DIRECTION FINDING OF LONG TERM EVOLUTION ENABLED HANDSETS FOR MONITORING APPLICATIONS

by

Johannes Rossouw van der Merwe

Submitted in partial fulfillment of the requirements for the degree

Master of Engineering (Electronic Engineering)

in the

Department of Electrical, Electronic and Computer Engineering
Faculty of Engineering, Built Environment and Information Technology
UNIVERSITY OF PRETORIA

February 2016

© University of Pretoria

UNIVERSITEIT VAN PRETORIA
UNIVERSITY OF PRETORIA
YUNIBESITHI YA PRETORIA

© University of Pretoria

I would like to thank:

My wife, Suné, for her support,

my father, Abel, for the love of engineering,

my mother, Connie, for her patience and understanding,

Hendrik du Rand and Francois Maasdorp for their technical inputs.

© University of Pretoria

© University of Pretoria

SUMMARY

DIRECTION FINDING OF LONG TERM EVOLUTION ENABLED HANDSETS FOR MONITORING APPLICATIONS

by

Johannes Rossouw van der Merwe

Supervisors:	Prof L. P. Linde and Prof W. P. du Plessis
Department:	Electrical, Electronic and Computer Engineering
University:	University of Pretoria
Degree:	Master of Engineering (Electronic Engineering)
Keywords:	Array signal processing, Direction-of-arrival estimation, FD-Root-MuSiC algorithm, 4G mobile communication

Given the widespread adoption of cellular-phones, it can be assumed that the presence of a phone can predict with good certainty the presence of a human being. Therefore the location of phones in restricted areas can aid in anti-poaching, anti-smuggling, illegal immigration, and search-and rescue operations. There are numerous obstacles associated with regulations and policies which restrict the direct use of the cellular network, therefore the acquisition of a non-network cooperative (NNC) direction finding (DF) receiver system is required. This dissertation addresses the development of such a NNC system.

The system requirements for a NNC-DF is analysed to illustrate the design challenges, such as DF accuracy, dynamic range, inter-channel interference, processing requirements and cost. Theoretical analysis of different receiver designs, DF estimation algorithms, processing methods, and sensory input configurations, are done and investigated through simulation. The simulation results are used to optimise the system parameters in terms of processing time versus DF accuracy. The optimised results are then used to discuss the design process for an operational system.

Several Multiple Signal Classification (MuSiC) based algorithms are used for the direction-of-arrival (DOA) estimation, as these algorithms are super-resolution phase interferometry

algorithms. Linear and circular sensor arrays of four to six elements are considered for the investigation. A selection of receivers which use different levels of signal isolation and integration methods are used and compared.

The simulation results illustrate that receiver designs with high signal separation have superior results, but the associated processing requirements make these receivers impractical. Many of the simpler receiver architectures achieved competitive DF accuracy, and required only a fraction of the processing resources. Exploiting the resource block (RB) structure of Long-Term Evolution (LTE), the 12-carriers per RB can be combined to improve DF estimation. It was found that integration of the autocovariance matrix (ACM) of 12 carriers in a RB (MuSiC based algorithms require the ACM for estimation) yields the best results. The Root-MuSiC algorithm resulted in the optimal performance versus processing time for linear arrays, and the frequency-domain Root-MuSiC algorithm for circular arrays. Advanced forms of the MuSiC algorithm, which use the weighted least squares (WLS) algorithm, required additional processing, but results did not improve significantly. It was also found that the design of the receiver had a greater influence on the performance than the DF algorithms.

Optimisation was done so as to find the best combination of the following:

- receiver design,
- integration method,
- windowing method,
- DF algorithm,
- antenna configuration and
- antenna size.

The optimisation compared the processing time to DF accuracy of the different DF systems. It was shown that for uniform circular arrays (UCAs), simple receiver architectures with ACM integration over a RB, using a rectangular window and the frequency-domain (FD)-Root-MuSiC algorithm, yielded the best processing time versus DF accuracy. Similar results were found with uniform linear arrays (ULAs), with the exception that the Root-MuSiC algorithm performed better. Optimisation proved efficient DF receiver design.

It was concluded that the best possible DF accuracy often requires an impractical system.

Similarly, arbitrary large arrays yield excellent results, but are expensive and impractical for mobile applications. Through optimisation of the simulation results the development of a realisable system with the best possible performance is possible.

© University of Pretoria

© University of Pretoria

OPSOMMING

RIGTINGPEILING VAN LANGTERMYN EVOLUSIE GEAKTIVEERDE PLATFORMS VIR MONITERING-TOEPASSINGS

deur

Johannes Rossouw van der Merwe

Studieleier(s):	Prof L. P. Linde en Prof W. P. du Plessis
Departement:	Elektriese, Elektroniese en Rekenaar-Ingenieurswese
Universiteit:	Universiteit van Pretoria
Graad:	Magister in Ingenieurswese (Elektroniese Ingenieurswese)
Sleutelwoorde:	FD-wortel-MuSiC algoritme, Rigting-van-aankoms estimasie, Samestelling seinverwerking, 4G mobiele kommunikasie

Gegewe die wydverspreide gebruik van sellulêre fone, kan dit aanvaar word dat die teenwoordigheid van ’n selfoon met sterk sekerheid die teenwoordigheid van ’n mens kan voorspel. Gevolglik kan die bepaalde ligging van ’n selfoon in ’n verdagte gebied help om bv. stropery, smokkel, en onwettige immigrasie teen te werk, asook help met soek- en reddingsoperasies. Wette en regulasies bied struikelblokke wat die direkte gebruik van ’n sellulêre netwerk beperk om die ligging van ’n sellulêre foon te bepaal. Daarom is dit noodsaaklik om ’n nie-netwerk koherente (NNK) rigtingpeiling (RP) - stelsel te gebruik om die ligging van sellulêre fone te bepaal. Hierdie verhandeling spreek die ontwerp van so ’n NNK stelsel aan.

Die stelselvereistes vir ’n NNK RP-stelsel word ontleed, terwyl die geassosieerde ontwerpsuitdagings, soos akkuraatheid, dinamiese bereik, inter-kanaal steuring, verwerkingsvereistes en koste in ag geneem word. Die teoretiese analise van verskillende ontvangerontwerpe, rigtingpeiling algoritmes, en verwerking metodes is gedoen en bevestig deur simulasie. Die simulasieresultate word gebruik om die stelselparameters te optimiseer in terme van verwerkings-tyd teenoor rigtingpeilings akkuraatheid. Die resultate wat as optimaal beskou word, word bespreek in terme van die ontwerp van ’n operasionele stelsel.

© University of Pretoria

Verskeie MuSiC-gebaseerde algoritmes word gebruik vir die rigting-van-aankoms estimasie, omdat hierdie algoritmes super-resolusie fase-interferometriese tegnieke is. Lineêre en sirkulêre sensorsamestellings met vier tot ses elemente word ondersoek in hierdie studie. ’n Verskeidenheid van ontvangers met verskillende seinisolasietegnieke en integrasiemetodes word gebruik en vergelyk.

Die simulasieresultate wys daarop dat die ontvangerontwerpe, met hoë seinisolasietegnieke, bostaande resultate toon, maar dat die verwerkingsvereistes van dié tegnieke onrealisties hoog is. Eenvoudiger ontvangerontwerpe bereik kompeterende rigtingpeilings akkuraathede, maar vereis slegs ’n fraksie van die verwerkingshulpbronne. Deur die ontginning van die verwerkingsblok (VB) van Langtermyn Evolusie (LTE), kan die 12 draers per VB gekombineer word om die rigtingpeiling te verbeter. Daar is bevind dat die integrasie van die kovariansiematriks van elk van die 12 draers per VB (MuSiC gebaseerde algoritmes benodig ’n kovariansiematriks vir estimasie) die beste resultate lewer. Die Wortel-MuSiC algoritme het die beste akkuraatheid teenoor verwerkingstyd vir lineêre samestellings gelewer, en die frekwensie-domein (FD) Wortel-MuSiC algoritme die beste resulate vir sirkulêre samestellings gebeur. Gevorderde weergawes van die MuSiC-algoritme, wat die geweegde kleinste kwadrate algoritme gebruik, vereis addisionele verwerking, maar lewer resultate wat nie beduidend beter is nie. Dit is ook bevind dat die ontwerp van die ontvanger ’n groter invloed op die akkuraatheid van die estimasie het as wat die rigtingpeiling algoritmes bied.

Optimisering is gedoen om die beste kombinasie van die volgende faktore te vind:

- ontvanger ontwerp,
- integrasie metode,
- venstermetode,
- rigtingpeilings algoritme,
- antennasamestelling-opstelling en
- antennasamestelling-grootte.

Die optimiseringsproses vergelyk die verwerkingstyd en rigtingpeilings akkuraatheid van die verskillende stelselparameters. Daar is getoon dat eenvormige sirkulêre samestellings met eenvoudige ontvanger-argitektuur en kovariansiematriks integrasie oor ’n VB, met die FD-Wortel-MuSiC-algoritme, die beste verwerkingstyd teenoor rigtingpeilings akkuraatheid

© University of Pretoria

lewer. Soortgelyke resultate is gevind met eenvormige lineêre samestellings, met die uitsondering dat die Wortel-MuSiC algoritme. Die gebruik van optimiseringstegnieke lei tot doeltreffende rigtingpeilingontvanger ontwerp.

Die mees gewensde rigtingpeilings akkuraatheid vereis dikwels ’n onwerkbare stelsel. Verder lewer arbitrêre groot samestellings uitstekende resultate, maar is duur en oneffektief vir mobiele radio toepassings. Deur optimisering van die simulasieresultate kan werkbare stelsels ontwikkel word met die beste moontlike werkverigting.

© University of Pretoria

LIST OF ABBREVIATIONS

3-D	Three dimensional
3GPP	3rd Generation Partnership Project
4G	4th generation mobile networks
5G	5th generation mobile networks
ACM	Autocovariance matrix
ADC	Analogue-to-digital converter
AGC	Automatic gain control
AOA	Angle of arrival
ARD	Amplitude-range-Doppler
ASK	Amplitude-shift keying
AWGN	Additive white Gaussian noise
BER	Bit error rate
BPF	Bandpass filter
BPSK	Binary phase-shift keying
CDMA	Code-division multiple access
CP	Cyclic prefix
CPU	Central processing unit
CRB	Cramér-Rao bound
CRC	Cyclic redundancy check
DCT	Discrete cosine transform
DDC	Digital down-converter
DF	Direction finding
DFT	Discrete Fourier transform
DL	Down-link
DOA	Direction-of-arrival

© University of Pretoria

DoCoMo	Do Communications over the Mobile-network
DSP	Digital signal processor
E-UTRA	Evolved Universal Terrestrial Radio Access
EM	Electromagnetic
eNodeB	Evolved Node B
EPA	Extended pedestrian A
ESPRIT	Estimation of signal parameters via rotational invariance technique
ETSI	European Telecommunications Standards Institute
ETU	Extended typical urban
EVA	Extended vehicular A
FD	Frequency-domain
FDD	Frequency-division duplex
FDMA	Frequency-division multiple access
FFT	Fast Fourier transform
FIR	Finite impulse response
FOV	Field-of-view
FPGA	Field-programmable gate array
GPU	Graphics processing unit
GSM	Global System for Mobile Communications
ICI	Inter channel interference
IDFT	Inverse discrete Fourier transform
IF	Intermediate frequency
IFFT	Inverse fast Fourier transform
IMT-A	International Mobile Telecommunications Advanced
ISI	Inter symbol interference
ITU	International Telecommunication Union
ITU-R	International Telecommunication Union radio-communications Sector
LOS	Line of sight
LPF	Low pass filter
LQE	Linear quadratic estimation
LTE	Long-Term Evolution
LTE-A	Long-Term Evolution Advanced
MIMO	Multiple-input, multiple-output

© University of Pretoria

MP	Matrix pencil
MSE	Mean square error
MTN	Mobile Telephone Network
MuSiC	Multiple Signal Classification
MVDR	Minimum variance distortionless response
NB	Narrow band
NI	National Instruments
NNC	Non-network cooperative
NTT	Nippon Telegraph and Telephone
OFDM	Orthogonal frequency division multiplexing
PAPR	Peak-to-average-power ratio
PCA	Principal component analysis
PCCC	Parallel concatenated convolutional code
PDF	Probability density function
PN	Pseudo-noise
POI	Probability of intercept
PSD	Power spectral density
PSK	Phase-shift keying
QAM	Quadrature amplitude modulation
QoS	Quality of service
QPSK	Quadrature phase modulation
RB	Resource block
RE	Resource element
RF	Radio frequency
RMSE	Root mean square error
RRC	Root raised cosine
RWR	Radar warning receiver
S/P	Serial-to-parallel
SC-FDMA	Single-carrier frequency division multiple access
SDMA	Space-division multiple access
SDR	Software-defined radio
SLL	Sidelobe level
SNR	Signal-to-noise ratio

© University of Pretoria

SQNR	Signal-to-quantisation-noise ratio
SVD	Singular value decomposition
TDD	Time-division duplex
TDMA	Time-division multiple access
TDoA	Time difference of arrival
UCA	Uniform circular array
UCA-CE	Uniform circular array with a center element
UE	User equipment
UL	Up-link
ULA	Uniform linear array
WB	Wide-band
WLS	Weighted least squares

© University of Pretoria

NOMENCLATURE

$[\cdot]^H$	Hermitian transpose of a matrix
$\|\cdot\|$	Magnitude of a vector or absolute value of a scalar
$[\cdot]^*$	Complex conjugate
$[\cdot]^T$	Transpose of a matrix
A_m	Amplitude value on the mth OFDM carrier
a_n	Complex amplitude of the nth antenna element
A_{norm}	Normalised amplitude
$\mathbf{A}(\theta)$	Array steering matrix
$\dot{\mathbf{a}}(\theta)$	First derivative of the array steering vector
$\mathbf{a}(\theta,\phi)$	Antenna steering vector
b	Number of bits
$\mathbf{B}$	Factorised steering matrix
$\tilde{\mathbf{B}}$	Weighted least squares steering matrix
b_{ef}	Number of effective bits
B_f	Sample bandwidth
B_s	Bandwidth of the signal of interest
c	Speed of light
CRB	Cramér-Rao bound
CRB_{UCA}	Cramér-Rao bound of an uniform circular array
CRB_{UCA}	Cramér-Rao bound of an uniform circular array with a centre element
CRB_{ULA}	Cramér-Rao bound of an uniform linear array
D	Antenna directivity
d	Path length
d_A	Distance from handset A to DF system
d_B	Distance from handset B to DF system

© University of Pretoria

d_C	Distance from handset C to DF system
$\triangle d$	Distance between two sensors
$\delta[n]$	Delta Dirac function
$\Delta\theta$	Angular step size for the Fourier domain Root-MuSiC algorithm
d_{eNB}	Distance from eNode B to DF system
$\mathbf{d}_n$	Distance vector of the nth antenna element
d_s	Inter-element spacing of an uniform linear array
$\mathbf{e}_k$	The kth eigenvector
$\mathbf{E}_N$	The noise subspace
$\hat{\mathbf{E}}_N$	Estimated noise subspace
$\mathbf{E}_S$	The signal subspace
$\hat{\mathbf{E}}_S$	Estimated signal subspace
$\mathrm{E}\left[\cdot\right]$	Expected value
$\mathbf{F}$	Fisher information matrix
$\mathbf{f}$	Estimated vector of the MuSiC null-spectrum function
F_a	Array factor
F_{av}	Average radiation intensity
f_c	Sinusoidal centre frequency
f_D	Maximum Doppler frequency shift
F_m	The mth root of the Fourier domain Root-MuSiC algorithm
$\breve{F}_m$	Null-padded Fourier domain polynomial
F_{max}	Maximum radiation intensity
$f_{s,min}$	Minimum sampling frequency for TDoA systems
$\mathbf{F}_{m,n}$	The value in the Fischer information matrix in the mth row and nth column
F_n	Noise figure
$\mathscr{F}\left\{\cdot\right\}$	Fourier transform
f_s	Sample rate
f_{sym}	OFDM carrier spacing
$F(\theta,\phi)$	Antenna radiation pattern
$\hat{f}(\theta)$	Approximated MuSiC null-spectrum function
$f(\theta)$	The MuSiC null-spectrum function
$\breve{f}(z)$	Interpolated MuSiC null-spectrum function

© University of Pretoria

$\mathbf{G}$	Transformation matrix for manifold Root-MuSiC
G_r	Antenna gain from receiver
G_t	Antenna gain from transmitter
$\mathbf{g}(\theta)$	Virtual steering vector of an antenna array
$H_f[\omega]$	Filter response
H_m	Fourier domain weighted least squares polynomial coefficient
$\mathbf{I}$	Identity matrix
$\Im\{\cdot\}$	Imaginary values of a matrix
J	Number of one sided samples used for interpolation of the MuSiC null-spectrum function
j	Imaginary unit
$\mathbf{J}_m(\cdot)$	Bessel function of the first kind of order m
K	Number of data samples
k_b	Boltzmann's constant
$\mathbf{k}(\theta, \phi)$	Wave-number of each antenna element for the given signal
L	Number of signals
λ	Wave-length of a signal
λ_k	The kth eigenvalue
$\hat{\mathbf{\Lambda}}_{\mathbf{N}}$	Estimated eigenvalue matrix of the noise subspace
$\hat{\mathbf{\Lambda}}_{\mathbf{S}}$	Estimated eigenvalue matrix of the signal subspace
L_p	Ideal path-loss
M	Number of one sided samples used for the Fourier domain Root-MuSiC algorithm
M	Number of angle of arrival estimates
$MSE(\hat{\theta})$	Mean square error of the angle of arrival
μ_{en}	Mean of X_{en}
μ_n	Mean of X_n
M_w	Number of one sided samples used for the Fourier domain weighted least squares Root-MuSiC algorithm
N	Number of integrated data samples
N_a	Number of antenna elements
$\mathbf{n}(k)$	Noise signal at time sample k
N_{man}	Manifold number

© University of Pretoria

$\mathcal{N}(\mu, \sigma)$	Gaussian distribution with mean μ and standard deviation σ
N_q	Number of quantisation levels
N_{sym}	Number of modulated OFDM carriers
$\frac{\partial}{\partial\theta}$	Partial derivative in terms of angle of arrival
p_{gaus}	Probability density function of a Gaussian random variable
ϕ	Elevation angle
ϕ_0	Phase offset
P_{max}	Maximum received power
P_{min}	Minimum received power
P_n	Average power of X_n
P_r	Received power
p_{Ray}	Probability density function of a Rayleigh random variable
P_{rel}	Relative power
P_t	Transmitted power
Q	Number of test values for the weighted least squares algorithm
r	Radius of an uniform circular array
r_1	Radius from eNode B to cell edge
r_2	Radius from eNode B to nearest handset
R_c	Code rate
$\Re\{\cdot\}$	Real values of a matrix
p_{Rice}	Probability density function of a Ricean random variable
$VAR(\hat{\theta})$	Variance of the angle of arrival
$RMSE(\hat{\theta})$	Root mean square error of the angle of arrival
$R_{nn}[l]$	Ensemble autocorrelation with offset l
$\mathbf{R}_s$	Auto-covariance matrix of transmitted signal vector $\mathbf{s}$
$R_{s\|n}$	Cross terms between the signal and noise of the auto-covariance of the received signal
$\hat{\mathbf{R}}_{\mathbf{x}}$	Estimated auto-covariance matrix of received signal vector $\mathbf{x}$
$\mathbf{R}_x$	Auto-covariance matrix of received signal vector $\mathbf{x}$
$S_{cc}(f)$	Power spectral density of a single modulated OFDM carrier
$S(f)$	Doppler spread
σ_{en}^2	Variance of X_{en}
σ_n	Standard deviation of noise

σ_n^2	Variance of X_n
$\mathbf{s}(k)$	Transmitted signal at time sample k
$SNQR$	Signal to quantisation noise ratio
$S_{(t,\phi)}(f)$	Power spectral density of OFDM symbol with a phase discontinuity
$S_{xx}[m]$	Power spectral density of x at the mth frequency
T	Window period
T_0	Time offset
T_{CP}	Cyclic prefix period
t_{del}	Time delay
T_f	Radio frame of LTE
θ	Azimuth angle
$\hat{\theta}$	Estimated angle of arrival
$\langle\theta,\phi\rangle$	Direction of arrival set
$\hat{\theta}_{post}$	Post estimation integration output
T_{hf}	Half frame of LTE
T_K	Absolute temperature
$\textbf{trace}\left(\cdot\right)$	Trace of a matrix
T_s	Time unit of LTE
T_s	Sampling period
T_{sf}	Subframe of LTE
T_{slot}	Time slot of LTE
T_{sym}	Symbol period of an OFDM symbol
$\mathbf{u}$	Fourier domain weighted least squares polynomial vector
v	Normalised frequency shift variable
$\mathrm{VAR}\left[\cdot\right]$	Variance within a function
v_p	Propagation velocity
$\mathbf{v}_r$	Polynomial vector
$W_{rec}[m]$	Rectangular window function
$w(\theta)$	Weights for weighted least squares algorithm
$\mathbf{W}_\theta$	Weighing matrix
X_{en}	Integrated Gaussian distributed random variable
$x_i[n]$	Input to a finite impulse response filter at the nth time sample
$X_i[\omega]$	Frequency domain input of a finite impulse response filter

© University of Pretoria

$x[k]$	Observed signal at the kth sample
$\mathbf{x}(k)$	Received signal vector at time sample k
$X[m]$	Frequency domain of the received signal at the mth frequency
X_n	Gaussian distributed random variable
$x_n[k]$	Noise at the kth sample
$X_{OFDM}[m]$	Modulated data on the mth carrier
$x_{OFDM}[n]$	Time domain data of an OFDM symbol at the n sample
$x_{OFDM}^{IS}[n]$	Finite time domain representation of an OFDM symbol
$X_{OFDM}^{IS,CT}(f)$	Frequency domain of the continuous time expansion of an OFDM symbol
$x_{OFDM}^{IS,CT}(t)$	Continuous time expansion of an OFDM symbol
$x_o[n]$	Output from a finite impulse response filter at the nth time sample
$X_o[\omega]$	Frequency domain output from a finite impulse response filter
$x_s[k]$	Signal with information at the kth sample
$X_s[m]$	Frequency of the information signal at the mth frequency
$y_f[n]$	Continuous time expansion of a channeliser output
$y_m[n]$	Output from channeliser receiver of the nth sample and the mth tap
z	A root of the MuSiC null-spectrum function
$\mathbb{Z}$	Integer values

© University of Pretoria

TABLE OF CONTENTS

© University of Pretoria

© University of Pretoria

© University of Pretoria

© University of Pretoria

LIST OF FIGURES

© University of Pretoria

© University of Pretoria

© University of Pretoria

LIST OF TABLES

© University of Pretoria

© University of Pretoria

CHAPTER 1

INTRODUCTION

1.1 PROBLEM STATEMENT

1.1.1 Context of the problem

Mobile communication platforms, such as cellular phones and tabular devices, are widely used throughout the world. In October 2014 the number of mobile subscribers using the technology officially surpassed the human population of approximately 7.18 billion [1]. It can therefore be assumed that there is a strong correlation between the location of such a device and that of a human being. Locating a mobile communication platform, and implicitly locating people, can therefore be used for the following applications:

- search, rescue and other emergency operations;
- natural resource protection against poaching;
- border safeguarding for smuggling and illegal immigration;
- policing activities; and
- for spectral monitoring actions (population profiling).

A method used for tracking is to estimate the direction of the communication signal from the source (mobile communication device) to the receiving system. By combining multiple direction-of-arrival (DOA) estimates, the location of the target can be obtained through triangulation. Once the location is known, the target can be tracked. This dissertation focuses on the DOA estimation of such a system.

© University of Pretoria

Mobile operators typically have the ability to track and locate the users of the network; however due to legal, corporate and administrative obstacles it is often not a viable option for quick response operations. Therefore, in-field tracking without the aid of the cellular network is required. Non-network cooperative (NNC) DOA estimation is considerably more difficult and requires a more complex system. The probability of intercept (POI) and system performance are both reduced due to lack of a-priori signal information, emitter-receiver geometry and the characteristics that a mobile communication platform transmits asynchronously and non-continuously. While the techniques underlying NNC DOA are well-known [2], to the best of the author's knowledge, the combination use here has not been considered in the literature.

Long-Term Evolution (LTE) is a 4th generation mobile networks (4G) technology and is currently the most recent implemented specification for cellular communications. It should be noted that 5th generation mobile networks (5G) is due to be launched before the year 2020 [3]. Due to the high data rates of the system, LTE has become very popular with the increased use of smart-phones. LTE is available in South Africa and was quickly adopted. LTE is a new communication protocol that has not been thoroughly studied for NNC direction finding (DF) techniques.

1.1.2 Research gap

DF techniques used on orthogonal frequency division multiplexing (OFDM) systems, such as LTE, usually assumes full network cooperation. This means that the DF algorithms are optimal as they are fully synchronised with the source communication signal. Further, the signal properties are known and can be exploited by the receiver, hence the POI is greatly increased. There is little research on NNC-DF techniques which are focused on cellular communication signals, hence a research gap is identified.

1.2 RESEARCH OBJECTIVE AND QUESTIONS

The object of the research is to determine which processing methods can be used to increase the DF accuracy through the exploitation of the OFDM signal structure used in LTE.

© University of Pretoria

1.3 HYPOTHESIS AND APPROACH

DOA estimation techniques in conjunction with spectral estimation can be used to enhance DF on communication signals, as used in LTE, to obtain the location of a person. By exploiting the underlying signal structure it should be possible to increase DF accuracy in the presence of multiple interfering signals.

A DF system that uses an antenna array will be simulated to determine and compare the effectiveness of different antenna array types on DOA estimation algorithms.

1.4 RESEARCH GOALS

The following goals are specified for the research:

- To determine if the DOA estimation techniques are applicable and can be adapted for OFDM-based communication signals,
- Investigate the effects of the antenna array configuration on the performance of the DOA estimation,
- To determine the angular resolution obtainable by a DF system,
- Explore the characteristics of OFDM based signals that can be exploited to increase DF accuracy.

1.5 RESEARCH CONTRIBUTION

NNC-DF on LTE signals can be beneficial to emergency, security and monitoring services, without the required cooperation or network infrastructure of the cellular network operators. The DF of LTE specific signals can also aid in spacial multiplexing within a communication system to enhance system capacity.

1.6 OVERVIEW OF STUDY

Chapter 2 provides background to the theoretical concepts required for NNC system design and what is currently used in literature.

© University of Pretoria

Chapter 3 analyses the NNC receiver problem and shows the associated signal processing restrictions. The engineering challenge is greatly emphasised by the theoretical concepts provided in this chapter.

Chapter 4 provides the details of a simulation set-up, shows the results, and discusses what is observed in the simulations. Further, the results of the simulations are used to determine the optimal receiver design parameters.

Chapter 5 uses the simulation results of chapter 4 and applies it to practical system design. This chapter illustrates that the theoretical best results are often impractical for operational systems.

Chapter 6 summarises the outcomes of the study and draws conclusions on the work done.

© University of Pretoria

CHAPTER 2

LITERATURE STUDY

2.1 CHAPTER OBJECTIVES

This chapter provides a background of DF techniques, with emphasis on the Multiple Signal Classification (MuSiC) algorithm. Related topics such as estimation theory, noise reduction, signal isolation and integration, and sensor arrays are also discussed. An overview of the LTE specification, with emphasis on the physical layer, is given.

2.2 DIRECTION FINDING TECHNIQUES

DOA estimation determines the direction from which a signal originates, in both the azimuth and elevation angles of the receiver system. Angle of arrival (AOA) on the other hand only estimates a single angle of the DOA. In most cases AOA estimation is applied to the azimuth angle of the system, however any single measurement-plane can be used.

DOA estimation can be achieved through multiple methods. In this discussion only non-cooperative electromagnetic (EM) signal DF is considered; however, it should be noted that some co-operative techniques, such as querying a source to reveal its location, exist.

For EM signal DF, the DOA estimation technique is dependent on the physical attributes of the sensor system. DOA systems can be categorised as follows:

1. amplitude comparison,
2. time difference of arrival (TDoA),
3. phase comparison.

© University of Pretoria

Amplitude comparison techniques either use multiple sensors, or multiple measurements at different positions and/or orientations to perform DOA estimation. The technique compares the amplitude from different data samples and determines from which direction the source signal originated from, by selecting the DOA that is associated with the largest measured amplitude.

By using multiple directional sensors, where each sensor is placed in order to cover a different sector such that the full 360° azimuth is covered, multiple sensors can be used to achieve amplitude comparison. Another popular method is to use a single directional sensor which is rotated, and then to select the AOA at the angle at which the signal is observed to be the most powerful. This is referred to as a spinning-DF. The advantage of the spinning-DF is that only a single sensor is required. However the drawback is that the mechanical dynamics of the system requires regular maintenance. Lastly, manual amplitude comparison can be done by using a single hand-held sensor that can be pointed in the direction of interest. Hand-held amplitude comparison is often used to locate beacons and illegal broadcast transmissions for spectral monitoring and regulative tasks.

TDoA requires multiple sensor elements, as the measured time difference caused by the travel time of the EM signal between these sensors are compared. This method is possible due to the fact that any signal is limited by its propagation velocity, and in the case of a EM signal it is the speed of light. The complication with this method is that the sample rate f_s of such a system should be sufficiently high to be able to measure the time differences. Alternatively the distance between sensors should be increased such that the travel distance for the wave, and consequently the travel time, is increased. This observation limitation is related to the propagation velocity, and as a result TDoA is more popular in auditory systems (i.e. SONAR) than in EM systems. The minimum required sample-rate $f_{s,min}$ for a two element system is related to the propagation velocity v_p (in the case of an EM wave it is the speed of light c) and the distance between the two sensors $\triangle d$:

$$f_{s,min} = \frac{v_p}{\triangle d} = \frac{c}{\triangle d}. \tag{2.1}$$

Phase comparison DF assumes that the sample rate condition is not met by the system (2.1). In the majority of the cases the condition is not met as the distance between the sensors is reduced to make the system smaller, in many cases with the objective of being portable. The

© University of Pretoria

frequency of use, also has a significant influence on the size of the array, hence high frequency systems may force the separation distance to be reduced. In phase comparison the phase difference between the sensor elements is used to estimate the DOA. Phase comparison is also known as phase interferometry.

Phase comparison requires multiple antenna elements. Multiple elements increase system performance through diversity gain. Typically the system performance increases as the number of sensor elements are increased. The spatial relations of a uniform linear array (ULA) has similar mathematical characteristics as the frequency content of a signal, thus signal frequency estimation techniques can be adapted for DOA estimation [4]. It can therefore be concluded that a discrete Fourier transform (DFT) can be used to transform a measurement set from the sensor array to the received power over different incident angles. These methods are considered similar to DF phase estimation. For other array configurations the techniques can be adapted, but a mathematical transformation is required. There are multiple frequency estimation techniques [5] that can be adapted for interferometry.

2.2.1 Super Resolution DF techniques

Super resolution DF techniques are DOA estimation methods with an angular resolution smaller than the main beam-width of the antenna array. The resolution of a DF system is defined as the smallest relative incident angle between two independent sources which the sensor system can differentiate as being independent signals.

A popular super resolution DF technique is the MuSiC algorithm, as it can be used for any sensor array configuration and allows the DOA of multiple sources to be estimated simultaneously [6–8]. MuSiC is a principal component analysis (PCA) based technique and uses eigenvalue decomposition on the autocovariance matrix (ACM) of the received signals to estimate the signal parameters.

Estimation of signal parameters via rotational invariance technique (ESPRIT) is a super resolution AOA estimation technique that is computationally less complex than MuSiC. However, it has configurational restrictions on the usable sensor array. MuSiC has been found to have superior performance over ESPRIT [9], and joint MuSiC-ESPRIT algorithms have also been considered with improved performance at the cost of a great increase in complexity [10]. Im-

© University of Pretoria

proved versions of MuSiC and ESPRIT have been developed based on cyclostationarity, but requires a-priori information of the transmitted signals [11]. Both the MuSiC and ESPRIT algorithms incorporate a search step to find an optimal solution. Methods to reduce the parametric search have therefore been developed. A neural network technique has also been considered and implemented to reduce the parameter search [12].

Matrix pencil (MP) algorithms apply singular value decomposition (SVD) to a windowed matrix of the received signal to estimate the TDoA between the elements [13]. The MP has the benefit that it is independent of the ACM and can be used to estimate the TDoA of non-stationary signals [14]. MP is a mathematical extension on the ESPRIT algorithm and has a computational benefit of being independent of parametric searches [15, 16].

The Capon algorithm, also known as the minimum variance distortionless response (MVDR) beam-former is based on the Barlett algorithm [17], and was originally used for locating seismic activity. This method aims to impose a unity gain in "look"-direction whilst minimising the received power in all other directions. The constraint minimisation problem is solved through the use of Lagrange multipliers. The benefit of this algorithm is that it reduces interference signals form other directions as it follows a beam-former approach.

2.2.2 Sensor Array

The configuration of the sensor input influences the design of a DF system, as it determines which DF algorithms can be used, the signal processing, cost, and physical dimensions of a system. If a mechanically static system is required (hence no moving parts) then a sensor array should be used. Further, the use of multiple sensors are widely used in DF systems due to diversity gain and as it allows the use of super resolution techniques.

2.2.2.1 Antennae and Arrays

An antenna is an EM transducer between a transmission line and a propagating EM wave in an unbounded medium [18]. The physical dimensions and properties of an antenna determines the radiation pattern of the said antenna in free space.

A wave that is radiated by a point source propagates spherically away from the point. As

© University of Pretoria

the wave propagates from the source the radius of the sphere increases, and at a sufficiently large radius it can be assumed that the wave-front at a given point is approximately flat, relative to the receiver system. The far-field is defined as the region where the wave-front is approximated to be flat. The radiation pattern is a directional function that characterises the relative power distribution of an antenna in the far field. The directivity of an antenna D is defined as the ratio between the maximum radiation intensity F_{max} and the average radiation intensity F_{av}:

$$D = \frac{F_{max}}{F_{av}}. \tag{2.2}$$

Most phase interferometry algorithms assume that omnidirectional antennas are used. An omnidirectional antenna radiates equal energy in all directions. In practice dipole antennas are often used, as the respective radiation pattern $F(\theta, \phi)$ is only a function of the elevation angle from the horizon ϕ and independent of the azimuth angle θ:

$$F(\theta, \phi) = \left(\frac{\cos\left(\frac{\pi}{2}\sin(\phi)\right)}{\cos(\phi)} \right)^2. \tag{2.3}$$

If multiple antenna elements are phase synchronised, the array factor $F_a(\theta, \phi)$ of those elements can be calculated. The array factor F_a is a component sum of the N_a array elements, and is a function of each antenna signal's complex amplitude a_n; the position of each antenna in three dimensional (3-D) space $\mathbf{d}_n$; and the wave-number of the signal, $\mathbf{k}$:

$$F_a = \left| \sum_{n=0}^{N_a-1} a_n \mathrm{e}^{-\,\mathbf{j}\mathbf{k}\cdot\mathbf{d}_n} \right|^2. \tag{2.4}$$

If all array elements have the same radiation pattern, the radiation pattern with the elements can be multiplied to the array factor to obtain the radiation pattern of the antenna array. By altering the signal's complex amplitudes a_n for each element, the radiation pattern can be altered, therefore enabling beam-steering. These signal attributes are also known as the array steering vector. Given an array of N_a antenna elements , the resultant $(N_a \times 1)$ steering vector $\mathbf{a}(\theta, \phi)$ of that antenna array is described as:

$$\mathbf{a}(\theta, \phi) = \begin{bmatrix} \mathrm{e}^{\mathbf{j}\mathbf{k}(\theta,\phi)\cdot\mathbf{d}_1} & \dots & \mathrm{e}^{\mathbf{j}\mathbf{k}(\theta,\phi)\cdot\mathbf{d}_{N_a}} \end{bmatrix}^T. \tag{2.5}$$

The wave-number k is the spatial vector and a function of the azimuth angle θ, elevation angle ϕ and the expected signal's wave-number, as shown in:

$$\mathbf{k}(\theta, \phi) = \frac{2\pi}{\lambda} \begin{bmatrix} \sin\phi\cos\theta & \sin\phi\sin\theta & \cos\phi \end{bmatrix}. \tag{2.6}$$

© University of Pretoria

Most antennas are reciprocal in nature, hence the radiation pattern is equivalent to the power received from each direction. Therefore the radiation pattern and steering vector can be used for DOA estimation. Many algorithms address the reverse problem, through estimating the steering vector which will result in a reproduction of the measured data. This is why a good understanding of antenna arrays and beam steering is required for DOA estimation.

It should be noted that beam-forming is proven optimal with narrow band (NB) signals. Similarly, most DOA algorithms are only applicable to NB signals.

Popular configurations that include uniformly spaced arrays are the ULA and the uniform circular array (UCA). The ULA consists of N_a elements located on a straight line with an equal spacing between them. For example, if all the elements are located along the x-axis with a spacing of d_s, then the position of all the elements $\mathbf{d}$ are given by :

$$\mathbf{d} = d_s \begin{bmatrix} -\frac{N_a}{2} & -\frac{N_a+1}{2} & \dots & \frac{N_a-1}{2} & \frac{N_a}{2} \end{bmatrix} \cdot \hat{\mathbf{x}}. \tag{2.7}$$

The benefit of a ULA is that the DFT of the steering vector can be used to generate the radiation pattern of the array:

$$F_a = \left| \sum_{n=0}^{N_a-1} a_n \mathrm{e}^{-\mathrm{j} n d_s \frac{2\pi}{\lambda}} \right|^2 = \left| \mathscr{F}\left\{ \mathbf{a} \right\} \right|^2 . \tag{2.8}$$

The wave-number k is set to $\frac{2\pi}{\lambda}$, where λ is the wavelength of the signal of interest. The Fourier transform is denoted by $\mathscr{F}\left\{\cdot\right\}$. The use of the DFT greatly simplifies the required mathematical calculations. The major drawback of a ULA is that the radiation pattern is symmetrical over the line on which the elements are located, therefore the line-symmetry causes a 180° ambiguity. In practice, directional antennas are used to limit the beam to only a single side of symmetry in order to resolve the ambiguity. In the process the array has a smaller field-of-view (FOV).

A UCA consists of N_a antenna elements that are located on a circle with radius r. The spatial vector can be described as:

$$d_n = r \cdot \cos\left(2\pi \frac{n}{N_a}\right) \cdot \hat{\mathbf{x}} + r \cdot \sin\left(2\pi \frac{n}{N_a}\right) \cdot \hat{\mathbf{y}}. \tag{2.9}$$

The benefit of a UCA is that it has a 360° azimuth coverage, hence making AOA possible in

© University of Pretoria

all angles, if a sufficient number of elements are used. The main lobe of a UCA is broader than that of a ULA array, for the same number of antenna elements.

2.2.2.2 Selection of the Sensor Array

ULAs are typically used for multiple-input, multiple-output (MIMO) communications as they are fairly simple to implement and can form narrow beams [6]. A ULA has a DF ambiguity [4]. However, for cellular communications sectoring is used with directed antenna elements. The sectoring thus removes the DF ambiguity, at the cost of requiring a ULA for each sector [9]. The adaptation of interferometry algorithms for non-linear antenna arrays has been done, but increases the algorithm's complexity [4, 7]. Using a ULA for each sector is expensive and requires multiple replicas of the same system.

Monitoring applications, where NNC-DF is used, typically use a single UCA . This is done such that a single system is required and that a DF ambiguity is eliminated. A comparison of the two structures for smart antenna arrays have been done [19], but circular arrays have not been used for DF on LTE or similar communication systems.

LTE is an agile system with variable bandwidth that can be changed by the base-station according to the required spectrum within the available allocated spectrum [20]. Furthermore, the allocated bandwidth for each mobile station can be reallocated per LTE frame of 1 ms. This also implies that the DOA estimation should be achieved within 1 ms. Each mobile station can be assigned a different portion of the frequency band and time slots. An additional step to determine the DOA signal is therefore to determine which resources is allocated to a user. Hence joint time-, frequency- and DOA estimation should be implemented per mobile station for successful locating.

© University of Pretoria

2.3 DOA ESTIMATION PERFORMANCE

2.3.0.3 Estimation

Given a variable θ and the estimator of the variable $\hat{\theta}$, the mean square error (MSE) is defined as the average power of the error [21]:

$$MSE(\hat{\theta}) = \frac{1}{M}\sum_{m=1}^{M}(\hat{\theta}_m - \theta)^2. \tag{2.10}$$

The root mean square error (RMSE), also referred to as the absolute error, is the square-root of the MSE:

$$RMSE(\hat{\theta}) = \sqrt{MSE(\hat{\theta})} = \sqrt{\frac{\sum_{m=1}^{M}(\hat{\theta}_m - \theta)^2}{M}}. \tag{2.11}$$

The RMSE is used as a baseline to determine the performance of an estimator. The benefit of using the RMSE, rather than the MSE, is that it has the same units as the estimated variable and is therefore simpler to compare with. Errors are usually caused by the noise in a system.

2.3.0.4 The Cramér-Rao bound

The Cramér-Rao bound (CRB) is the lower bound for which estimation of θ is possible [2]. The CRB for an estimated variable is defined by the variance expected of that variable:

$$\mathrm{MSE}(\hat{\theta}) = \mathrm{VAR}[\hat{\theta}] \geq \mathrm{CRB}. \tag{2.12}$$

The CRB for AOA estimation is derived from the Fisher information matrix F and the number of data points K used in the measurement:

$$\mathrm{MSE}(\hat{\theta}) = \frac{1}{K}\mathbf{F}^{-1}. \tag{2.13}$$

The Fisher information matrix, for the estimation of a single signal, is a scalar [22]:

$$\mathbf{F} = \mathsf{trace}\left(\mathbf{R}_x^{-1}\frac{\partial\mathbf{R}_x}{\partial\theta}\mathbf{R}_x^{-1}\frac{\partial\mathbf{R}_x}{\partial\theta}\right). \tag{2.14}$$

The covariance matrix $\mathbf{R}_x$ is a function of the signal-to-noise ratio (SNR) and the steering vector of the array $\mathbf{a}(\theta)$:

$$\mathbf{R}_x = \mathrm{SNR}\cdot\mathbf{a}(\theta)\mathbf{a}(\theta)^H + \mathbf{I}, \tag{2.15}$$

© University of Pretoria

where $\mathbf{I}$ is defined as the identity matrix and the Hermitian transpose is defined by $(\cdot)^H$. The resultant Fisher matrix can be determined to be a function of the SNR, the number of antenna elements N_a and the derivative of the steering vector:

$$\mathbf{F} = 2\text{SNR} \times |\dot{\mathbf{a}}(\theta)|^2 \frac{N_a\text{SNR}}{N_a\text{SNR}+1}. \tag{2.16}$$

The CRB for AOA estimation can be simplified if it is assumed that the number of antenna elements N_a is arbitrarily large. Then the CRB can be simplified by:

$$\text{CRB} \approx \frac{1}{2K \times \text{SNR} \times |\dot{\mathbf{a}}(\theta)|^2}, \tag{2.17}$$

where K is the number of snapshots of the signal used and $\dot{\mathbf{a}}(\theta)$ is the derivative of the steering vector in terms of the incident angle.

The CRB for multiple signals is typically higher due to the interference between the signals. The Fisher information matrix for P signals can be defined as:

$$\mathbf{F} = \begin{bmatrix} F_{1,1} & \cdots & F_{1,P} \\ \vdots & \ddots & \vdots \\ F_{P,1} & \cdots & F_{P,P} \end{bmatrix}, \tag{2.18}$$

where each of the values $F_{n,m}$ in the Fisher information matrix is defined by the respective partial derivative of the incident angle set (θ_m, θ_n) as shown:

$$\mathbf{F}_{m,n} = \text{trace}\left(\mathbf{R}_x^{-1}\frac{\partial \mathbf{R}_x}{\partial \theta_m}\mathbf{R}_x^{-1}\frac{\partial \mathbf{R}_x}{\partial \theta_n}\right). \tag{2.19}$$

As there are multiple signals present, the definition of the covariance matrix is changed to:

$$\mathbf{R}_x = \sum_{p=1}^{P} \text{SNR}_p \mathbf{a}_p(\theta)\mathbf{a}_p(\theta)^H + \mathbf{I}. \tag{2.20}$$

By solving the Fisher information matrix for the given signal set, the CRB for each signal can be determined.

2.4 THE MUSIC ALGORITHM

The MuSiC algorithm is selected for further discussion, as it is a super resolution DOA estimation algorithm that can be used on any array configuration. Many DOA estimation

© University of Pretoria

algorithms are bounded to certain array configurations (e.g. ESPRIT requires two identical array sets), hence the unbounded property of the MuSiC algorithm is beneficial. The MuSiC algorithm therefore allows the simple comparison of different array configurations.

2.4.1 Spectral MuSic Algorithm

The MuSiC algorithm is a super resolution interferometry technique used for DOA estimation [23].

The sensor array receives L NB far-field signals, each with a DOA of $\langle\theta, \phi\rangle$. The DOA values are defined as:

$$\langle\theta, \phi\rangle = \begin{bmatrix} \langle\theta_1, \phi_1\rangle & \dots & \langle\theta_L, \phi_L\rangle \end{bmatrix}^T \tag{2.21}$$

A single snapshot at a discrete time k of the received signal x can be represented as:

$$\mathbf{x}(k) = \mathbf{A}(\theta)\mathbf{s}(k) + \mathbf{n}(k), \tag{2.22}$$

where $s(k)$ is a $(L \times 1)$ vector of the signal waveforms, and $\mathbf{A}(\theta, \sigma)$ is the $(N_a \times L)$ signal steering matrix. The steering matrix $\mathbf{A}(\theta, \sigma)$ is defined as:

$$\mathbf{A}(\theta) = \begin{bmatrix} \mathbf{a}(\theta_1, \phi_1) & \dots & \mathbf{a}(\theta_L, \phi_L) \end{bmatrix}, \tag{2.23}$$

where $n(k)$ is a $(L \times 1)$ vector representing the received noise and is assumed additive white Gaussian noise (AWGN) with a variance of σ_n^2. The noise vector is defined as:

$$\mathbf{n}(k) \sim \mathcal{N}(0, \sigma_n). \tag{2.24}$$

The ACM R_x of the received signal is a $(N_a \times N_a)$ Hermitian matrix and is defined as the expected value of the multiplication of the received signal and its Hermitian transpose:

$$\mathbf{R_x} = \mathrm{E}\left[\mathbf{x}(k) \times \mathbf{x}(k)^H\right] = \mathbf{A}\mathbf{R_s}\mathbf{A}^H + \sigma_n^2\mathbf{I}. \tag{2.25}$$

The ACM R_s of the source signals is defined in:

$$\mathbf{R_s} = \mathrm{E}\left[\mathbf{s}(k) \times \mathbf{s}^H(k)\right]. \tag{2.26}$$

© University of Pretoria

The ACM should be approximated from the data. To improve the approximation of the ACM, K windows of the data can be averaged:

$$\hat{\mathbf{R}}_{\mathbf{x}} = \frac{1}{K}\sum_{k=1}^{K}\mathbf{x}(k) \times \mathbf{x}^{H}(k). \tag{2.27}$$

The ACM can be composed into eigenvalue λ_k and eigenvector e_k pairs:

$$\mathbf{R}_{\mathbf{x}} = \sum_{k=1}^{N_a}\lambda_k \mathbf{e}_k \mathbf{e}_k^H. \tag{2.28}$$

The largest L eigen-pairs can be regarded as the eigenvalues and eigenvectors describing the signal subspace:

$$\mathbf{E}_S = \begin{bmatrix} \mathbf{e}_1 & \dots & \mathbf{e}_L \end{bmatrix}, \tag{2.29}$$

and the remaining eigenvalues and eigenvectors describe the noise subspace:

$$\mathbf{E}_N = \begin{bmatrix} \mathbf{e}_{L+1} & \dots & \mathbf{e}_{N_a} \end{bmatrix}. \tag{2.30}$$

Note that the eigen-pairs should be sorted in descending values for this decomposition, as shown:

$$\left(\hat{\lambda}_1 \geq \hat{\lambda}_2 \geq \cdots \geq \hat{\lambda}_{N_a}\right). \tag{2.31}$$

The approximation ACM can therefore be separated into a signal ACM and a noise ACM:

$$\hat{\mathbf{R}}_{\mathbf{x}} = \hat{\mathbf{E}}_{\mathbf{S}}\hat{\mathbf{\Lambda}}_{\mathbf{S}}\hat{\mathbf{E}}_{\mathbf{S}}^H + \hat{\mathbf{E}}_{\mathbf{N}}\hat{\mathbf{\Lambda}}_{\mathbf{N}}\hat{\mathbf{E}}_{\mathbf{N}}^H. \tag{2.32}$$

The eigenvalue diagonal matrices are defined by the signal-subspace eigenvalues:

$$\hat{\mathbf{\Lambda}}_{\mathbf{S}} = \mathrm{diag}\left(\hat{\lambda}_1, \dots, \hat{\lambda}_L\right), \tag{2.33}$$

and the noise-subspace eigenvalues:

$$\hat{\mathbf{\Lambda}}_{\mathbf{N}} = \mathrm{diag}\left(\hat{\lambda}_{L+1}, \dots, \hat{\lambda}_{N_a}\right). \tag{2.34}$$

The MuSiC null-spectrum function is defined by the array steering vector and the noise-subspace eigenvector-matrix:

$$f(\theta) = \mathbf{a}^H(\theta,\phi)\hat{\mathbf{E}}_{\mathbf{N}}\hat{\mathbf{E}}_{\mathbf{N}}^H\mathbf{a}(\theta,\phi) = \left\|\hat{\mathbf{E}}_{\mathbf{N}}^H\mathbf{a}(\theta,\phi)\right\|. \tag{2.35}$$

© University of Pretoria

The MuSiC null-spectrum function calculates the relation between the incident angle (both azimuth and elevation) and the observed signal; finding the minima of this function will yield the DOA estimation of the L signals.

The spectral MuSiC algorithm searches for the minima of the MuSiC null-spectrum function by guessing and testing multiple values. This method requires much processing and the estimator is limited to the testing values, hence it is in the definition biased to the test value step size. There are many methods for optimising the search of the minima. One such method is to use a tree-type search algorithm, thus reducing the number of values to be tested.

The MuSiC algorithm is a robust DOA estimation method, however it does require the receiver to have a-priori knowledge on the number of signals observed in the ACM, as it influences the assumption of the signal - and noise subspaces. This is often considered as the greatest drawback of MuSiC based DOA algorithms. One method to counter this problem is to estimate the number of signals by exploiting the angular diversity of the array [24–26]
.

Through spectral and temporal filtering, signals can be isolated such that the number of present signals are reduced, thereby improving the performance of the MuSiC algorithm [27]. Further, in the case where the signals are sparse in time or frequency, filtering can lead to the assumption that only one signal can be present, therefore the problem is reduced to single signal detection [28].

2.4.2 Non parameter search algorithms

2.4.2.1 Root-MuSiC

A method of reducing the bias whilst reducing the processing required for the DOA estimation, is the Root-MuSiC algorithm [29]. This algorithm calculates polynomial vector $\mathbf{v}_r$ from the noise subspace:

$$v_r(m) = \sum_{k-l=m} \left[\hat{\mathbf{E}}_{\mathbf{N}}\hat{\mathbf{E}}_{\mathbf{N}}^H\right]_{k,l}. \tag{2.36}$$

Each element in the polynomial vector $\mathbf{v}_r$ is the sum of a diagonal in the matrix $\hat{\mathbf{E}}_{\mathbf{N}}\hat{\mathbf{E}}_{\mathbf{N}}^H$. The roots of the polynomial vector reveal the locations of the stationary points of the MuSiC

© University of Pretoria

null-spectrum function; by selecting the largest root within the unit circle, the DOA can be estimated.

2.4.2.2 Manifold Root-MuSiC

It should be noted that the Root-MuSiC algorithm is only directly applicable to a ULA [30]. If any other antenna array configuration is used, then a transformation matrix should be derived and used to translate the ACM to the equivalent ACM of a ULA. The manifold separation technique approximates the actual $(1 \times N_a)$ steering vector $\mathbf{a}(\theta)$ by the multiplication of a $(N_a \times N_{man})$ transformation matrix $\mathbf{G}$ and a virtual $(N_{man} \times 1)$ steering vector $\mathbf{g}(\theta)$ [31–33]:

$$\mathbf{a}(\theta) \simeq \mathbf{G}\mathbf{g}(\theta). \tag{2.37}$$

The virtual steering vector $\mathbf{g}(\theta)$ is assumed to be that of a ULA:

$$\mathbf{g}(\theta) = \begin{bmatrix} \mathrm{e}^{-\mathrm{j}\frac{N_{man}-1}{2}\theta} & \dots & \mathrm{e}^{\mathrm{j}\frac{N_{man}-1}{2}\theta} \end{bmatrix}^T . \tag{2.38}$$

Through substitution the MuSiC null-spectrum function is redefined :

$$f(\theta) \simeq \mathbf{g}^H(\theta)\mathbf{G}^H\hat{\mathbf{E}}_{\mathbf{N}}\hat{\mathbf{E}}_{\mathbf{N}}^H\mathbf{G}\mathbf{g}(\theta). \tag{2.39}$$

N_{man} should be selected sufficiently large such that the ACM translation is sufficiently accurate for DOA estimation. In the case of UCA, a mathematical transformation can be derived [34]:

$$[\mathbf{G}]_{m,n} = \frac{\mathrm{e}^{\left(\frac{2\pi\,\mathrm{j}(m-N_{man}-1)(n-1)}{N_a}\right)}}{N_a \times \mathrm{j}^{(m-N_{man}-1)} \times J_{(m-N_{man}-1)}\left(\frac{2\pi r}{\lambda}\right)}, \tag{2.40}$$

where $J_m(\cdot)$ is the Bessel function for the first kind of order m. The approximation of the transformation matrix becomes arbitrarily accurate for large N_a. This means that the approximation error approaches zero as N_a increases. The manifold number N_{man} in this case is specified by:

$$N_{man} = \left\lfloor \min\left(\frac{N_a}{2}, \frac{2\pi r}{\lambda}\right) \right\rfloor, \tag{2.41}$$

where $\lfloor \cdot \rfloor$ indicates that the value should be rounded down to the nearest integer.

The transformation matrix is only valid for a large number of antenna elements which is typically not viable for most sensor systems [35].

© University of Pretoria

2.4.2.3 Fourier-Domain Root-MuSiC

The frequency-domain (FD)-Root-MuSiC algorithm, applies the same principal as the Root-MuSiC algorithm, however it estimates the roots through the Discrete Time DFT. For this explanation the elevation angle of $\phi = 0$ is selected, hence it assumes all sources are on the horizontal plane. Further, as only a single angle is estimated, the process is referred to as AOA estimation. The algorithm assumes that the roots F_m are the DFT coefficients of the MuSiC null-spectrum function:

$$f(\theta) \approx \sum_{m=-(M-1)}^{M-1} F_m \mathrm{e}^{\mathrm{j}m\theta} = \hat{f}(\theta). \tag{2.42}$$

If the complex exponential is translated by:

$$z = \mathrm{e}^{\mathrm{j}\theta}, \tag{2.43}$$

then the inverse discrete Fourier transform (IDFT) can be used to approximate the MuSiC null-spectrum function as a polynomial with the coefficients of F_m:

$$f(z) \approx \sum_{m=-(M-1)}^{M-1} F_m z^m = \hat{f}(z). \tag{2.44}$$

To calculate the Fourier coefficients F_m, a $2M - 1$ number of equally spaced azimuth angles:

$$\Delta\theta = \frac{2\pi}{2M-1}, \tag{2.45}$$

are tested in the MuSiC null-spectrum function, and then the coefficients are calculated through the IDFT to obtain:

$$F_m \simeq \sum_{m=-(M-1)}^{M-1} f(m\Delta\theta)\mathrm{e}^{\mathrm{j}m\Delta\theta}. \tag{2.46}$$

The AOA estimation uses the roots to estimate the minima of the MuSiC null-spectrum function. Note that the root selection is done differently compared to the conventional Root-MuSiC algorithm [36]. The roots of this algorithm are either on the unit circle or in reciprocal pairs that are not on the unit circle. To select the roots of this algorithm, select the largest root on, or within, the unit circle. If the root is on the unit circle, average it with the closest root also on the unit circle and use the result to estimate the DOA. If the root is within the

© University of Pretoria

unit circle, then use it directly for the DOA estimation. The roots relate back, through the transformation given in (2.43), to the estimated DOA. For better performance, the MuSiC null-spectrum requires more values to be tested.

The great advantage of the FD-Root-MuSiC is that any antenna array configuration can be used, as the MuSiC null-spectrum function is estimated without the need of mathematical derivation of the steering vector. It does require some values to be tested, but it is considerably less than what is required for the spectral-MuSiC algorithm.

Note that if both the azimuth and the elevation are to be estimated simultaneously the two dimensional DFT can be used. Further, if an array has a symmetrical ambiguity (e.g. an ULA)leading to the MuSiC spectrum to be even, then a discrete cosine transform (DCT) can be used.

2.4.2.4 Fourier-Domain Line-search MuSiC

The disadvantage of the FD-Root-MuSiC algorithm is that it requires polynomial factorisation of order $2M-2$ and some testing of the MuSiC null-spectrum function. As M increases, so does the performance of the algorithm. The order of the polynomial also increases and results in great computational complexity to find the associated roots. It is clear that the processing for this method can quickly become impractical for real-time systems.

As the DFT is used to approximate the roots, the IDFT can in turn be used to re-estimate the MuSiC null-spectrum function. By null-padding the FD-Root-MuSiC polynomial:

$$\breve{F}_m = \begin{cases} F_m & \text{if } m \leq M-1 \\ 0 & \text{if } M-1 < m \leq J-1 \end{cases}, \tag{2.47}$$

and using the IDFT, the MuSiC null-spectrum function can be implicitly interpolated:

$$\breve{f}(z) \approx \sum_{m=-(J-1)}^{J-1} \breve{F}_m z^m = \sum_{m=-(M-1)}^{M-1} F_m z^m. \tag{2.48}$$

The ratio of J to M determines the resolution increase. This allows simple and computationally efficient extrapolation from a few measured data points. As the polynomial factorisation is not required and replaced by a IDFT, this method requires considerable less processing. It should be noted that this method has a bounded RMSE related to the number of IDFT

© University of Pretoria

coefficients J:

$$\min[\mathsf{RMSE}] = \frac{360^\circ}{4 \times (2J-1)}. \tag{2.49}$$

2.4.2.5 Fourier-Domain Weighted Least Squares MuSiC

A close approximation of the MuSiC null-spectrum function at its minima is required for an accurate estimation of the DOA. By considering the FD-Root-MuSiC as a weighted least squares (WLS) problem, the function can be made more sensitive around the minima of the MuSiC null-spectrum function, hence increasing the estimator accuracy [36]. The WLS problem is defined by:

$$\min_{H_m} \sum_{l=1}^{Q} w(\theta_l) \left| f(\theta_l) - \sum_{m=-(M_w-1)}^{M_w-1} H_m \mathrm{e}^{\mathrm{j}m\theta_l} \right|. \tag{2.50}$$

The weights of the function $w(\theta_l)$ is optimally selected as the inverse of the approximated MuSiC null-spectrum function:

$$w(\theta_l) = \frac{1}{f(\theta_l)}. \tag{2.51}$$

The FD-WLS polynomial H_m will be used to determine the roots of the MuSiC null-spectrum function:

$$f(z) = \sum_{m=-(M_w-1)}^{M_w-1} H_m z^m. \tag{2.52}$$

The order of the FD-WLS polynomial $(2M_w - 1)$, should be less than the number of tested values Q, i.e $Q > (2M_w - 1)$.

The WLS problem can be redefined in matrix form (2.53) and is a function of the FD-WLS polynomial $\mathbf{u}$:

$$\min_{\mathbf{u}} \left| \mathbf{W}_\theta^{1/2} (\mathbf{f} - \mathbf{B}\mathbf{u}) \right|^2, \tag{2.53}$$

where the approximated values $\mathbf{f}$ of the MuSiC null-spectrum function:

$$\mathbf{f} = \begin{bmatrix} f(\theta_1) & \cdots & f(\theta_Q) \end{bmatrix}^T. \tag{2.54}$$

is obtained through testing of the DOA values empirically; and the factorised $(Q \times (2M_w - 1))$ WLS steering matrix $\mathbf{B}$:

$$\mathbf{B} = \begin{bmatrix} \mathbf{1}_Q & 2\Re\left\{\tilde{\mathbf{B}}\right\} & 2\Im\left\{\tilde{\mathbf{B}}\right\} \end{bmatrix}, \tag{2.55}$$

© University of Pretoria

is derived from the implicit $Q \times M_w$ WLS steering matrix $\tilde{\mathbf{B}}$:

$$\left[\tilde{\mathbf{B}}\right]_{l,m} = \mathrm{e}^{\mathrm{j}m\theta_l}. \tag{2.56}$$

The $Q \times Q$ weighing matrix is a diagonal matrix and is a function of the approximated MuSiC null-spectrum function and is given by:

$$\mathbf{W}_\theta = \mathsf{diag}\left\{ \begin{array}{ccc} w(\theta_1) & \cdots & w(\theta_Q) \end{array} \right\} = \mathsf{diag}\left\{ \begin{array}{ccc} \frac{1}{f(\theta_1)} & \cdots & \frac{1}{f(\theta_Q)} \end{array} \right\}. \tag{2.57}$$

The FD-WLS polynomial $\mathbf{u}$ can therefore be expressed as a function of the above defined matrices:

$$\mathbf{u} = \left(\mathbf{B}^T \mathbf{W}_\theta \mathbf{B}\right)^{-1} \mathbf{B}^T \mathbf{W}_\theta \mathbf{f}. \tag{2.58}$$

One of the benefits of the FD-WLS polynomial is that the number of empirically tested values is greater than the order of the polynomial, hence a processing reduction is achieved in the polynomial factorisation. The FD-WLS polynomial can either be factorised as in the case of the FD-Root-MuSiC, or be converted back as in the case of the FD Line-search MuSiC algorithm.

2.5 SIGNAL CONDITIONING

The DOA estimation can be improved through additional processing. These processing tasks include: filtering of a signal to isolate it and to reduce the power of out-of-band noise; integrating the data to reduce the variance of the noise; averaging of ACM matrices to improve the approximation; signal deinterleaving methods of the multiple access scheme; and tracking of estimated parameters to enhance the estimation and to stitch the received data through the multiple access scheme. Such processing tasks are usually not regarded as part of the estimation of signal parameters. However they greatly benefit the overall system performance.

Some of these methods are discussed in this section.

© University of Pretoria

2.5.1 Noise reduction

The effects of noise can be minimised through integration of the data. Define a Gaussian random variable X_n with a mean μ_n and variance σ_n^2:

$$X_n \sim \mathcal{N}(\mu_n, \sigma_n). \tag{2.59}$$

Another random variable X_{en} at time sample k can be defined as the average of X_n over N samples:

$$X_{en}[k] = \frac{1}{N}\sum_{l=0}^{N-1} X_n(Nk + l) \tag{2.60}$$

Note that X_{en} will have a data-rate reduction of factor N from X_n [37]. However, the effective mean μ_{en} can be proven to be the same as that of X_n:

$$\mathsf{E}[X_{en}] = \frac{1}{N}\sum_{l=0}^{N-1} \mathsf{E}[X_n] = \frac{1}{N}\sum_{l=0}^{N-1} \mu_n = \mu_n, \tag{2.61}$$

and the effective variance σ_{en}^2 is not the same as that of X_n, but it is related:

$$\mathsf{VAR}[X_{en}] = \frac{1}{N^2}\sum_{l=0}^{N-1} \mathsf{VAR}[X_n] = \frac{1}{N^2}\sum_{l=0}^{N-1} \sigma_n^2 = \frac{\sigma_n^2}{N}. \tag{2.62}$$

This shows that the average of N samples of a Gaussian random variable results in a new Gaussian random variable with the same mean, but with a reduced variance:

$$X_{en} \sim \mathcal{N}(\mu_{en}, \sigma_{en}) = \mathcal{N}(\mu_n, \frac{\sigma_n}{\sqrt{N}}). \tag{2.63}$$

If the received noise in a system follows a zero-mean Gaussian distribution, the power of the noise ($P_n = \sigma_n^2$) is scaled by the number of averaging samples. Therefore, integration gain decreases the effective observed noise. If the noise (independent from the signal, i.e. not correlated), that is added to the signal, has zero mean, and is Gaussian distributed, then it is defined as AWGN.

It should be noted that if the signal is integrated, the noise is reduced at the cost of the bandwidth of the system. The integration of the data is implicitly affected by a finite impulse response (FIR) low pass filter (LPF). Define a discrete input signal $x_i[n]$ which is passed through an averaging filter of L samples to obtain the output $x_o[n]$:

$$x_o[n] = \frac{1}{L}\sum_{l=1}^{L} x_i[n-l] \tag{2.64}$$

© University of Pretoria

The frequency domain output $X_o[\omega]$ of the filter can be determined directly from the frequency domain of the input of the system, $X_i[\omega]$, due to the linearity property of the Fourier transform:

$$X_o[\omega] = \frac{X_i[\omega]}{L} \sum_{l=1}^{L} \mathrm{e}^{-\,\mathrm{j}\omega l}. \tag{2.65}$$

The transfer function $H_f[w]$ of the averaging filter can therefore be determined as:

$$H_f[w] = \frac{X_o[\omega]}{X_i[\omega]} = \frac{\sum_{l=1}^{L} \mathrm{e}^{\mathrm{j}\omega l}}{L} = \frac{\mathrm{e}^{\mathrm{j}\omega\frac{L-1}{2}}}{L} \frac{\sin\left(\frac{\omega L}{2}\right)}{\sin\left(\frac{\omega}{2}\right)}. \tag{2.66}$$

If it is assumed that L is arbitrarily large, the magnitude of the function can then be approximated by:

$$|H_f[w]| \approx \frac{1}{L} \frac{\sin\left(\frac{\omega L}{2}\right)}{\frac{\omega}{2}} = \mathsf{sinc}\left(\frac{\omega L}{2\pi}\right), \tag{2.67}$$

where the sinc-function is defined as:

$$\mathsf{sinc}\,(t) = \begin{cases} \frac{\sin(\pi t)}{\pi t} & t \neq 0 \\ 1 & t = 0 \end{cases}. \tag{2.68}$$

If the ratio between the sampling rate and the bandwidth of the observed signal is less than the number of samples L that are integrated, a portion of the signal bandwidth is lost.

2.5.2 Signal isolation

2.5.2.1 Isolation over multiplexing schemes

There are multiple methods to isolate a signal from a set of signals. Isolating a signal can be done through deinterleaving the multiplexing scheme. Multiplexing schemes can span the following dimensions:

- Time
- Frequency
- Code
- Space

If the signal set uses a time-division multiple access (TDMA) scheme, then signal isolation can be done by identifying and allocating a number of data samples of each signal. This

© University of Pretoria

requires elaborate and accurate synchronisation in time with each of the signals. In a NNC DOA system, the geometry between the receiver system and sources may allow the signals to overlap in time due to the uncontrolled propagation distances, and in return the propagation times.

For frequency-division multiple access (FDMA) based systems, the channels can be separated through filtering by using a bandpass filter (BPF) for each frequency channel. This is a processing intensive task, but it is possible to achieve through the use of channelisers. The inter channel interference (ICI) of this system can be caused by: the side-lobes of the signals interfering if great power difference between signals are present; frequency dispersive channels [38]; and due to frequency reuse allocations. Isolation through filtering is discussed in a later subsection.

In the case of code-division multiple access (CDMA) schemes, the signals are deinterleaved by correlating each received signal with its chip code. The chip code is a pseudo-noise (PN) sequence and should be known by the receiver in order to extract the signal. To achieve DOA estimation, all the codes should be known in order to isolate the different signals. This tends to be a processing intensive task. CDMA signals often lie beneath the noise floor, making them difficult to detect. However it has been proven possible to detect CDMA signals [39, 40].

Lastly, space-division multiple access (SDMA) uses beam-forming to isolate signals in space. DOA estimation is often required for SDMA systems to render the reciprocal task of beam-forming. Beam-forming is used to increase spatial isolation in communication systems. By null-steering or using directional antennas, signals can be isolated in space. The issue however with SDMA systems is that the receiver system should be located at a position to intercept the signal. This is very difficult to achieve, and consequently the POI is greatly reduced for NNC systems. Often the DF system should be mobile in order to manually locate the signals as they are bounded geographically.

2.5.2.2 Filtering

As discussed earlier, a signal set which uses a FDMA scheme or has a finite bandwidth can be isolated through filtering.

© University of Pretoria

If a digital receiver is used, anti-aliasing filtering is essential, as it limits aliasing errors due to out-of-band interference. An anti-aliasing filter is an analogue LPF or BPF, which depends on whether lowpass - or bandpass sampling is used. Once a signal is digitised through the use of an analogue-to-digital converter (ADC), digital filtering can be used to further isolate signals. The number of quantisation levels of a ADC, N_q, determines the dynamic range of the receiver system, and is related to the number of bits b by (2.69) [41]:

$$N_q = 2^b. \tag{2.69}$$

Through the process of digitising a signal, quantisation errors introduce noise into the system. A measure of the best achievable dynamic range is related to the signal-to-quantisation-noise ratio (SQNR) and is dependent of the word-length (number of bits b) of the ADC:

$$\text{SQNR} = 10\log\left(\frac{3\times 2^{2b}}{2}\right) \approx 6.02\times b + 1.76 \quad [\mathsf{dB}]\,. \tag{2.70}$$

A method to increase dynamic range without increasing the number of bits of the ADC is to oversample. For each doubling of the sample-rate, a virtual additional bit can be added to the ADC word length. The effective number of bits b_{ef} is dependent on the actual number of bits b, the sample rate, f_s and the bandwidth of the signal of interest, B_s:

$$b_{ef} = b + \frac{1}{2}\log_2\left(\frac{f_s}{B_s}\right). \tag{2.71}$$

The drawback is that as the sample rate increases, the spurious free dynamic range decreases due to non-ideal effects of the ADC. It should also be noted that as the sample rate increases, so does the thermal noise of the system. Thermal noise, N_{th} is caused by random movement of electrons in an electronic system and is related to the Boltzmann's constant k_b, the absolute temperature T_K, the sample bandwidth B_f and the noise figure F_n of the system according to:

$$N_{th} = k_b \times T_K \times B_f \times F_n. \tag{2.72}$$

If the anti-aliasing filter is shaped to the bandwidth of the signal B_s rather than to the sampling bandwidth B_f, then the thermal noise is not increased through oversampling. This is an efficient method to increase dynamic range of a system. However, if a densely packed

© University of Pretoria

spectrum is to be sampled and a set of signals is to be observed, then the anti-aliasing filter should be designed over the whole bandwidth of interest. Therefore the full noise bandwidth will be sampled. Once a signal is digitised, the out-of-band noise and interference can still be filtered out, but the word-length effects of sampling are permanent.

Filtering can be used to reduce out-of-band noise, but it does not remove in-band noise. Therefore filtering can not completely remove noise from a system. This is an important fact to remember, as aggressive filtering of a signal does not provide a useful benefit.

2.5.2.3 The DFT

DFT can be used to isolate signals which do not overlap in frequency. The DFT can be seen as a NB filter over each frequency tap of the algorithm [41]:

$$\mathbf{X} = \mathfrak{F}\left\{\mathbf{x}\right\} \quad \text{for } X[m] = \frac{1}{K}\sum_{k=0}^{K-1} x[k]\mathrm{e}^{-\frac{2\pi \mathrm{j}km}{K}}. \tag{2.73}$$

A received signal $x[n]$ is composed of a transmitted signal $x_s[n]$ and AWGN signal $x_n[n]$:

$$x[k] = x_s[k] + x_n[k] \tag{2.74}$$

The linearity property of the Fourier transform, and consequently the DFT can be used:

$$X[m] = \mathfrak{F}\left\{x[k]\right\} = \mathfrak{F}\left\{x_s[k]\right\} + \mathfrak{F}\left\{x_n[k]\right\}, \tag{2.75}$$

where $x_n[k]$ is AWGN and therefore stationary in the wide sense. The ensemble autocorrelation of the variable can be determined as being only a function of the variance of the noise:

$$R_{nn}[l] = \mathsf{E}\left[x_n[k]x_n^*[k+l]\right] = \sigma_n^2\delta[l]. \tag{2.76}$$

The power spectral density (PSD) of the noise can be determined through the use of the DFT:

$$S_{xx}[m] = \mathsf{E}\left[X_n^2[m]\right] = \frac{1}{K}\sum_{k=0}^{K-1} R_{nn}[k]\mathrm{e}^{-\frac{2\,\mathrm{j}\pi km}{K}} = \frac{\sigma_n^2}{K}\sum_{k=0}^{K-1}\delta[k]\mathrm{e}^{-\frac{2\pi km}{K}} = \frac{\sigma_n^2}{K}. \tag{2.77}$$

This shows that a reduction of noise per frequency tap, similar to (2.61), is achieved. Therefore the DFT is a simple method for reducing noise through frequency spreading in a system.

© University of Pretoria

The expected received signal is therefore shown to have a constant noise level:

$$X[m] = X_s[m] + \frac{\sigma_n}{\sqrt{K}}. \tag{2.78}$$

A filter is usually applied through the convolution of a signal and the impulse response of the filter. Through the duality principle of the Fourier transform, the process can also be achieved through the multiplication of the frequency response of the filter and the signal. Therefore a DFT can be used to achieve filtering in the frequency domain.

As a filter is applied by the multiplication of each frequency component, it shows that the filter will alter the signal and the noise proportionally. This proves that filtering does not reduce in-band noise.

Redundancy in the processing of a DFT can be removed through the use of a fast Fourier transform (FFT). However, an FFT is optimal when the number of data samples K is a power of 2.

2.5.2.4 Windowing

A DFT uses a finite set of data samples, therefore the frequency content of a signal cannot be accurately represented. If all data samples used in the DFT are selected to have equal weight, a rectangular window of the data is used. The frequency response of a window, defined over a period of T, can be derived as:

$$W_{rec}[m] = \int_{-\frac{T}{2}}^{\frac{T}{2}} \mathrm{e}^{-2\pi \mathrm{j} f t} dt = T\frac{\sin\left(2\pi T f\right)}{2\pi T f} = T\mathsf{sinc}\left(2T f\right). \tag{2.79}$$

The window is multiplied with the data in the time domain, therefore it is convolved in the frequency domain. This means that a window causes frequency dispersion of a signal.

If the input signal is a sinusoid with a frequency f_c that is an integer dividend k of the inverse of the rectangular window period T i.e.:

$$f_c = \frac{1}{k \times T} \;\; ; \quad k \in \mathbb{Z}, \tag{2.80}$$

then the sinusoid will be accurately portrayed, as all the zeros of the window in the frequency domain overlap with the frequency taps of the DFT.

© University of Pretoria

If this condition is not met, then the signal will have a component on all frequency taps, causing interference.

A method to reduce this interference is to use a tapered window. This implies that the frequency response of the window is altered. Table (2.1) shows some popular window methods and the corresponding time domain response.

Table 2.1: Popular Window definitions

Window Type	**Time domain for** $\lvert k\rvert \leq \frac{K-1}{2}$
Rectangular	1
Triangular	$1-\left\lvert\frac{2k}{K-1}\right\rvert$
Hann	$\frac{1}{2}\left(1+\cos\left(\frac{2\pi k}{k}\right)\right)$
Hamming	$0.54+0.46\cos\left(\frac{2\pi k}{k}\right)$
Blackman-Harris	$0.35875-0.48829\cos\left(\frac{2\pi k}{k}\right)+0.14128\cos\left(\frac{4\pi k}{k}\right)-0.01168\cos\left(\frac{6\pi k}{k}\right)$
Gaussian	$\mathrm{e}^{\left(-\frac{\sqrt{2}k\times\beta}{K}\right)^2}$

Windows are often used with DFTs and as a method to approximate a FIR filter more accurately. It should be noted that a window and a filter share common principles, however they differ in application. A filter is applied through a convolution in the time domain and a multiplication in the frequency domain, whereas a window is a multiplication in the time domain and a convolution in the frequency domain. This shows that the two are reciprocal operations of each other. A window is often implemented in conjunction with a filter, however the convolution in the frequency domain is not applied to the signal, hence the window does not cause frequency dispersion of the signal. This distinction is important to understand for system design.

The one sided time domain of the figures are seen in Figure 2.1. The windows are symmetrical, hence only one-sided plotting of the window is shown.

© University of Pretoria

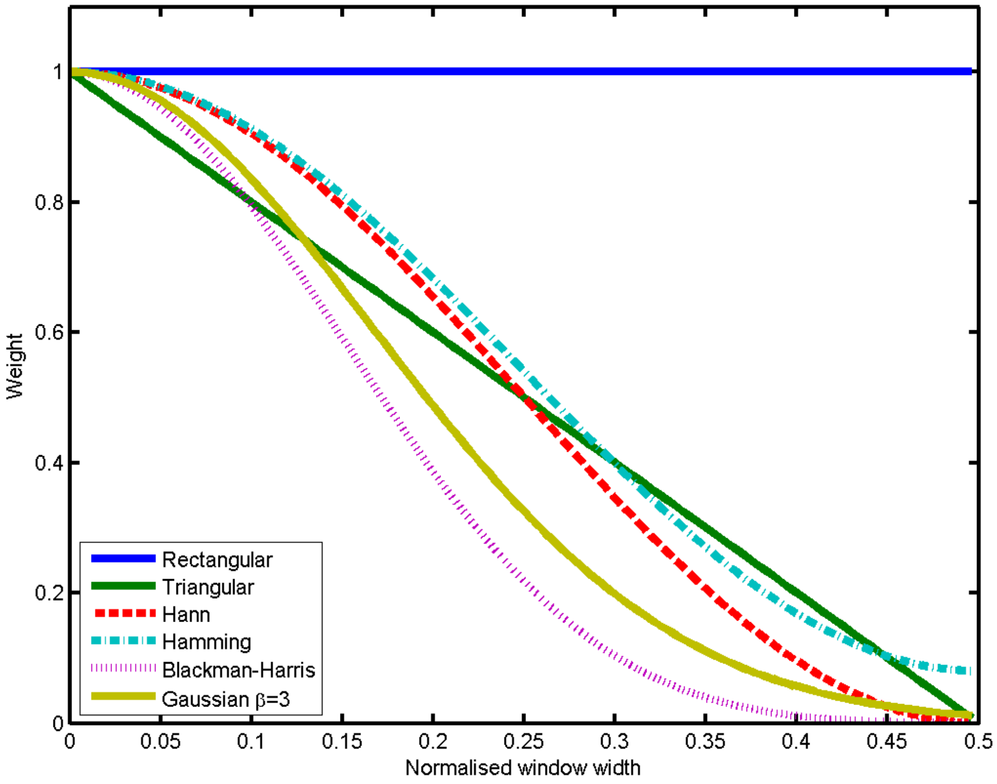

Figure 2.1: Time domain of popular windows.

The tapering implicitly places more emphasis on the data samples in the centre of the data set, hence the data is weighted. If an event of interest in the data (e.g., the start of a communications signal burst) is not located near the center, then its impact is reduced. It should therefore be considered that loss of data sensitivity can be caused by windowing.

The signalling properties of the different windows are difficult to compare in the time domain. The one-sided frequency responses of these windows are shown in Figure 2.2. The frequency axis f_n is normalised to the inverse of the window period T; alternatively it can also be considered as being normalised to the frequency resolution of the DFT, where K is the DFT length and f_s the sample rate:

$$f_n = f \times T = \frac{f \times K}{f_s}. \tag{2.81}$$

The frequency domain of the different windows show that the tapering of the signal reduces the sidelobe level (SLL) of the interference, at the cost of broadening of the main lobe. The

© University of Pretoria

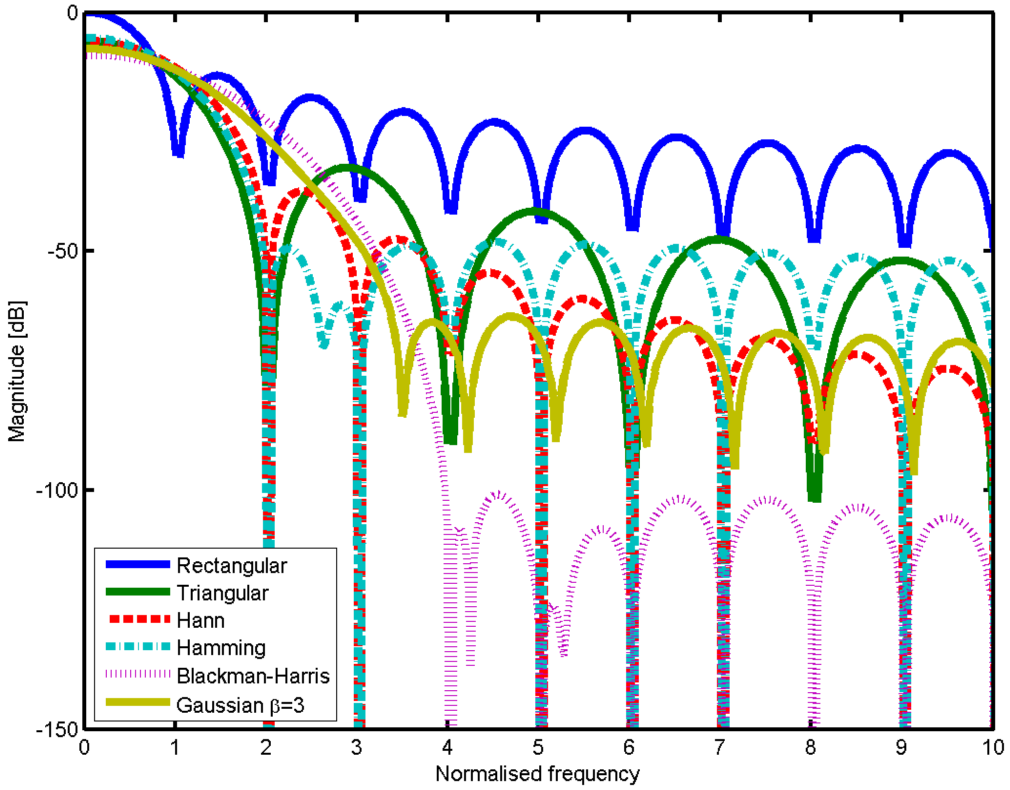

Figure 2.2: Frequency domain of popular windows.

zeros of the windows are often shifted and are therefore not equally spaced with the reciprocal of the window width, hence interference is guaranteed even if the sinusoidal period condition of (2.80) is met.

The benefit of using a window is that the side-lobes are significantly reduced, thus the DFT has less interference from the side-lobes. The trade-off is that the main lobe is broadened, hence the frequency components of signals are spread over multiple near-lying frequency taps.

Windowing can be used as a method to change the properties of a DFT, and hence it is broadly considered as a method to enhance the isolation of FDMA based signals without the use of filtering. On its own windowing has no great benefit, however it can be used as a tool to optimise the performance of filters and transformations.

© University of Pretoria

2.5.3 DOA estimation improvement

DOA estimation through PCA based methods can be improved by increasing the accuracy of the approximation of the ACM. By taking only a single snapshot of the data at time k, the ACM of (2.27) can be expanded:

$$\mathbf{x}(k)\mathbf{x}^H(k) = \mathbf{A}\mathbf{s}(k)\mathbf{s}^H(k)\mathbf{A}^H + \mathbf{A}\mathbf{s}(k)\mathbf{n}^H(k) + \left(\mathbf{A}\mathbf{s}(k)\mathbf{n}^H(k)\right)^H + \mathbf{n}(k)\mathbf{n}^H(k), \tag{2.82}$$

and simplified:

$$\mathbf{x}(k)\mathbf{x}^H(k) = \mathbf{A}\mathbf{s}(k)\mathbf{s}^H(k)\mathbf{A}^H + 2\Re\left\{\mathbf{A}\mathbf{s}(k)\mathbf{n}^H(k)\right\} + \mathbf{n}(k)\mathbf{n}^H(k), \tag{2.83}$$

where $\Re\{\cdot\}$ denotes the real component of a complex signal. The investigation of each component individually shows that the dominant signal terms:

$$\lim_{K\to\infty} \frac{1}{K}\sum_{k=1}^{K} \mathbf{A}\mathbf{s}(k)\mathbf{s}^H(k)\mathbf{A}^H = \mathbf{A}\mathbf{R}_s\mathbf{A}^H, \tag{2.84}$$

and noise terms:

$$\lim_{K\to\infty} \frac{1}{K}\sum_{k=1}^{K} \mathbf{n}(k)\mathbf{n}^H(k) = \sigma_n^2\mathbf{I}, \tag{2.85}$$

tend to the expected values.

The cross terms between the signal and the noise $R_{s|n}$:

$$R_{s|n} = \lim_{K\to\infty} \frac{1}{K}\sum_{k=1}^{K} 2\Re\left\{\mathbf{A}\mathbf{s}(k)\mathbf{n}^H(k)\right\}, \tag{2.86}$$

tend to be negligible, if the signal and the noise is uncorrelated:

$$R_{s|n} = \lim_{K\to\infty} \frac{2}{K}\Re\left\{\mathbf{A}\sum_{k=1}^{K} \mathbf{s}(k)\mathbf{n}^H(k)\right\} \approx 0. \tag{2.87}$$

The expected result tends to what is previously shown:

$$\lim_{K\to\infty} \hat{\mathbf{R}}_x = \mathbf{A}\mathbf{R}_s\mathbf{A}^H + \sigma_n^2\mathbf{I} = \mathbf{R}_x. \tag{2.88}$$

This means that as the number of samples increases, the estimation tends towards the expected value. The expected values of the signal cross term $R_{s|n}$ is defined as:

$$\mathrm{E}\left[R_{s|n}\right] = \frac{2}{K}\Re\left\{\mathbf{A}\sum_{k=1}^{K} \mathrm{E}\left[\mathbf{s}(k)\right]\mathrm{E}\left[\mathbf{n}^H(k)\right]\right\}. \tag{2.89}$$

© University of Pretoria

It shows that $R_{s|n}$ tends to zero if the signal is uncorrelated with AWGN:

$$\mathrm{E}\left[R_{s|n}\right] = \frac{2}{K}\Re\left\{\mathbf{A}\sum_{k=1}^{K}\mathrm{E}\left[\mathbf{s}(k)\right]\times 0\right\} = 0 \tag{2.90}$$

The variance of the cross term is a function of the multiplication variance of the noise and the signal:

$$\mathrm{VAR}\left[R_{s|n}\right] = \frac{2}{K^2}\Re\left\{\mathbf{A}\sum_{k=1}^{K}\mathrm{VAR}\left[\mathbf{s}(k)\mathbf{n}^H(k)\right]\right\}. \tag{2.91}$$

If the noise is assumed to be AWGN, and the signal has a zero mean and a variance equal to the power of the signal P_s , the combined variance of the noise and the signal can be derived as:

$$\begin{aligned}\mathrm{VAR}\left[\mathbf{s}(k)\mathbf{n}^H(k)\right] = {} & \mathrm{VAR}\left[\mathbf{s}(k)\right]\mathrm{VAR}\left[\mathbf{n}^H(k)\right] + \mathrm{VAR}\left[\mathbf{s}(k)\right]\mathrm{E}\left[\mathbf{n}^H(k)\right]^2 \\ & + \mathrm{VAR}\left[\mathbf{n}^H(k)\right]\mathrm{E}\left[\mathbf{s}(k)\right]^2. \end{aligned} \tag{2.92}$$

It is assumed that the signal has a variance equal to the power of the signal P_s:

$$\mathrm{E}\left[\mathbf{s}^2(k)\right] = P_s, \tag{2.93}$$

and, if the noise is assumed to be AWGN:

$$\mathrm{E}\left[\mathbf{n}^H(k)\right]^2 = 0\ , \quad \mathrm{VAR}\left[\mathbf{n}^H(k)\right] = \sigma_n^2, \tag{2.94}$$

then the combined variance of the noise and the signal obtained through substitution results in:

$$\mathrm{VAR}\left[\mathbf{s}(k)\mathbf{n}^H(k)\right] = \sigma_n^2\left(\mathrm{VAR}\left[\mathbf{s}(k)\right] + \mathrm{E}\left[\mathbf{s}(k)\right]^2\right), \tag{2.95}$$

and in:

$$\mathrm{VAR}\left[\mathbf{s}(k)\mathbf{n}^H(k)\right] = \sigma_n^2\left(\mathrm{E}\left[\mathbf{s}^2(k)\right] - \mathrm{E}\left[\mathbf{s}(k)\right]^2 + \mathrm{E}\left[\mathbf{s}(k)\right]^2\right) = \sigma_n^2 P_s. \tag{2.96}$$

The cross term $R_{s|n}$ can now be determined, and has a variance related to the signal and noise powers, as well as the number of snapshots taken:

$$\mathrm{VAR}\left[R_{s|n}\right] = \frac{2\sigma_n^2 P_s}{K}\Re\left\{\mathbf{A}\right\}. \tag{2.97}$$

Increasing the number of snapshots improves the approximation of the ACM, and in return the estimation is improved. It can therefore be concluded that multiple snapshots of data is required to reliably approximate the ACM, and to have acceptable results.

© University of Pretoria

2.5.4 Estimation Tracking

Multiple DOA estimated values can be combined to increase the estimated parameter. A Kalman filter is a popular technique and can be used for multiple tasks, such as tracking and estimation improvement.

A Kalman filter, also referred to as linear quadratic estimation (LQE), uses a series of measurements or estimations to recursively estimate the underlying state of the system. The Kalman filter consists of two stages: a prediction stage and an update state. During the prediction stage the filter estimates what the next value will be based on previous data. During the update stage a new measurement is used to update the filter parameters by comparing the measurement to the predicted values. It is proven that if the underlying system is accurately known, a Kalman filter has optimal performance.

The disadvantage of using a Kalman filter is that a good estimation of the noise of the system is normally required for optimal performance. However, there are methods that do not have this requirement [42,43]. To obtain satisfactory performance, the Kalman filter requires some convergence time. In the case of signalling systems that reconfigure rapidly (e.g. dynamic resource allocation, frequency hopping, pulse staggering) or systems with short burst-like transmission, the required convergence time may not be available. Furthermore, some tracking of a signal within a multiplexing scheme is required to achieve efficient estimation.

Alternatively, if it is assumed that the signal source and the sensor system are both stationary, then consecutive measurements can be integrated; or if multiple signals are transmitted from the same source and have an accessible multiplexing scheme, the DOA of each individual signal can be integrated:

$$\hat{\theta}_{post} = \frac{1}{K} \sum_{k=1}^{K} \hat{\theta}. \tag{2.98}$$

The new estimator will be biased if the original value is biased. Similarly it will be unbiased if the original values are unbiased. The variance of the estimator is reduced by the number of estimated values averaged:

$$\text{VAR}\left[\hat{\theta}_{post}\right] = \frac{\text{VAR}\left[\hat{\theta}\right]}{K}. \tag{2.99}$$

Therefore the RMSE will also reduce proportionally.

© University of Pretoria

The issue however with DOA estimation is that if multiple interfering signals are observed, or if the noise is not AWGN, or if the signals are correlated, it may cause the DOA estimation to lock onto the wrong minima of the MuSiC null-spectrum function. DOA estimation on the wrong signal results in large biased errors. If one of these wrong estimated values is summed with correct estimated values, it may seriously jeopardise the performance of the newly defined estimator. Further, in the case that the DOA of multiple signals are simultaneously estimated through the same process (e.g. FDMA separation using DFT), then the same lock - whether correct or not - tends to be achieved over all signals from the same source. Thus summing of estimated values in non-ideal situations will result in no performance improvement at all.

A further issue is that both the azimuth and the elevation angles wrap around. Thus wrapping errors should be removed before summing, as this will result in very high RMSE values due to the 360° phase shifts in the estimated values.

A weighting function can be used instead of direct averaging, in an attempt to improve estimation reliability. Take for example a FDMA multiplexing scheme that uses a number of adjacent frequency channels. The channels on the edges will be more prone to interference caused by neighbouring signals, than those in the center channels, hence more weight can be applied to the values in the center channels than those one the edges.

It is therefore possible to decrease the RMSE of the estimated values through post-estimation integration; however there are multiple obstacles that can reduce the success thereof.

2.5.5 Integration gain in a DF system

Integration gain is the process of increasing the performance of a system through the integration of data. In the case of PCA based DOA estimation system there are three possible methods of integration: pre-DOA (signal isolation and noise reduction) integration, DOA improvement integration (increase approximation accuracy of the ACM), and post estimation integration (combining multiple estimated values).

Pre-DOA integration is processing that isolates the signal of interest, this may include filtering and decimation. It should be noted that filtering reduces the total SNR of the signal of

© University of Pretoria

interest by reducing out-of-band interference and noise. Oversampling of a signal can be used to increase the dynamic range of a digital receiver. The benefit of pre-DOA integration is that high sample-rates can be used and reduced through integration before the DOA estimation is performed; thus less processing on later stages, like eigenvalue decomposition or polynomial factorisation, is required. Data-rate reduction, memory restrictions and processing restrictions are the main reasons to use pre-DOA integration, as it relieves these limitations from later processing tasks.

DOA improvement integration focuses on improving the approximation of the ACM. Using a single snapshot of data is suboptimal, as large errors may be present. However increasing the number of snapshots quickly improves ACM approximation. Once the approximation of the ACM is sufficiently accurate, then further integration will yield no useful improvement, as it requires additional processing which can rather be utilised efficiently on other tasks. DOA improvement integration improves the ACM estimation but does not reduce the noise within the ACM. Therefore it is important to use DOA improvement integration to get a good approximation of the ACM, however aggressive integration on this level has no useful benefits.

Post estimation integration usually requires multiple DOA estimates; hence it implies that more processing is required on earlier stages. This form of integration is not always available due to the processing architecture, and it is not always optimal as previously discussed. An effective application for post estimation integration is with signal detection and classification. If multiple signals are classified as being from the same source, then their individual DOA estimated values can be added together to improve accuracy. It should be noted that this will be highly dependent on the implementation of the classification algorithm.

A combination of all these integration methods will result in optimal system performance. The system requirements should be analysed to determine where integration should be implemented and how intense the integration should be. For example, if the data-rate and processing are limiting factors, the integration will be moved to earlier stages in the processing chain.

All methods of integration have some sort of performance increase in the system. There are many limitations concerning implementation of these methods, such as signals of interest, sig-

© University of Pretoria

nal bandwidth, multiple access scheme of the signal, available processing, data-rate, available memory, sensor and receiver architecture, and what output is required.

As an example, in the case of bi-static radar, the majority of processing is focused on generating the amplitude-range-Doppler (ARD) map and target detection. Assuming an ARD per sensor is generated, and the DOA is to be performed on the ARD data, then the detected target on the ARDs is highly isolated in both range and Doppler (great pre-DOA estimation integration), this however leaves no room for DOA improvement integration and only target tracking is available for post estimation signal processing.

2.6 THE LTE SPECIFICATION

The LTE specification will be discussed in this section.

2.6.1 History and requirements

LTE is a cellular communication standard which complies to the International Telecommunication Union radio-communications Sector (ITU-R) specifications for International Mobile Telecommunications Advanced (IMT-A). The LTE specifications are open-source and are maintained by 3rd Generation Partnership Project (3GPP) [44]. LTE is often referred to as a 4G technology, however it does not meet all the specifications to be classified as a 4G technology. Long-Term Evolution Advanced (LTE-A) is an extended version of LTE, and does meet all 4G specifications.

LTE was developed to satisfy the need for greater data-rates, improved system capacity and reduced latency for cellular networks [45]. The data-rate requirement for LTE include a peak data-rate of 100 Mbps for the down-link (DL), and 50 Mbps for the up-link (UL), using a 20 MHz signal bandwidth. The first proposition for LTE was made by Nippon Telegraph and Telephone (NTT) Do Communications over the Mobile-network (DoCoMo) [46], with the intent of making it an international standard. The first LTE network was launched on 14 December 2009 by the mobile operator TeliaSonera in the cities of Oslo and Stockholm [47]. On 14 July 2011 the first LTE network was launched in South Africa by the mobile operator Mobile Telephone Network (MTN) in the Gauteng province [48].

© University of Pretoria

There are 44 Evolved Universal Terrestrial Radio Access (E-UTRA) operational bands that are specified for use by LTE systems [44]. As each geographical region may have different spectral allocations, applicable E-UTRA operational bands can be utilised for each region. Therefore the adoption of LTE systems are simple and for diverse and densely packed spectra. The operational bands range from 452.5 MHz (Band No. 31) to 3.8 GHz (Band No. 43). Hence LTE systems should require a great frequency range for operation.

2.6.2 Structure of the physical layer

The LTE specification supports two duplexing modes: frequency-division duplex (FDD) and time-division duplex (TDD) [20]. FDD can support either full or half duplexing, and TDD is available only for half duplexing. Table 2.2 shows the structure definitions for the time frame structure. It should be noted that all timing in the LTE specification is measured in the time unit T_s, as defined in Table 2.2.

Table 2.2: Time frame structure of Type 2 (TDD) for LTE from [20].

Name	**Variable**	**duration**	**No. of T_s**	**No. of T_{slot}**
Time unit	T_s	32.55 ns	1	1/15360
Time slot	T_{slot}	0.5 ms	15 360	1
Subframe	T_{sf}	1 ms	30 720	2
Half frame	T_{hf}	5 ms	153 600	2
Radio frame	T_f	10 ms	307 2010	20

The frame structure is shown in Figure 2.3.

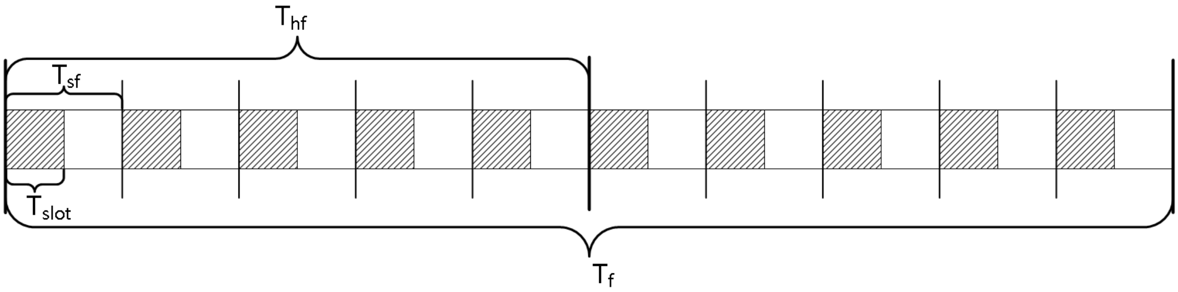

Figure 2.3: Time frame structure for LTE. Adapted from 3GPP [20], with permission.

© University of Pretoria

The frame structure of Type 1 is used for the FDD duplexing mode [20]. The frequency separation in FDD between the UL and DL is specified for each E-UTRA operational band and ranges from 10 MHz (Band No. 31) to 400 MHz (Band No. 4 and 10) [44].

The frame structure of Type 2 is used for the TDD duplexing mode [20]. The TDD configuration is half duplexing system, therefore the same radio channel is used for both the UL and DL. The switching patterns between the UL and DL are divided into sections of subframe $T_{sf} = 1$ ms length; and these patterns are defined in the specification for either a half frame $T_{hf} = 5$ ms or radio frame $T_f = 10$ ms intervals.

The modulation for the LTE DL is OFDM, and single-carrier frequency division multiple access (SC-FDMA) is used for the UL. Both methods are FDMA based, hence they allow the spectrum of a channel to be divided between various users. A resource block (RB) contains 12 sub-carriers, each with a inter-carrier spacing of 15 kHz. The bandwidth of a RB is therefore 180 kHz. A RB spans a full timeslot T_{slot} of 0.5 ms. The base-station, named an Evolved Node B (eNodeB), assigns RBs to each user. The RB allocation can be dynamically changed by the eNodeB within a subframe T_{sf}, to efficiently manage the spectral resources.

The transmission bandwidth for an LTE channel is scalable, to allow efficient deployment according to the available spectrum for the said channel. The transmission bandwidth is the allocated bandwidth for the channel. Each channel has an associated number of RBs for its specified transmission bandwidth. To minimise interference between channels, a guard band is implemented, therefore the data bandwidth is narrower than the transmission bandwidth. The digital sample rate is greater than the transmission bandwidth to ensure that the analogue full bandwidth is achievable, this also reduces interference due to non-ideal effects of the transmitter. In both OFDM and SC-FDMA an inverse fast Fourier transform (IFFT) is used to modulate (and FFT to demodulate) the data onto the respective carriers. The IFFT length is determined by the transmission bandwidth, the number of RBs and the sample rate. A more detailed discussion on the modulation will be given in the subsequent section. The occupied carriers per symbol are the non-zero FFT taps. All these values are shown in Table 2.3 for the respective channel sizes.

Through carrier aggregation the transmission bandwidth can be increased by grouping mul-

© University of Pretoria

Table 2.3: Structural specifications of LTE from [20].

Parameter	**Values**					
Transmission bandwidth [MHz]	1.4	3	5	10	15	20
Data bandwidth [MHz]	1.08	2.7	4.5	9	13.5	18
Number of resource blocks	6	15	25	50	75	100
FFT size	128	256	512	1024	1536	2048
Sampling rate [MHz]	1.92	3.84	7.68	15.36	23.04	30.72
Occupied sub carriers per symbol	76	151	301	601	901	1201

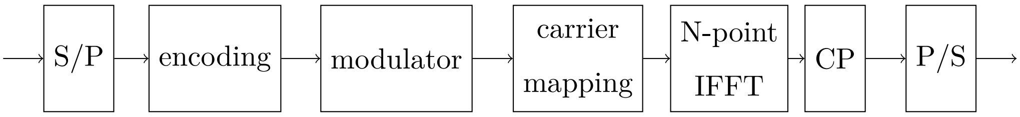

Figure 2.4: Block diagram of the DL modulation of the LTE. Adapted from 3GPP [20], with permission.

tiple channels together [49]. This allows superior data transmission, and allows LTE-A to be classified as a 4G system, even though the base specification of LTE is not.

2.6.3 Modulation, data-mapping and encoding

The DL of LTE uses OFDM. OFDM modulates multiple carriers simultaneously through the use of an IFFT. The IFFT ensures that the sub-carriers are orthogonal relative to each other. ICI between the carriers is minimised by the orthogonality of the system. Spectral efficiency can be improved by a multi-carrier system with closely placed orthogonal carriers. The base modulation used for each carrier can be amplitude-shift keying (ASK), phase-shift keying (PSK) or a combination of the two. The block diagram of the DL is shown in Figure 2.4.

In the physical layer of the DL, the input data stream is first passed thorough a serial-to-parallel (S/P) converter, to allow parallel processing for greater efficiency. The data is then encoded, with a cyclic redundancy check (CRC) code of length 24; and a parallel concatenated convolutional code (PCCC) turbo encoder which consists of two 8-state constituent encoders and a turbo code interleaver [50]. The code-rate R_c of the PCCC is $\frac{1}{3}$, this means that the

© University of Pretoria

output data-rate of the encoder is three times greater than the input data-rate. As part of the encoding, the data is scrambled; this is done to remove any patterns in the data that can result in unwanted frequency responses once modulated. Scrambling therefore artificially increases the randomness of the signal. A scrambler uses a Gold-sequence of length 31.

The DL of LTE uses binary phase-shift keying (BPSK), quadrature phase modulation (QPSK), 16-quadrature amplitude modulation (QAM), 64-QAM and 256-QAM as base modulation types. BPSK is used for equalisation and protocol overhead, hence it is not used for transmission of the message data. The number of symbols per modulation scheme is shown in Table 2.4. The base modulation is selected for the current function of the RB, and the quality of service (QoS) as reported by the receiver. The QoS is dependent on the transmitter-receiver separation distance, the channel, interferences from other sources and the noise level of the receiver. The modulation scheme with the highest data-rate (i.e. the modulation scheme with the greatest number of symbols and hence the greatest spectral efficiency) that provides a satisfactory bit error rate (BER) for reliable communication, is selected. The errors introduced in the communication system can be detected and in many cases corrected by the decoding of the data, hence the encoding improves the BER of the system at the cost of reducing the system capacity.

Table 2.4: Number of modulated symbols per modulation scheme

Modulation type	**No. of symbols**
BPSK	$2^1 = 2$
QPSK	$2^2 = 4$
16-**QAM**	$2^4 = 16$
64-**QAM**	$2^6 = 64$
256-**QAM**	$2^8 = 256$

A cyclic prefix (CP) is added to each OFDM symbol, to allow synchronisation of the symbols between the transmitter and receiver. A CP is simply a section of the OFDM symbol that is repeated, therefore slightly increasing the symbol length and adding redundancy. A diagram of the CP is shown in Figure 2.5. The CP is used as a guard interval to reduce inter-symbol interference, and it is also used to reduce the effects of frequency-selective fading in non-ideal transmission channels. The CP is added redundancy in the system to make the

© University of Pretoria

communication system more robust. It should be noted that the CP changes the PSD of each carrier in the OFDM structure, hence orthogonality is lost unless symbol-synchronisation is achieved at the receiver.

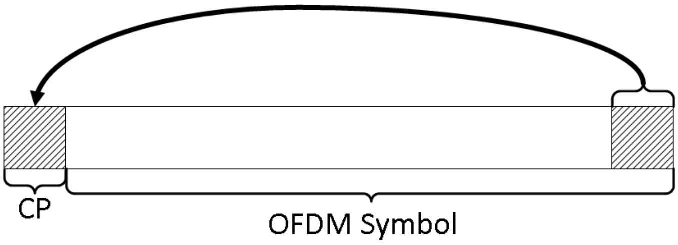

Figure 2.5: CP structure for LTE.

LTE has two configurations for the CP: normal - and extended CP operation [20]. In the normal CP configuration, there are 7-OFDM symbols per timeslot T_{slot}. It is assumed that the inter-carrier spacing of 15 kHz is used, and therefore the first symbol has a CP of $160 \cdot T_s \approx 5.2\ \mu s$, and the other 6 symbols have a CP of $144 \cdot T_s \approx 4.7\ \mu s$. In the extended CP, either 6 OFDM symbols each with a inter-carrier spacing of 15 kHz and a CP of length $512 \cdot T_s \approx 16.7\ \mu s$; or 3 OFDM symbols each with a inter-carrier spacing of 7.5 kHz and a CP of length $1024 \cdot T_s \approx 16.7\ \mu s$ is used. The percentage overhead of the CP is 7.14% for normal CP, and 25% for extended CP.

A root raised cosine (RRC) filter is used shaped to the transmission bandwidth before the OFDM signal is transmitted [51].

A resource element (RE) is a subsection of a RB. The number of REs is the product of the number of OFDM symbols and the number of carriers per RB. As an example, in normal CP operation, there are $7 \times 12 = 84$ REs per RB. The reference signals, and the modulated data are mapped to each RE. The reference signals are used for signal equalisation, and to network specific information. An example of a RB for normal CP operation is shown in Figure 2.6.

The UL of LTE uses SC-FDMA, and is very similar to the DL. The block diagram of the UL is shown in 2.7. The only difference is that an additional DFT is used in the transmission chain. This is done to reduce the peak-to-average-power ratio (PAPR) of the communication signal in comparison to OFDM. A large PAPR makes it difficult to span the full dynamic range of analogue amplifiers effectively as the average power does not get amplified greatly;

© University of Pretoria

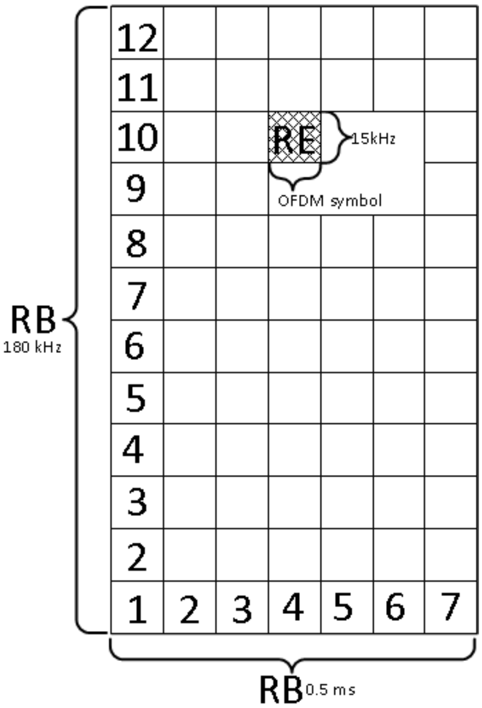

Figure 2.6: RB definition for normal CP configuration. Adapted from 3GPP [20], with permission.

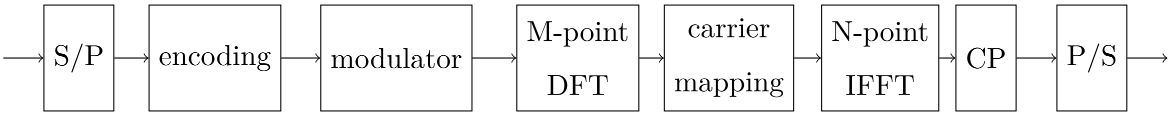

Figure 2.7: Block diagram of the DL modulation of the LTE. Adapted from 3GPP [20], with permission.

as a consequence the non linearities of the amplifiers distort the peaks in an OFDM system. SC-FDMA is selected for the user equipment (UE) as it has similar performance to OFDM with the benefit of reduced radio frequency (RF) hardware requirements.

The UL only uses QPSK, 16-QAM and 64-QAM for data modulation, and hence it does not have the same maximum data-rate capabilities as compared to the UL. The UE has significantly less transmission power (designed for longer battery life of devices), hence it cannot guarantee sufficient SNR at the eNodeB to compare with the DL data-rates.

© University of Pretoria

2.6.4 Handset requirements

The maximum transmission power of a UE for any transmission bandwidth is 23 dBm (0.2 W) [44] with a tolerance of ±2 dB. The minimum output power for a UE is −40 dBm. The power and timing delay as received by the eNodeB, is measured and used to adjust the settings of the UE. The power is adjusted to ensure that the eNodeB has a received SNR sufficient for reliable communication, whilst reducing inter-cell interference to other eNodeBs.

2.6.5 Direction finding in LTE

LTE utilises MIMO communications technology, which makes use of multiple antennas to implement spatial multiplexing in order to increase system capacity [50]. Improved DF and spatial multiplexing methods for LTE have been proposed by Bartoli et al. [6] to reduce interference, therefore increasing system performance. Parametric estimation techniques, which include DF, have been studied and implemented on LTE systems [52]. MIMO communications already use an array of antennas; therefore the antenna infrastructure is already in place for DF with interferometry.

2.7 CHANNEL MODELS

Radio propagation testing guidelines are standardised by International Telecommunication Union (ITU) [53] and adapted by the European Telecommunications Standards Institute (ETSI) for LTE [54]. Further specifications for MIMO channels are also developed by ETSI [55].

Small-scale fading describes the rapid changes in signal strength over small distance. These distances usually in the order of a few wavelengths. Multipath propagation, the relative velocity between the transmitter and receiver and the velocity of path scatterers in the environment are the sources of small-scale fading. These effects are more prone in urban areas as it is caused by reflections off buildings and moving vehicles.

Small-scale fading effects include time and frequency dispersion. The EM signal follows multiple routes as it journeys from the transmitter to the receiver, therefore multiple copies

© University of Pretoria

of the signal–each with a a different time delay and amplitude–is measured by the receiver, this is known as time dispersion. The sum of these signals is referred to as multipath, as the signal uses multiple paths to propagate. The various time-delayed signals interfere with each other and cause certain frequencies to be attenuated more than others, hence selective fading occurs. Frequency dispersion is caused by Doppler shifts on the signal. The Doppler shift is caused by relative movement between a transmitter-receiver pair, as well as any movement from multipath reflectors in the environment. Frequency dispersion can be considered as a random frequency modulation of the signal. Small scale fading thus results in delay and Doppler spread.

A fading channel model incorporates effects of multipath, Doppler frequency shift and noise. As a multipath component comprises of a time delay and change of amplitude of the original signal, it can be simulated through the use of an appropriately weighted tapped delay-line. A digital FIR filter can therefore be used to simulate multipath components. The Doppler frequency shift can be incorporated by multiplying each multipath signal with a Rayleigh or Rician distributed variable. A Rician channel has the characteristics of a Rayleigh channel with an added line of sight (LOS) path signal. Lastly, AWGN can be added to emulate noise effects.

Three models specified by ETSI is extended pedestrian A (EPA), extended vehicular A (EVA) and extended typical urban (ETU). The delay and relative magnitude of each multipath component for these channels are shown in Table 2.5. These channel models are also used for LTE system evaluation [56].

The Doppler spread of these channels have the classical Doppler spectrum, if omnidirectional antennas are assumed:

$$S(f) \propto \frac{1}{\sqrt{1-\left(\frac{f}{f_D}\right)^2}} \text{ for } f \in (-f_D, f_D)\,. \tag{2.100}$$

The maximum Doppler frequency f_D is specified as 0 Hz, 5 Hz, 70 Hz and 300 Hz respectively for the standard ETU channels [56]. The AWGN noise follows a Gaussian probability density function (PDF), as described in equation:

$$p_{gaus}(r) = \frac{1}{\sqrt{2\pi}\sigma} \mathrm{e}^{-\frac{(r-\mu)^2}{2\sigma^2}}, \tag{2.101}$$

© University of Pretoria

Table 2.5: Summary of ETSI Multipath channel models, with delay of each tap t_{del} in ns and the relative power P_{rel} of each tap.

-	EPA		EVA		ETU	
Tap	t_{del} [ns]	P_{rel} [dB]	t_{del} [ns]	P_{rel} [dB]	t_{del} [ns]	P_{rel} [dB]
1	0	0.0	0	0.0	0	-1.0
2	30	-1.0	30	-1.5	50	-1.0
3	70	-2.0	150	-1.4	50	-1.0
4	90	-3.0	310	-3.6	50	-1.0
5	110	-8.0	370	-0.6	50	-1.0
6	190	-17.2	710	-9.1	50	-1.0
7	410	-20.8	1090	-7.0	50	-1.0
8	-	-	1730	-12.0	50	-1.0
9	-	-	2510	-16.9	50	-1.0

where r is the amplitude, μ is the mean and σ is the standard deviation.

Fading channels introduces time and frequency dispersion. Rayleigh and Rician channels describe the statistical time varying nature of a flat fading signal. A Rician fading channel is defined as a Rayleigh fading channel with an added LOS component. The probability density function (PDF) of a Rayleigh distribution is defined as:

$$p_{Ray}(r) = \begin{cases} \frac{r}{\sigma^2} e^{\frac{-r^2}{2\sigma^2}} & 0 \leq r \leq \infty \\ 0 & r < 0 \end{cases}, \tag{2.102}$$

and the PDF of a Rician distribution is defined as:

$$p_{Rice}(r, A) = \begin{cases} \frac{r}{\sigma^2} e^{-\frac{r^2+A^2}{2\sigma^2}} \mathbf{J}_0\left(\frac{Ar}{\sigma^2}\right) & 0 \leq r \leq \infty \text{ and } 0 \leq A \\ 0 & r < 0 \end{cases}. \tag{2.103}$$

The variable A is the peak amplitude of the LOS signal in a Rician channel, K is the ratio between the deterministic signal power and the variance of the multipath, and is known as the Rician factor.

Spatial channel models are specified by ETSI for AOA [57]. These channel model are used for link testing of mobile communications systems. Advanced channel models which incor-

© University of Pretoria

porate large-scale fading, small scale fading, antenna modelling, array coupling, and spatial modelling of the transmitter and receiver are developed and specified in the LTE specification [58].

2.8 OPTIMISATION

In system design multiple parameters should be selected. The problem however is to select the parameters to have an optimal outcome. If multiple system parameters influence a single system outcome, the outcome cannot be optimised through individual parameter optimisation as the parameters are not isolated from each other. Therefore to optimise the system, the joint outcome of the parameters should be optimised.

Pareto optimisation is a optimisation theory used in economics to improve the economic-output on a system level [59]. Pareto optimisation is used in mathematical programming as a method to achieve best results of a multi-object system. The aim of Pareto optimisation is not to obtain a single solution, but rather to obtain a set of compromise solutions. This is beneficial as many system outputs are conflicting in nature and a optimal solution does not exist. This allows a greater scope of optimality in system design, even though complete satisfaction of each output is not achievable. The set of solutions are optimal in trade-off of characteristics and should be Pareto efficient.

A selection of parameters results in a Pareto efficient object if the outcomes of the object cannot be improved without worsening any other outcome of the system [60]. Likewise, a Pareto inefficient object is a system that can be improved in any way without degrading any other section of the system. A set of Pareto efficient objects form a Pareto front. All of the objects on the front are regarded as the optimal solutions to the system.

A tutorial on Pareto optimisation is provided in Appendix A for the interested reader.

© University of Pretoria

CHAPTER 3

PROBLEM ANALYSIS

3.1 CHAPTER OVERVIEW

This chapter investigates the problems associated with NNC DF of OFDM based cellular signals.

3.2 OFDM BASED SIGNAL ANALYSIS

OFDM is stated as being an FDMA scheme that uses perfect orthogonal carriers, hence interference is minimised. This allows carriers to be placed at a minimum distance apart to increase the system capacity. It is a popular modulation scheme used in modern communication systems [61].

3.2.1 Loss of Orthogonality from the CP

This section investigates the orthogonality of an OFDM symbol with an added CP.

The m-th modulated carrier $X_{OFDM}[m]$, with the complex amplitude A_m that is normalised by the intended OFDM symbol length T_{sym} is defined as [61]:

$$X_{OFDM}[m] = \frac{A_m}{T_{sym}}. \tag{3.1}$$

The discrete time definition $x_{OFDM}[n]$ is the IDFT (denoted by $\mathfrak{F}^{-1}\{\cdot\}$) of the N_{sym} modulated carriers, and is a function of the sample period T_s and the frequency spacing of the carriers f_{sym}:

$$x_{OFDM}[n] = \mathfrak{F}^{-1}\left\{X_{OFDM}[m]\right\} = \sum_{k=0}^{N_{sym}-1} \frac{A_k}{T_{sym}} \times \mathrm{e}^{2\pi\, \mathrm{j} n T_s k f_{sym}}. \tag{3.2}$$

$x_{OFDM}[n]$ is assumed to be an infinite time function. If a symbol is only present for a duration of the intended OFDM symbol length T_{sym} and starts at time T_0, the discrete finite signal $x^{IS}_{OFDM}[n]$ is defined as:

$$x^{IS}_{OFDM}[n] = x_{OFDM}[n] \times \Pi\left(\frac{nT_s - T_0}{T_{sym}}\right), \tag{3.3}$$

where the rectangular function is denoted by $\Pi(\cdot)$:

$$\Pi\left(\frac{t}{\tau}\right) = \begin{cases} 1 & \text{for } |t| \leq \frac{\tau}{2} \\ 0 & otherwise \end{cases}. \tag{3.4}$$

The function can be expanded to be continuous in time:

$$x^{IS,CT}_{OFDM}(t) = \left[\sum_{k=0}^{N_{sym}-1} \frac{A_k}{T_{sym}} \times \mathrm{e}^{2\pi\, \mathrm{j} t k f_{sym}}\right] \times \Pi\left(\frac{t - T_0}{T_{sym}}\right). \tag{3.5}$$

The frequency content of the signal can be obtained through the Fourier transform:

$$X^{IS,CT}_{OFDM}(f) = \left[\sum_{k=0}^{N_{sym}-1} \frac{A_k}{T_{sym}} \delta\left(f - n f_{sym}\right)\right] * T_{sym}\mathsf{sinc}\left(f T_{sym}\right) \times \mathrm{e}^{-2\pi\, \mathrm{j} f T_0}, \tag{3.6}$$

and can be further simplified:

$$X^{IS,CT}_{OFDM}(f) = \sum_{k=0}^{N_{sym}-1} A_k \mathsf{sinc}\left((f - n f_{sym}) T_{sym}\right) \times \mathrm{e}^{-2\pi\, \mathrm{j}(f + n f_{sym}) T_0}. \tag{3.7}$$

It can be derived that the functions are only orthogonal if the symbol period is the reciprocal of the frequency spacing:

$$f_{sym} = \frac{1}{T_{sym}}. \tag{3.8}$$

This shows that if a CP is added to the symbol (hence the effective symbol period is increased), the carriers will interfere with each other:

$$f_{sym} \neq \frac{1}{T_{sym}} = \frac{1}{T_{sym} + T_{CP}}. \tag{3.9}$$

Therefore symbol synchronisation and accurate sampling of the data is crucial for an OFDM system to operate.

© University of Pretoria

This point illustrates that if a NNC system is implemented, it uses a number of data points equal to the period of a OFDM data symbol without the CP, to ensure that the carriers are orthogonal relative to each other.

Using sample-rates that are integer multiples of the OFDM system sample-rate, will also be beneficial, however it will increase the system cost and complexity.

3.2.2 Symbol synchronisation

This section discusses the effects of a receiver being asynchronous with the communication signal, therefore resulting in inter symbol interference (ISI). The PSD for an OFDM carrier is theoretically [61]:

$$S_{cc}(f) = A^2 T_{sym} \mathsf{sinc}\left(f T_{sym}\right), \tag{3.10}$$

where T_{sym} is the symbol period, A is the average symbol amplitude and f is the normalised frequency. Note that this function has zero values for integer multiples of $f \times T_{sym}$. This shows that the carrier spacing should be the reciprocal of the symbol period, as discussed previously in section 3.2.1.

3.2.3 Phase discontinuity

A complex-sinusoid is bounded over a period of T_{sym}, and undergoes a random phase change of ϕ_0 at time t_0:

$$x(t) = A \times \Pi\left(\frac{t - \frac{t_0}{2}}{t_0}\right) \times \mathrm{e}^{2\pi \mathrm{j} f_c t} + A \times \Pi\left(\frac{t - \frac{T_{sym}+t_0}{2}}{T_{sym} - t_0}\right) \times \mathrm{e}^{2\pi \mathrm{j} f_c t + j\phi_0}. \tag{3.11}$$

The PSD for this case (if it is assumed that the random phase change ϕ_0 follows a uniform distribution in $[0, 2\pi]$ and the time-delay t_0 follows a uniform distribution in $[0, T_{sym}]$) is proven to be:

$$S_{(t,\phi)}(f) = \frac{A^2}{\pi^2 v^2 T_{sym}} \left[1 - \mathsf{sinc}\left(2 v T_{sym}\right)\right]_{v=f-f_c}. \tag{3.12}$$

The full derivation of (3.12) is shown in Appendix B.

Figure 3.1 shows the perfect OFDM PSD of (3.10) compared to the PSD which is asynchronous with the system as it samples over the phase discontinuity that occurs between two symbols (B.19) (i.e. 180° phase discontinuity).

© University of Pretoria

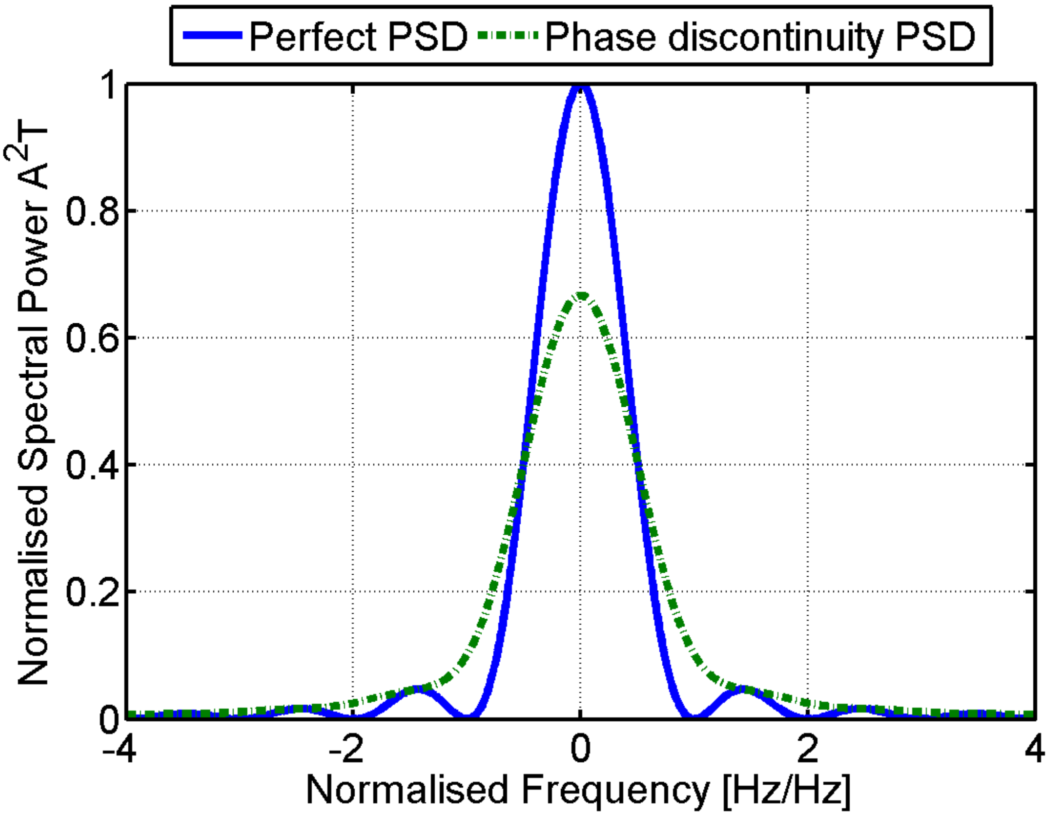

Figure 3.1: PSD of a non synchronous single OFDM carrier

It illustrates that the function is non-zero for all values, hence ICI is inevitable. This further proves that if symbol synchronisation is not met, then the OFDM system loses orthogonality.

Figure 3.2 shows the PSD on a decibel scale. In this figure it shows that the PSD with a phase discontinuity has no zeros, and seems to form a mask that is larger than the ideal value for $|f| > 0.5$. Effectively, by sampling asynchronously, the spectral density is spread over a larger bandwidth.

The PSD is undefined at $f = f_c$, however in Appendix B it is proven to be:

$$\lim_{f \to fc} S_{(t,\phi)}(f) = \frac{2}{3} A^2 T_{sym}. \tag{3.13}$$

This shows that the peak has less spectral power than in the orthogonal case. In the previous section it was shown that it is required that the sample-length of the data should be the same

© University of Pretoria

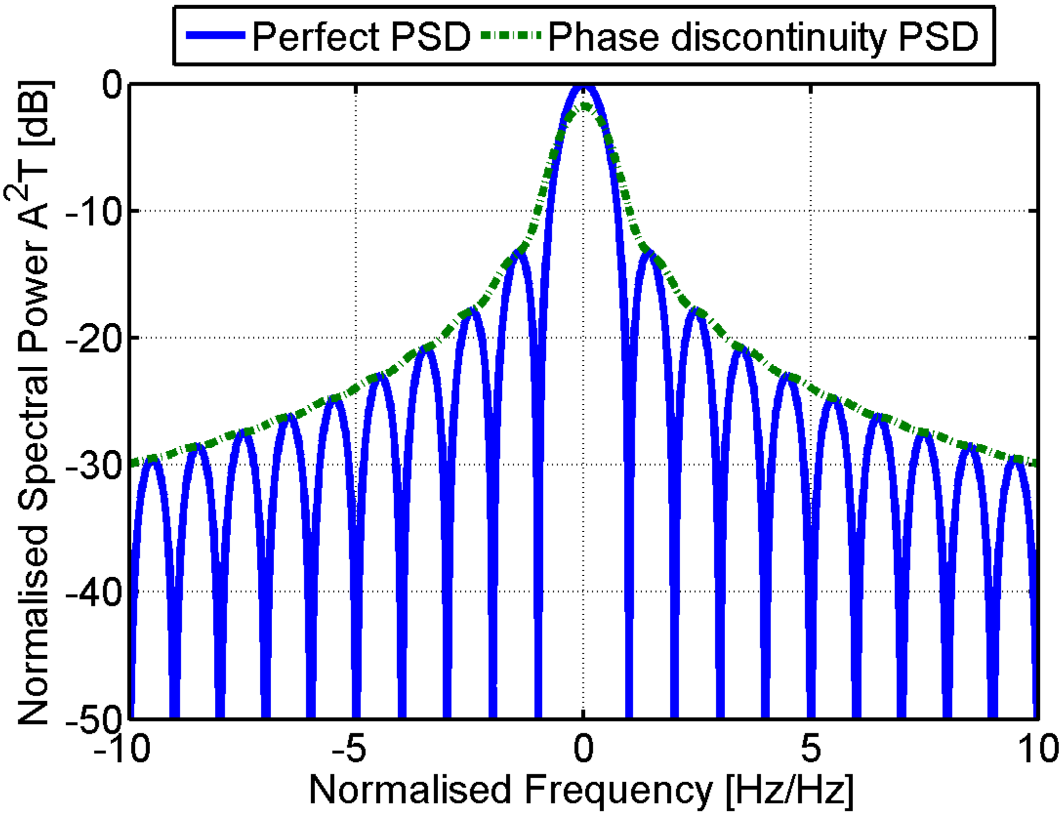

Figure 3.2: PSD of a non synchronous single OFDM carrier on a decibel scale, normalised to to the frequency resolution of the DFT.

as the OFDM signal, however it is shown that the measured data should also be synchronised to ensure carrier orthogonality.

The benefit of the CP is that absolute synchronisation is not required. As long as the block of samples do not overlap between symbols, orthogonality is kept. A slight sample offset will only cause a linear phase offset on the modulated OFDM carriers, which can be removed through the use of an equaliser. Thus the block of data to be sampled for an OFDM symbol can have a maximum tolerance of half the CP length. In the case of multipath, this tolerance is reduced.

The use of a Nyquist filter (a RRC Nyquist LPF is used in LTE) will smooth the phase transition, hence the interference is reduced. However, a Nyquist filter will not be able to completely correct the lack of orthogonality in this case.

© University of Pretoria

3.2.4 Complex amplitude discontinuity

In the previous case only a phase offset is observed. LTE uses QAM, hence the presence of an amplitude discontinuity can also be observed. The signal constellation and properties for QAM are analysed in Appendix C. A signal with a phase and amplitude discontinuity is given as:

$$x_a(t) = A_1 \times \Pi\left(\frac{t-\frac{t_0}{2}}{t_0}\right) \times \mathrm{e}^{2\pi \mathrm{j} f_c t} + A_2 \times \Pi\left(\frac{t-\frac{T_{sym}+t_0}{2}}{T_{sym}-t_0}\right) \times \mathrm{e}^{2\pi \mathrm{j} f_c t}. \tag{3.14}$$

The PSD for this case (if it is assumed the time-delay t_0 follows a uniform distribution in $[0, T_{sym}]$ and a QAM signal constellation is used) is proven to be (Appendix B):

$$S_{(t,\phi),a}(f) = \frac{A_{norm}^2}{\pi^2 v^2 T_{sym}} \left[1 - \mathsf{sinc}\left(2vT_{sym}\right)\right]_{v=f-f_c}, \tag{3.15}$$

where A_{norm} is the normalised amplitude to the mean of an OFDM modulation scheme (see Appendix C).

This illustrates that a QAM based modulation with OFDM has a similar result to the phase discontinuity case. This is largely contributed to the symmetrical properties of QAM. This further proves that loss of orthogonality is present if symbol-synchronisation is not achieved.

3.3 SYSTEM GEOMETRY

This section investigates the transmitter receiver configuration for a NNC system. The previous section explained the problems associated with not having symbol synchronisation within OFDM, and this section will illustrate why it is not achievable by a NNC system.

Figure 3.3 shows a scenario where a NNC receiver Rx is monitoring a cellular system operating around a base-station (eNodeB) with three connected cellular handsets (A,B and C). This geometry is chosen to demonstrate the extremes observed in a NNC-DF system.

Handset A and C are both located on the cell-edge of the system at opposite sides of the eNodeB, hence they are transmitting at the maximum power P_{max} specified for LTE of 0.2 W (23 dBm). Handset B is located very near to the eNodeB, and is transmitting at the

© University of Pretoria

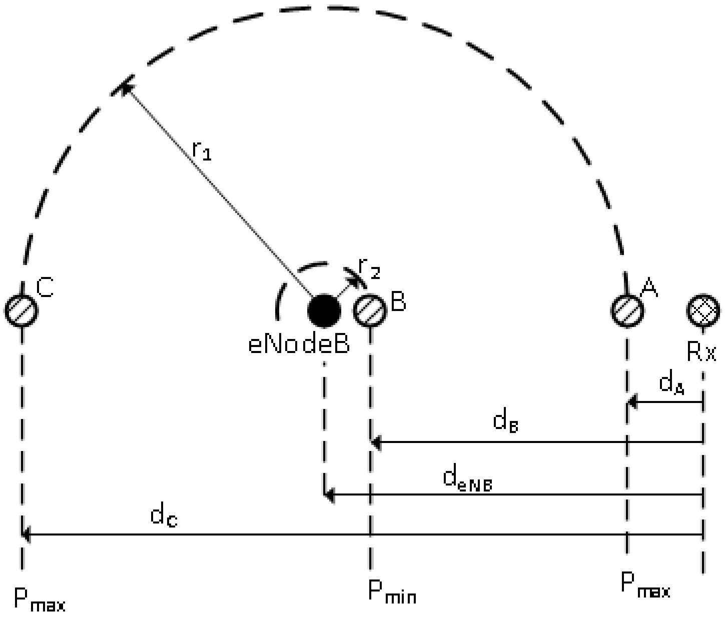

Figure 3.3: Cellular system and receiver geometry.

minimum power P_{min} for the cell of 20 μW (-17 dBm) to ensure equal received power at the eNodeB.

The receiver is located outside of the cell-edge. The cell-edge radius r_1 is selected as 5 km, as it is a minimum coverage E-UTRA requirement for LTE. The radius from the eNodeB to Handset B is selected as 50 m. The distance from the receiver system Rx to Handset A (d_A) is selected at 50 m.

The propagation time from a transmitter to a receiver is a function of the separation distance d_s and the propagation velocity (in the case of an EM-wave, it is the speed of light c) (3.16).

$$t_{del} = \frac{d_s}{v_p} = \frac{d_s}{c} \tag{3.16}$$

The ideal path-loss L_p can be described by the Friis free-space path-loss equation (3.17) [18].

$$L_p = \frac{P_r}{P_t} = \frac{G_t G_r \lambda^2}{16\pi^2 d^2} \tag{3.17}$$

© University of Pretoria

The path-loss is the ratio between the received power P_r of a receiving system and the transmitted power P_t from an emitter, and is a function of the transmitting antenna gain G_t, the receiving antenna gain G_r, the wave-length of the signal λ, and the distance between the emitter and the receiver d. Note that the Friis equation does not include noise, fading effects, terrain, interference and atmospheric conditions. Therefore actual path-loss is greater in a real system.

Unity gain for both antennas and an operational frequency of 900-MHz is assumed in this scenario. The absolute time delays, relative time-delays, the power received at the eNodeB, and the power received at the receiver system is shown in Table 3.1.

Table 3.1: Scenario variables

Parameter	**Unit**	**Handset A**	**Handset B**	**Handset C**
Distance from the eNodeB	m	5 000	50	5 000
Distance from Rx	m	50	5 050	10 050
Absolute time-delay to eNodeB	μs	16.67	0.167	16.67
Absolute time-delay to Rx	μs	0.167	16.83	33.5
Time-delay to Rx relative to Handset A	μs	0	16.67	33.33
Relative Time-delay from Handset A to Rx with timing advance	μs	0	33	33.33
Transmitted power	dBm	23	-17	23
Path-loss to eNodeB	dB	105.51	65.51	105.51
Received power at the eNodeB	dBm	-82.51	-82.51	-82.51
Path-loss to Rx	dB	65.51	105.6	111.57
Received power at the Rx	dBm	-42.51	-122.3	-88.57
Received power at the Rx relative to the received power of Handset A	dB	0	-79.79	-46.06

In this scenario the power control and timing advance by the eNodeB to the handsets are assumed ideal. The power control is implemented to ensure that equal power will be observed by the eNodeB for each handset. The timing advance is used to ensure that the received signals have minimal timing offsets as observed by the eNodeB. This reduces ICI as all symbols are semi-aligned and can therefore be semi-synchronously demodulated.

© University of Pretoria

In this scenario, the greatest timing difference between the received signals is 33.3 μs. This timing difference is equal to twice the maximum CP time ($512 \times T_s = 16.6$ μs for the extended CP) of LTE. Therefore inter-symbol interference is guaranteed. This proves why the signal processing challenges of section 3.2 are realistic for practical systems. In the case of very small cell-sizes these problems for a NNC system are reduced.

To compare the received signal powers for the NNC receiver, a maximum difference of 79.79 dB is calculated in this scenario. This means that a dynamic range greater than 80 dB is required for the receiver system to be able to observe both signals simultaneously. This point illustrates the challenge regarding power differences of cellular handsets. The lowest received power in this scenario is -122.3 dB, for many systems this power level is below the noise level, making it very difficult to detect.

In this scenario the 900 MHz range is selected as it is a popular band for cellular communications (E-UTRA band 5, 6, 8, 18, 19, 20, 26 and 27). However the 900 MHz band is typically used for Global System for Mobile Communications (GSM) and the 1800 MHz band (E-UTRA band 1, 2, 3, 4, 9, 10, 25, 33, 35, 36, 37 and 39) is used for LTE. There are LTE systems that do occupy the 900 MHz band. Note that the 1800 MHz band will have greater attenuation due to the Friis transmission equation (3.17). The 900 MHz band was selected for this scenario as it should have better performance, and should therefore emphasise that even with better band selection the power loss associated with monitoring a cellular system is detrimental to NNC monitoring.

It should be noted that for improved system performance the receiver should be located as close as possible to the eNodeB to benefit from power control and timing advance. This ideal scenario is unfortunately not always possible.

3.4 CRAMÉR-RAO BOUND FOR VARIOUS ARRAYS

This section evaluates the CRB for different array configurations, assuming only a single signal is observed. The full derivation of the CRBs are shown in Appendix D.

© University of Pretoria

3.4.1 CRB: ULA

The approximate CRB for a ULA with half-wavelength antenna spacing is derived as:

$$\mathrm{CRB}_{ULA} \approx \frac{6}{K \times \mathrm{SNR} \times \pi^2 \cos^2(\theta) N_a (N_a^2 - 1)}. \tag{3.18}$$

It should be noted that this CRB is a function of the incident angle θ, and is lowest when the source is located at the broadside of the antenna array, and highest at the end-fire of the array. This shows that the DOA estimation of a ULA is dependant on the location that the signal source has relative to the array.

3.4.2 CRB: UCA

The approximate CRB for a UCA with half-wavelength radius is derived as:

$$\mathrm{CRB}_{UCA} \approx \frac{1}{K \times \mathrm{SNR} \times \pi^2 \times N_a}. \tag{3.19}$$

This CRB is only a function of the SNR and the number of antenna elements N_a.

3.4.3 CRB: UCA-CE

A uniform circular array with a center element (UCA-CE) is an array of N_a elements, composed of a UCA of $N_a - 1$ elements and a single element at the origin. The mathematical derivations of this array is therefore similar to that of a UCA with one less element:

$$\mathrm{CRB}_{UCA-CE} \approx \frac{1}{K \times \mathrm{SNR} \times \pi^2 \times (N_a - 1)}. \tag{3.20}$$

The CRB shows that a UCA-CE has the bound of a UCA with one less element. UCA-CE configuration are however used for small antenna configurations, as it removes the antenna structural ambiguity for small arrays.

3.5 CHANNELISER ARCHITECTURE

A channeliser is a software filter-bank that is used to separate signals from different frequencies. There are many architectures for channelisers, however in this section a DFT based channeliser is discussed.

© University of Pretoria

A channeliser architecture is defined by a running DFT of size K. The discrete input data $x[n]$ is passed through a DFT to form the output data $y_m[n]$ for the m-th frequency tap (3.21).

$$y_m[n] = \frac{1}{K}\sum_{k=0}^{K-1} x[n+m]\mathrm{e}^{-2\pi\,\mathrm{j}m\frac{k}{K}} \tag{3.21}$$

For a block of input data of size K, the DFT generates K output points. As the block of data used for the DFT is shifted on by one sample after each calculation, only one new data sample of x is introduced and K new outputs are generated. It can therefore be said that once the original block of data has been replaced with new data samples, then the channelisers has an increase of factor K samples from input to output.

Theoretically the output is a time-shifted Fourier transform of the data. If a sinusoidal input with a frequency of f_c, a sample-rate of T_s, and a data block-length of T_d is used, then the output can be described:

$$y_f[n] = \mathfrak{F}\left\{\Pi\left(\frac{t}{T_d}\right)\times \mathrm{e}^{2\pi\,\mathrm{j}f_c(t+nT_s)}\right\} = T_d\mathsf{sinc}\left(T_d f\right) * \mathrm{e}^{2\pi\,\mathrm{j}nT_s f}\delta\left(f-f_c\right). \tag{3.22}$$

Through simplification, it can be shown that the resultant expression is a function of the rectangular window (refer to section 2.5.2.4) and a shifted sinusoid:

$$y_f[n] = T_d\mathsf{sinc}\left(T_d f\right) * \mathrm{e}^{2\pi\,\mathrm{j}nT_s f_c}\delta\left(f-f_c\right) = T_d\mathsf{sinc}\left(T_d(f-f_c)\right)\mathrm{e}^{2\pi\,\mathrm{j}nT_s f_c}, \tag{3.23}$$

therefore the result is a scaled version of the original signal:

$$y_{f_c}[n] = T_d\mathrm{e}^{2\pi\,\mathrm{j}nT_s f_c}. \tag{3.24}$$

This shows that the original signal is retrievable at this frequency. The operation therefore uses a DFT, but the output is a time domain signal. The interference to other channels is a function of the window used for the DFT. Therefore by selecting the appropriate window the interference can be decreased more efficiently.

A channeliser efficiently separates a signal into various frequency taps. Once the taps are generated, further processing can be done, for example additional filtering can be implemented to increase the separation of signals. Due to the structure of a channeliser, it is an

© University of Pretoria

efficient algorithm for constant-time processing platforms, e.g. a field-programmable gate array (FPGA).

3.6 PRACTICAL CONSIDERATIONS

The previous chapter gave an overview of the literature. The literature often assumes the ideal case of a system, especially as most sections of the literature only considers itself in an isolated scenario. This chapter has analysed and discussed many effects that are detrimental to DOA estimation of OFDM based cellular communication signals. This section aims to provide practical considerations required in design and implementation of a NNC DF system.

3.6.1 Location

As underlined in section 3.3, the geometry of a system can greatly influence the performance. As a cellular system uses multiple base-stations to provide coverage to a area, it is difficult to cover the same area without the use of multiple NNC receivers. The use of multiple receivers will greatly increase system cost.

The location of a NNC receiver should be as close as possible to a base station to benefit from the power and timing control of the handsets. This is however not always possible as the base-stations are often located on restricted property, hard to reach places (roof tops or mountains), or they can be hidden (hence some locating of the base-station is also required).

Frequency reuse is implemented in cellular systems to increase system capacity. Frequency reuse can cause interference for a NNC receiver if the receiver is poorly located between two base-stations that make use of the same transmission frequency. It should be noted that this probability can be very low, as the frequency reuse-factor is implemented to limit interference in a system.

In conclusion, the location selection of a NNC deployment will have a profound influence on the performance of the system. Adequate planning and scouting before deployment will therefore be crucial for the system to succeed.

© University of Pretoria

3.6.2 Antenna array

The selection of the antenna array determines the theoretical best performance of a system, as discussed in sections 2.2.2 and 3.4. The trade-off between arrays with good performance per number of antenna elements (e.g. ULA), and arrays which have reduced ambiguity and hence larger reliable angular-coverage (e.g. UCA-CE) should be evaluated.

In this dissertation only NB antennas with half wave-length antenna spacings are discussed in order to demonstrate the concept. In practical systems wide-band (WB) signal estimation is required, and hence WB antenna configurations are required. This is an important point to realise for a deployable system, however it is beyond the scope of this dissertation.

In literature arbitrary large sensor arrays are used, as it provides superior performance, and the assumption of (2.17) is valid. This is not necessarily practical for a deployable system. A receiver-channel is required per antenna element, hence the system cost increases as the number of antenna elements increases.

The greatest design issue with a large number of receiver channels is to ensure that the channels are time- , phase- and data-reference synchronised. If the channels are not synchronised, then coherent comparison is not possible and therefore DOA estimation using interferometry is void. This is the greatest risk associated with DOA estimation of practical systems. The phase stability between receivers directly influences DOA estimation accuracy. Synchronising receivers are achievable on off-the-shelf equipment that have multiple synchronised channels, however most hardware have limited number of channels and synchronisation between hardware sets proof difficult. In most cases when a large number of channels is required for a system, the hardware is typically not commercially available; therefore custom hardware should be developed, which is expensive due to development costs.

The application often limits the antenna configuration. If the system is required to be portable, then the absolute size of the system should be sufficiently small. For man-portable systems additional ergonomic analysis is required. For vehicular systems additional system specifications such as mounting of the system to the vehicle and to ensure vehicular safety and regulations are required. The operational frequency and the number of antenna elements directly influence the size of the system.

© University of Pretoria

The selection of the antenna is also important. If the array is to be mounted on a planar surface (e.g. roof of a vehicle), then the use of dipole antennas is restricted. In such cases monopole-antennas are often used. If the antenna configuration is to be mounted on a planar surface on the side of a vehicle, then patch-antennas can provide a good solution. In most cases omnidirectional antennas are preferred; however if the FOV is not required to be the full range, then directional antennas can have an antenna gain benefit. This shows that the application will directly influence the selection of the number and configuration of the antenna elements.

3.6.3 Bandwidth and POI

There are multiple E-UTRA bands assigned for communication. Therefore multiple bands should be monitored. These bands often have large bandwidths (maximum bandwidth for FDD is 80 MHz in E-UTRA band 22, and for TDD 200 MHz in E-UTRA bands 40, 42 and 43). This illustrates that a large operational bandwidth is required for a NNC system if the full communication of LTE in an area is to be monitored.

Systems that have large sample bandwidths are typically costly and bulky. For mobile systems, this is often not realisable. As soon as the operational bandwidth of a NNC receiver is reduced, the POI of that system is also severely reduced. There are methods to more efficiently reduce the operational bandwidth, through monitoring of the base-stations to determine which bands are currently utilised and to allocate the NNC receiver bandwidth accordingly.

3.6.4 Calibration

All equipment should be calibrated to ensure reliable results. In the case of a sensor array, phase calibration is required for channel synchronisation. Often the phase offsets of the sensor array are altered if the environment is changed (i.e. the array is moved), hence portable calibration should be built into the system.

The receiver hardware may have temperature-sensitive components, hence a change in ambient or operational temperature may also influence the synchronisation of the channels. Calibration-in-the-loop methods are strongly advised to reduce all environmental effects on

© University of Pretoria

the measurements.

3.6.5 Processing

The tasks that the NNC system should be capable to achieve directly influences the required processing of the system. If processing intense tasks are required, then suitable hardware should be selected. Certain tasks are more efficient on certain hardware architectures, hence processing hardware should be considered carefully. Fixed-length processing tasks are often best suited for set hardware based architectures (e.g. dedicated hardware of FPGAs). Variable length processing that benefits greatly from parallel processing is suited for graphics processing unit (GPU) base architectures, and variable length processing that does not require parallel processing is best suited for digital signal processors (DSPs) or central processing units (CPUs).

Analogue processing should not be disregarded as there are benefits, however for a multiple-channel system calibration is proven difficult. Analogue processing is usually used for filtering and for automatic gain control (AGC).

3.6.6 Receiver system and cost

Due to the massive power differences of signals on receive (illustrated in section 3.3), a receiver with a wide dynamic range is required. A wide dynamic range implies that a digital receiver with an ADC with high resolution is required (e.g. in the scenario of section 3.3 a minimum word-length of 13 bits is required). With an ADC the trade-off between bandwidth, resolution and cost should be considered.

In the previous section the trade-offs of the receiver system has already been discussed. In general the better the performance of a system, the more expensive the system will be. If a system should be custom made (i.e. does not use off-the-shelf equipment), then development costs heavily inflate system costs. A deployable system will be more costly than a laboratory set-up, as the system should be packed and ruggedised. Electrical power for the system is often an issue for deployable system and should be taken into consideration.

© University of Pretoria

© University of Pretoria

CHAPTER 4

SIMULATIONS

4.1 CHAPTER OVERVIEW

This chapter presents the simulation results from various DF receivers, sensor array structures, processing methods and algorithms.

4.2 SIMULATION SET-UP

The input signal is selected as an OFDM communication signal similar to the LTE specification. An OFDM symbol contains a number of carriers spaced equally in frequency, hence it is generated optimally by modulating the data on each carrier and using an inverse-FFT to transpose the symbol into the time domain [61]. In the LTE specification, 12 carriers are grouped together to form a RB [20, 50]. RBs are assigned to each user to achieve efficient frequency resource allocation. A CP is added in the time domain to each OFDM symbol for symbol synchronisation.

It is assumed that two signals from different AOAs are present. The first signal contains two RBs, they are denoted as RB 1 and RB 2 respectively. The second signal is directly adjacent in the frequency domain to the first signal and contains a single RB, this is denoted as RB 3. The second signal is received with 10 dB more power than the first signal. This is done to test the interference between signals from different sources at different power levels. The two sources are not time aligned, hence the OFDM symbols of the two sources are not synchronised at the receiver. This is done as it is assumed the DF system is NNC.

A 256-point IFFT is used for the OFDM symbol modulation. Only three RBs are modulated (36 carriers), hence 14% of the spectrum is utilised (percentage of carriers occupied). The SNR is calculated using the combined power of both signals. Figure 4.1 shows a diagram of the source signals.

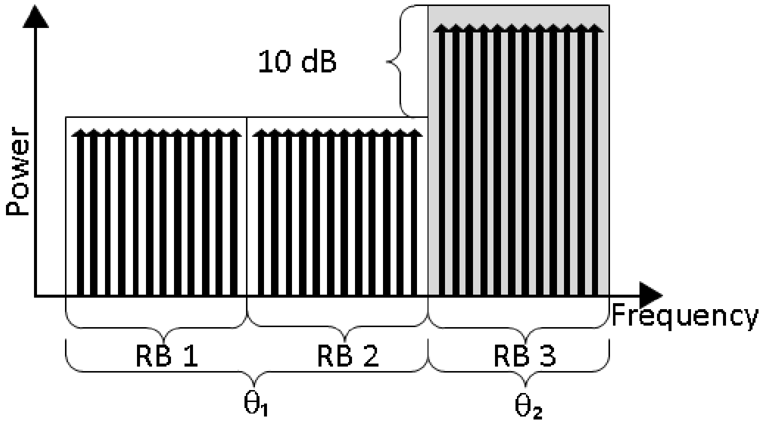

Figure 4.1: Diagram of the source signal properties.

Four different types of receivers are used for the pre-DOA integration. All receivers use $2N$ data samples, where N is the number of samples per OFDM symbol (without the CP). Hence multiple symbols are observed, and in the process the OFDM system loses orthogonality (see section 3.2). A block diagram of the four receiver types are shown in Figure 4.2.

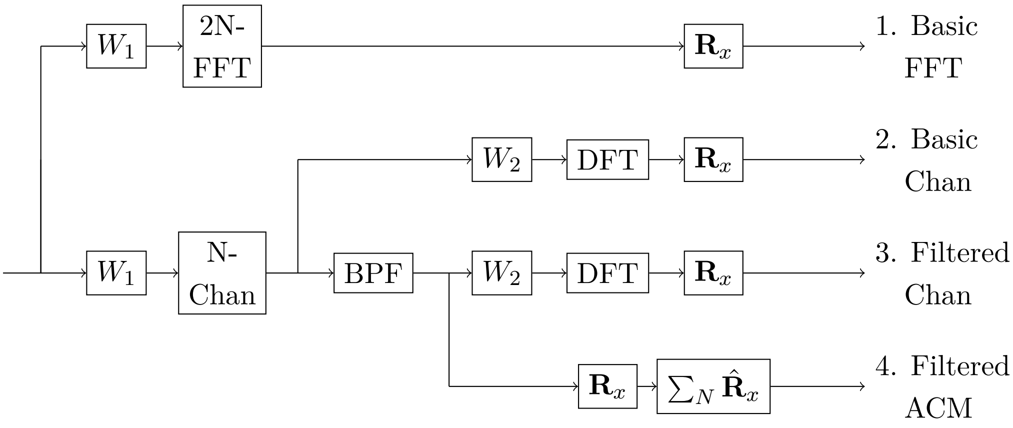

Figure 4.2: Block diagram of the pre-DOA and DOA improvement integration.

The four receivers are:

1. A basic FFT method is used, with a FFT size $2N$ and a window W_1, hence every second frequency tap will coincide with a carrier. This receiver architecture increases

© University of Pretoria

the carrier spacing by using double the number of required FFT taps. The out of band noise is also further reduced as the noise is spread over twice the number of frequency taps. This is also the least processing intensive receiver architecture.

2. A channeliser that uses an N-point FFT with a window W_1 to separate the channels. The N-FFT serves as a time domain filter bank. After $2N-1$ data points have moved through the channeliser, an N-point DFT with a window W_2 is used to integrate each channel. This receiver architecture increases carrier isolation through channelising the data. This is more processing intensive than the first receiver.
3. Similar to the channeliser in case 2, however an additional BPF is implemented on every channel between the channeliser and the DFT to further reduce interference from neighbouring channels. The added filter increases carrier isolation, hence this receiver has the greatest out-of-band noise and interference reduction.
4. Similar to the BPF channeliser of case 3, however the ACM per data sample is calculated and the N-number of ACMs are then added. Hence it focuses on DOA improvement integration. This receiver uses both carrier isolation and ACM-improvement integration methods. This means that this receiver should have the best approximation of the ACM. This receiver type is also the most processing intensive due to the generation of N ACM calculations.

To exploit the FDMA structure of OFDM, the carrier-structure is used for frequency integration. A block diagram of the three FDMA integration methods is shown in Figure 4.3.

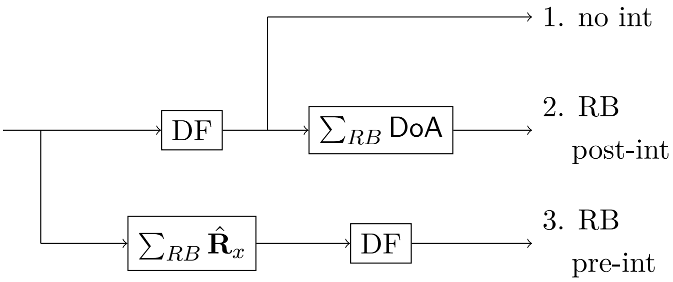

Figure 4.3: Block diagram of DOA improvement and post-DOA integration.

Three methods are used for every receiver type:

1. Only DF is performed, hence no inter-channel integration is used. This is to demonstrate the performance without exploiting the multiplexing scheme of the signal.

© University of Pretoria

2. The DOA estimates per RB are summed (12 carriers), for post-DOA integration. This method shows a basic post DOA estimation method that can improve the overall estimation.
3. The ACM of each carrier of a RB is used for DOA improvement. This method uses DOA improvement integration over the multiplexing scheme, thus showing that even though the receiver architecture does not use ACM integration, it can be used in the processing chain at a later stage.

By combining the receivers and the FDMA integration methods, a total of 12 systems are simulated. These DOA estimation systems are aimed at different levels of pre-DOA, DOA improvement and post-DOA integration methods.

The windows used for W_1 and W_2 in the simulation are:

1. Rectangular,
2. Triangular,
3. Hann,
4. Hamming,
5. Gaussian with $BT = 3$,
6. Blackman-Harris.

For these simulations it is assumed that if both W_1 and W_2 are used, they are selected to be the same window. The receiver sample-rate is 3.84 MHz and assumes a complex baseband signal. The intermediate frequency (IF) is selected as 1 GHz. The IF determines the relation between the Doppler frequency shift and velocity, as well as determines the location of the sensors within the sensor array.

The array structures use 4,5, and 6 elements. These number of elements are selected as it requires relatively few channels which are practically achievable due to cost, size and processing. The sensor configurations for the arrays are selected as basic uniform arrays:

1. ULA with half wave-length inter-element spacing,
2. UCA with half wave-length radius,
3. UCA-CE with half wave-length radius.

© University of Pretoria

In the simulation multiple array structures are selected to be tested, however in the case where other parameters are to be tested (i.e. receiver, windowing, and DF algorithms), a 5-element UCA is selected. This array structure is selected as it is the UCA structure with the fewest number of elements and a half-wavelength radius that does not have an angular ambiguity. A UCA is selected as it is a standard structure that has 360° azimuth coverage.

Only PCA based AOA estimation algorithms are used in the simulation, in particular the MuSiC algorithm. These algorithms are selected as they are applicable to the given array configurations. The following algorithms (with descriptions) are used in the simulation:

1. **MuSiC**: This is the spectral MuSiC algorithm (see section 2.4.1). As it is computationally expensive to search through all values, a search tree is used. The benefit is that for the same resolution considerably less data-points need to be evaluated, however an early error in the search algorithm can cause the whole search to be faulty. Four iterations of the tree-search is done. The search step-sizes are 10°, 1°, 0.1° and 0.01° respectively. The search ranges are: full range ($-90°$ to $90°$ for ULA, and $-180°$ to $180°$ for UCA and UCA-CE), $\pm 10°$, $\pm 1°$ and $\pm 0.1°$ for the four stages respectively. This shows that in the worst case 100 angles are tested through the tree-search algorithm. If all angular values are to be tested at the same angular resolution of 0.01° then 36 000 values should be tested, therefore the tree algorithm reduces the number of tests by a factor of 360. The algorithm can have a minimum RMSE of 0.005°, as it is limited by the angular search resolution.
2. **Root-MuSiC**: This algorithm uses the manifold Root-MuSiC(see section 2.4.2.2). The mathematical translation of equation (2.40) is used for the UCA. Similarly, for a UCA-CE, the centre element is omitted and is regarded as a UCA for this algorithm; note that this reduces the performance of a UCA-CE greatly. A mathematical translation for a UCA-CE is not currently available, and such a derivation is beyond the scope of this dissertation. This algorithm requires less processing than the spectral MuSiC algorithm, however it has reduced performance due to approximation errors.
3. **Root-Search-MuSiC**: This algorithm uses the Root-MuSiC algorithm to estimate an initial value. This value is then used as a search location and improved through the use of the spectral MuSiC algorithm. Once again a search tree of two stages is used to determine the optimal point. An angular resolution of 0.8° and 0.16° are used for the

© University of Pretoria

tree searches respectively, over a search range of ±4° and ±0.64°. This algorithm should provide improved results in comparison to the Root-MuSiC, at the cost of additional processing.

4. **FD-Root-MuSiC**: This algorithm is described in section 2.4.2.3. The manifold is selected as $M = 16$, hence a total of $2M - 1 = 31$ angular values are tested in this algorithm.
5. **FD-Linesearch-MuSiC**: This algorithm is described in section 2.4.2.4. The manifold is selected as $M = 16$, hence a total of $2M - 1 = 31$ angular values are tested in this algorithm. The IDFT parameter is selected as $J = 256$, hence a IDFT of size $2J - 1 = 511$ is used. This shows that the minimum achievable RMSE for this algorithm is 0.176°.
6. **WLS-FD-Root-MuSiC**: This algorithm is described in section 2.4.2.5 with the principals of section 2.4.2.3. The manifold is selected as $M = 16$, and the test parameter is selected as $Q = 2M = 32$, hence a total of $2Q - 1 = 63$ angular values are tested in this algorithm.
7. **WLS-FD-Linesearch-MuSiC**: This algorithm is described in section 2.4.2.5 with the principals of section 2.4.2.4. The manifold is selected as $M = 16$, and the test parameter is selected as $Q = 2M = 32$, hence a total of $2Q - 1 = 63$ angular values are tested in this algorithm. The IDFT parameter is selected as $J = 256$, hence a IDFT of size $2J - 1 = 511$ is used. This shows that the minimum achievable RMSE for this algorithm is 0.176°.

The FD-Root-MuSiC is used in the simulations when other parameters are evaluated as it is applicable to any array configuration (no array-translation is required), less processing is required in comparison to the spectral-MuSiC algorithm, it is scalable for better resolutions, and renders a good approximation for a configuration with small number of antenna elements.

The simulations are Monte-Carlo based and each AOA-estimation receiver and method is run 100 times over 180 DOA sets. The AOA of RBs 1 and 2 are tested in 2° steps over the full azimuth, and the AOA of RB 3 is randomised for every simulation. This is done to ensure that the full range of AOAs are tested. Hence a total of 18 000 Monte-Carlo runs were performed. MATLAB version 8.2.0.701 (R2013b) on a LINUX operating system is used for

© University of Pretoria

the simulations. The computer used for the simulation is a Dell PowerEdge 2950 Generation 3 with two 2.5 GHz Intel Xeon L5420 quad-core processors and 16 GB of RAM.

4.3 RESULTS

The simulation results are shown in this section. As there are multiple parameters that are tested, only a subsection of the results are presented to illustrate the influence of these parameters. The results are shown in the subsequent subsections.

The CRB on these graphs are calculated for the case of a single signal, as this is a lower bound than for the case of multiple signals. The exact bound is not derived for each signal case due to the mathematical complexity involved.

The performance for a given DOA system and scenario is shown by RMSE for a given SNR. Typically the RMSE graph has four regions:

1. **Noise dominant region**: this is the region where the noise is much greater than the signal, hence parameter estimation will yield false results. This section has a constant value for AOA estimation, as this parameter wraps for every 360°. In the case of this simulation scenario, this region is typically for SNRs smaller than -20 dB.
2. **Noise uncertainty region**: this is the region where the SNR is sufficient to yield estimation results, but the noise still causes wrong separation of the eigenvectors to represent the signal and noise-subspaces. As a result the AOA estimation uses the wrong subspace and hence it causes large errors. This region typically has monotone descending RMSE values as the SNR increases, and is the bridge between the noise dominant region and the signal dominant region.
3. **Signal dominant region**: this is the region where the correct subspaces are selected and the SNR is sufficiently large for reliable estimation. Good estimators have RMSE values that are monotone descending as the SNR increases, and should be as close to the CRB as possible.
4. **Saturation region**: this is the upper region of the signal dominant region, where algorithm-, word-length-, tolerance- and system-deficiencies cause the performance of an estimator to saturate. This region therefore has a constant value for all the given SNRs values.

© University of Pretoria

It should be noted that the noise uncertainty region and signal dominant region are often difficult to distinguish from each other, especially in cases where the saturation region starts at low SNRs values.

4.3.1 Algorithm comparison

This section considers the performance of the DF algorithm. The legend for the graphs in this section is shown in Figure 4.4.

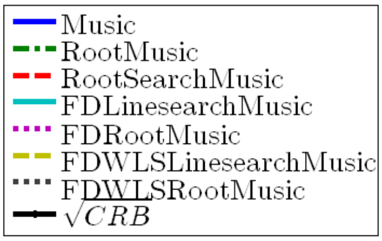

Figure 4.4: Legend for DF algorithm comparison.

Figures 4.5 to 4.13 compare the different DF algorithms. The results are generated from a simulation for a UCA of 5 elements and a BPF-Channeliser with ACM integration and a Gaussian window ($BT = 3$) for the first as well as second window.

A UCA is selected as it allows 360° coverage. A UCA array with 5 elements is the UCA array with the fewest number of elements, with no ambiguities for a half wave-length radius. The less elements that are used, the less processing is required. The BPF-Channeliser with ACM integration is used, as the receiver architecture applies maximum signal isolation, hence the best results are expected. A Gaussian window is used as it has low SLL with a relative small main lobe width increase.

Figures 4.5 to 4.7 show the performance of the DF algorithms for RB 1 under different post-integration methods.

The simulation results for the first RB show that they are far away from the general CRB. This is due to the interference caused by the signal of the third RB, which is received at higher power levels.

In the case with no post-integration (Figure 4.5) the majority of the algorithms tend to a

© University of Pretoria

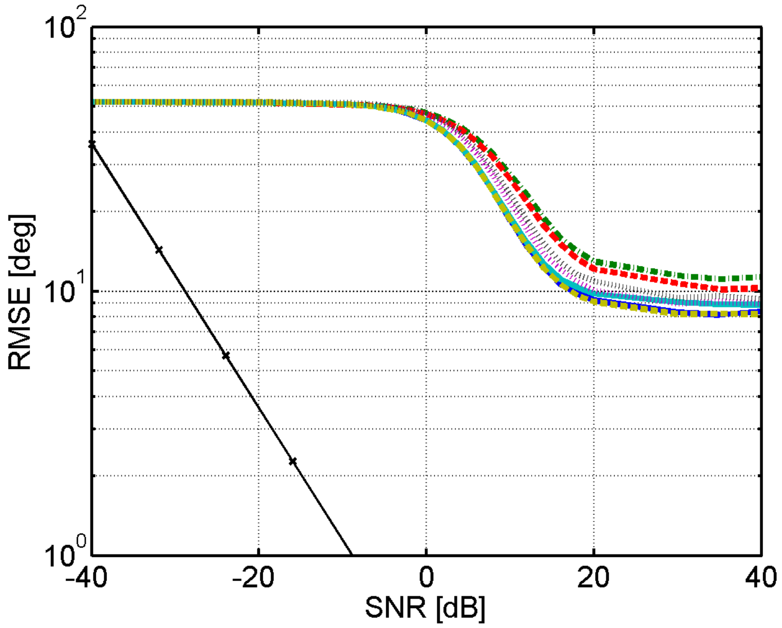

Figure 4.5: DF algorithm comparison using a UCA of 5 elements, a Gaussian window with $BT = 3$ and a BPF-Channeliser with ACM integration with no post-integration of RB 1.

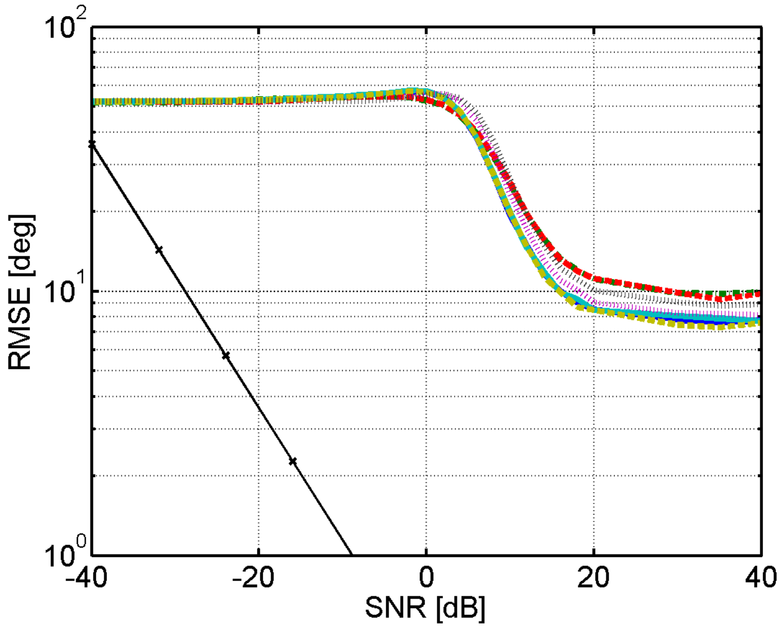

Figure 4.6: DF algorithm comparison using a UCA of 5 elements, a Gaussian window with $BT = 3$ and a BPF-Channeliser with ACM integration with post-integration over RB 1.

© University of Pretoria

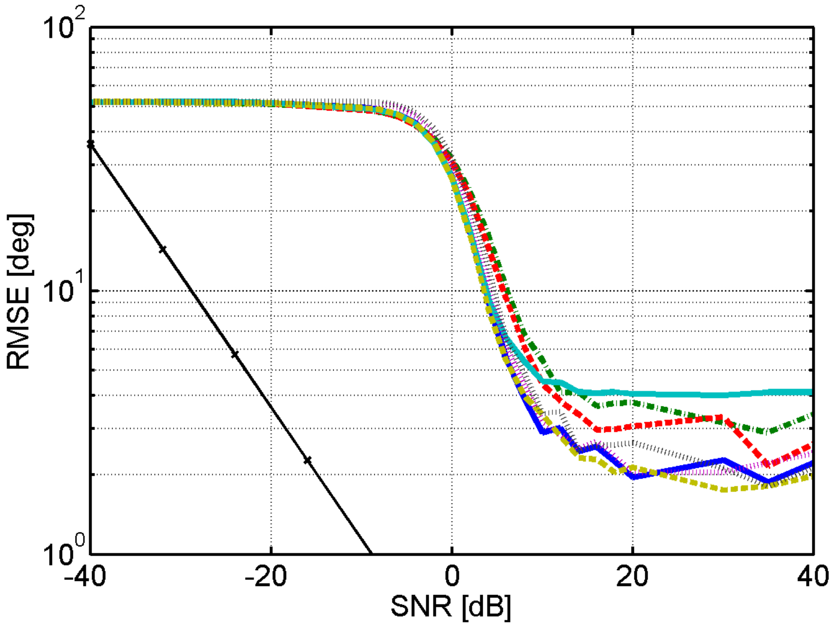

Figure 4.7: DF algorithm comparison using a UCA of 5 elements, a Gaussian window with $BT = 3$ and a BPF-Channeliser with ACM integration and with ACM integration of RB 1.

RMSE of 10° as the SNR increases. In the case of post-integration (Figure 4.6) all of the algorithms tend to RMSE values less than 10° as the SNR increases. The result that use ACM integration over the full RB (Figure 4.7), yields the best results; where the poorest performance was the FD-Linesearch-MuSiC algorithm that tends to a RMSE of 4° as the SNR increases.

In all three figures (Figures 4.5 to 4.7) the Root-MuSiC and the Root-search-MuSiC algorithms perform as two of the three poorest algorithms. The Root-Search-MuSiC outperforms the Root-MuSiC in all three cases. The (spectral) MuSiC and the WLS-FD-Linesearch algorithms consistently perform best in comparison to the other algorithms.

The noise dominant region for Figures 4.5 and 4.6 is defined for SNR$<$ 0 dB, and for Figure 4.7 it is defined for SNR< -5 dB. This shows that ACM integration reduces the transition between the noise dominant - and signal dominant region. In all three cases the noise uncertainty and signal dominant regions are not distinguishable. Post-integration increases the slope of the signal-dominant region, in comparison to using no integration.

Figures 4.8 to 4.10 show the performance of the DF algorithms for RB 2 under different

© University of Pretoria

post-integration methods.

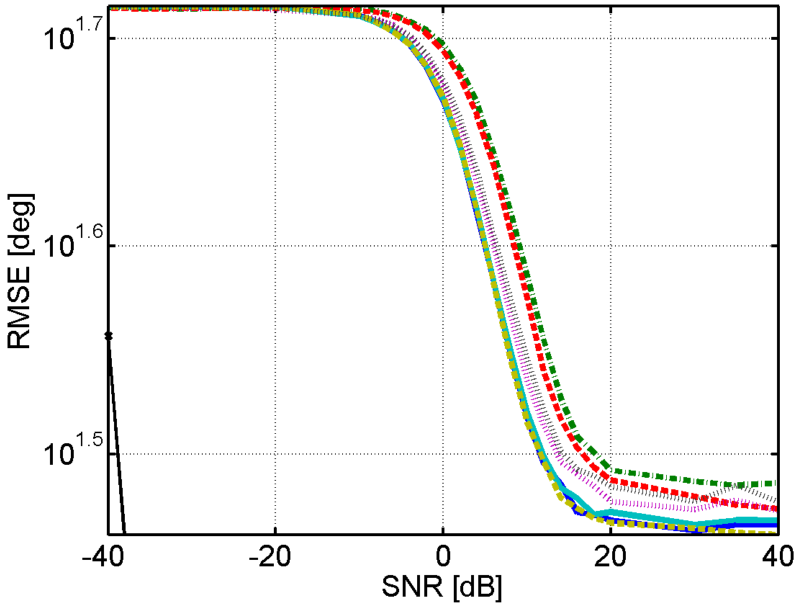

Figure 4.8: DF algorithm comparison using a UCA of 5 elements, a Gaussian window with $BT = 3$ and a BPF-Channeliser with ACM integration with no post-integration of RB 2.

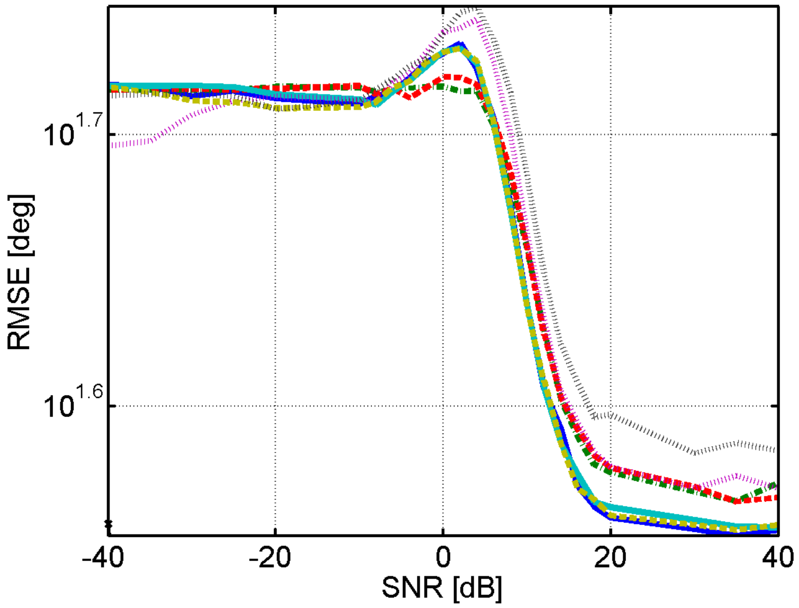

Figure 4.9: DF algorithm comparison using a UCA of 5 elements, a Gaussian window with $BT = 3$ and a BPF-Channeliser with ACM integration with post-integration over RB 2.

The simulation results for the second RB (Figures 4.8 to 4.10) have poorer results than those

© University of Pretoria

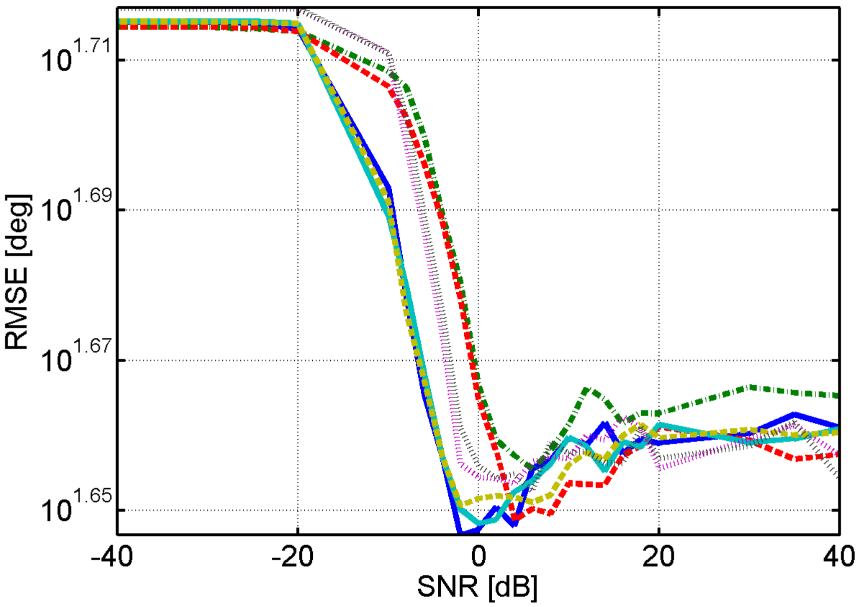

Figure 4.10: DF algorithm comparison using a UCA of 5 elements, a Gaussian window with $BT = 3$ and a BPF-Channeliser with ACM integration and with ACM integration of RB 2.

of the first RB (Figures 4.5 to 4.7). This is because the second RB is located very close to the third RB and results in significant interference. The results are biased to the AOA of the third RB and are hence more times than not associated with the wrong signal. The best achievable RMSE for the second RB is 30° (Figure 4.8).

Figures 4.11 to 4.13 show the performance of the DF algorithms for RB 3 under different post-integration methods.

Figures 4.11 to 4.13 have better performance and are near the CRB in the signal dominant region. The differences between the algorithms are larger for the third RB in comparison to the other RBs (Figures 4.5 to 4.10).

All four regions are clearly visible in Figure 4.13. Consider the data for the Root-search-MuSiC algorithm. The noise dominant region is defined for SNR values below -25 dB, the noise uncertainty region ranges from -25 dB to -10 dB, the signal dominant region ranges for values above -10 dB, and the saturation region ranges for values larger than 20 dB.

© University of Pretoria

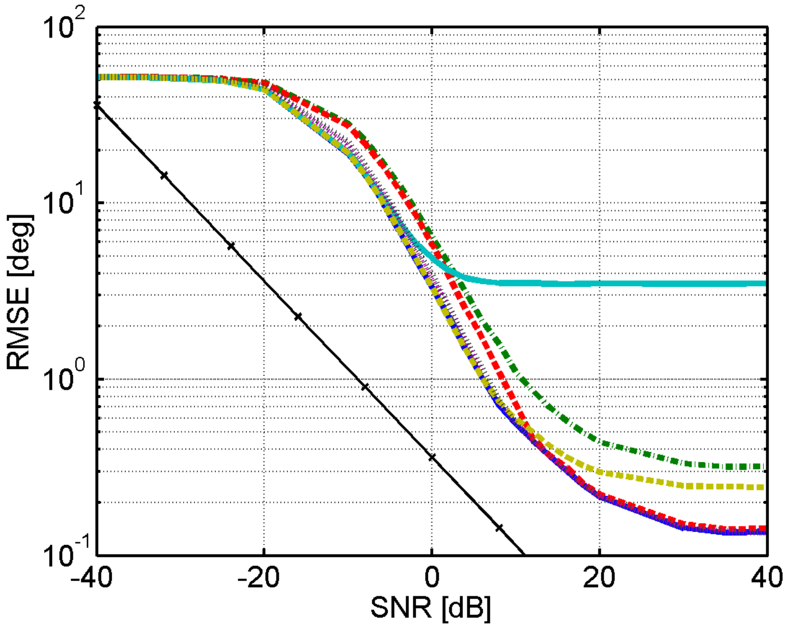

Figure 4.11: DF algorithm comparison using a UCA of 5 elements, a Gaussian window with $BT = 3$ and a BPF-Channeliser with ACM integration with no post-integration of RB 3.

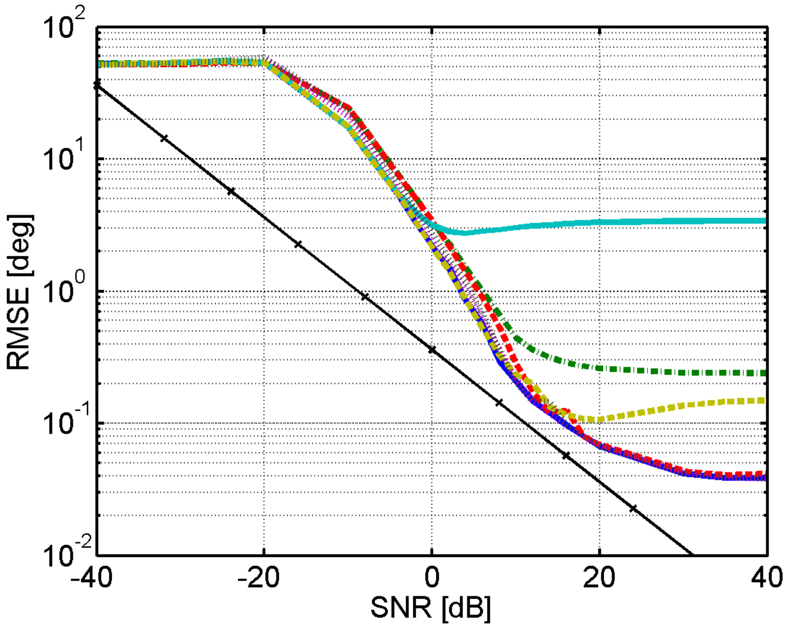

Figure 4.12: DF algorithm comparison using a UCA of 5 elements, a Gaussian window with $BT = 3$ and a BPF-Channeliser with ACM integration with post-integration over RB 3.

© University of Pretoria

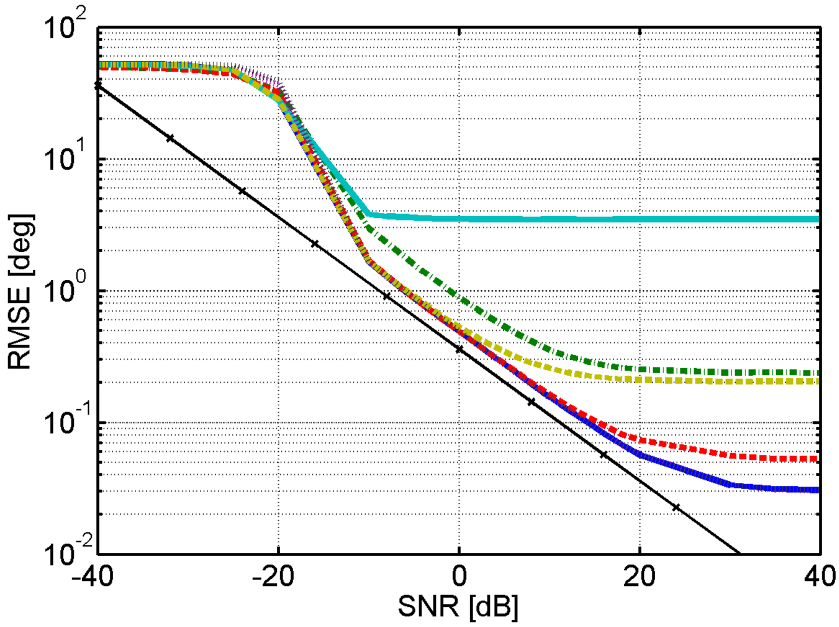

Figure 4.13: DF algorithm comparison using a UCA of 5 elements, a Gaussian window with $BT = 3$ and a BPF-Channeliser with ACM integration and with ACM integration of RB 3.

For all post-integration methods (Figures 4.11 to 4.13), the FD-Linesearch-MuSiC algorithm has the poorest performance, as the saturation region starts at the lowest SNR values and has a fairly high RMSE value of $\pm 3°$. In Figure 4.13, the FD-Linesearch-MuSiC algorithm saturation region spans the full signal dominant region, and this is clearly visible if compared to the other results on the same graph.

The ACM integration over a RB (Figure 4.11), yields the best results for all algorithms. In this figure it shows that the spectral MuSiC, FD-Root-MuSiC and WLS-FD-Root-MuSiC algorithms achieve the best as well as equal performance. The WLS-FD-Linesearch-MuSiC algorithm has a clear improvement on the FD-Linesearch-MuSiC algorithm. This shows that vastly superior performance can be achieved through the weighting function. Similarly, the Root-Search-MuSiC has a significant improvement over the Root-MuSiC algorithm, as it reduces the estimation error caused by the array approximation (note that with a ULA the improvement will not be as dramatic).

Table 4.1 shows the average processing times of all the algorithms. Note that the simulation times for the Basic-FFT is also included, as it is a receiver architecture that uses less

© University of Pretoria

processing, hence the processing time is mainly as a results of the DF algorithm.

Table 4.1: Average processing times for the different DF algorithms.

Algorithm	**Receiver**	
	BPF-Channeliser	**Basic-FFT**
MuSiC	22 h 3 min	4 h 34 min
Root-MuSiC	17 h 46 min	59 min
Root-Search-MuSiC	19 h 56 min	2 h 17 min
FD-Root-MuSiC	19 h 19 min	1 h 54 min
FD-Linesearch-MuSiC	19 h 17 min	1 h 42 min
WLS-FD-Root-MuSiC	19 h 45 min	2 h 9 min
WLS-FD-Linesearch-MuSiC	19 h 16 min	1 h 54 min

From the processing times it shows that the most processing intensive algorithm is the spectral MuSiC algorithm, as is expected. The least processing intensive algorithm is the Root-MuSiC. All other algorithms have relatively similar processing times. The processing time difference between the receivers are significant, however it will be discussed in section 4.3.2.

4.3.2 Receiver comparison

This section considers the influence of the receiver architecture on the DF performance. The legend for this section is shown in Figure 4.14.

Figures 4.15 to 4.17 compare the different receiver architectures and post-integration methods. The results are generated from a simulation for a UCA of 5 elements with a Gaussian window ($BT = 3$) for the first and second windows, and utilises the FD-Root-MuSiC algorithm.

Similar to the previous section, a UCA is selected as it allows 360° coverage, has no array ambiguities and consists of relatively few elements. A Gaussian window is selected as it has low SLL with a relative small main lobe width increase. The FD-Root-MuSiC algorithm is used as it requires relatively little processing (in comparison to the MuSiC and WLS-FD-RootMuSiC), and as it does not require a mathematical array transformation (in contrast to Root-MuSiC), while it is not limited to a step size (as is the case in the line-search based algorithms).

© University of Pretoria

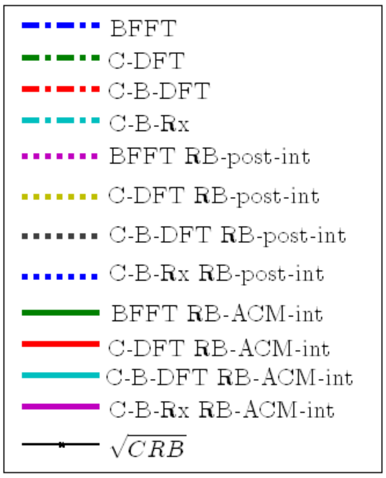

Figure 4.14: Legend for receiver comparison.

Figure 4.15 shows the performance for RB 1, Figure 4.16 for RB 2, and Figure 4.17 for RB 3.

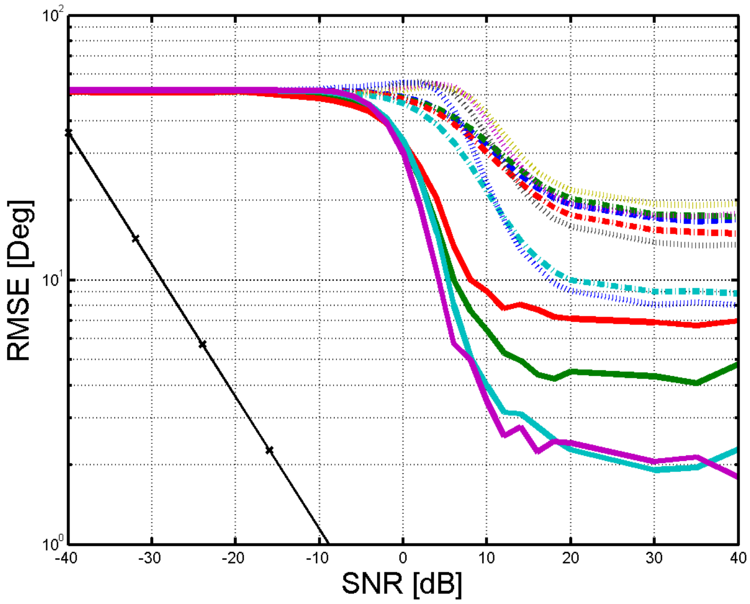

Figure 4.15: Receiver architecture comparison using a UCA of 5 elements, a Gaussian window with $BT = 3$ and the FD-Root-MuSiC algorithm for RB 1.

Using ACM post-integration yields the best result in terms of post-integration methods (Figure 4.17). There is a clear performance increase in systems that use more than one snapshot of data for the ACM approximation. However, the difference between 3072 snapshots (ACM

© University of Pretoria

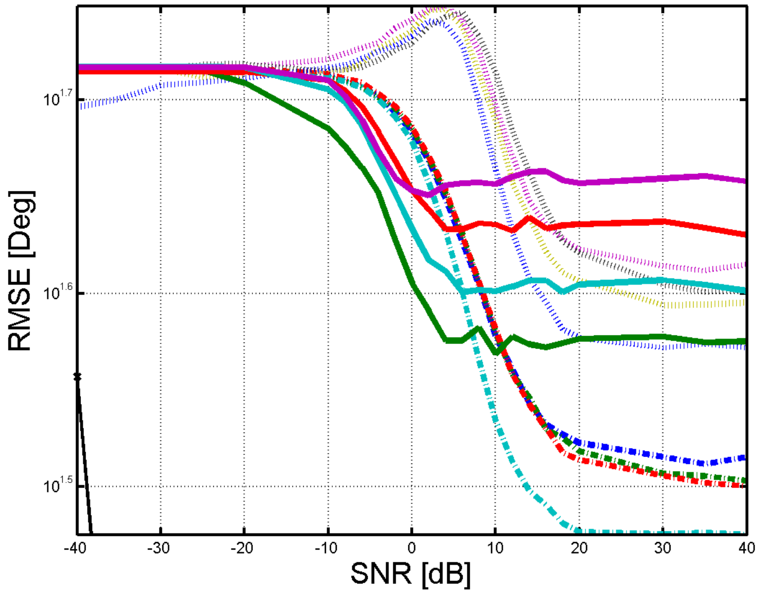

Figure 4.16: Receiver architecture comparison using a UCA of 5 elements, a Gaussian window with $BT = 3$ and the FD-Root-MuSiC algorithm for RB 2.

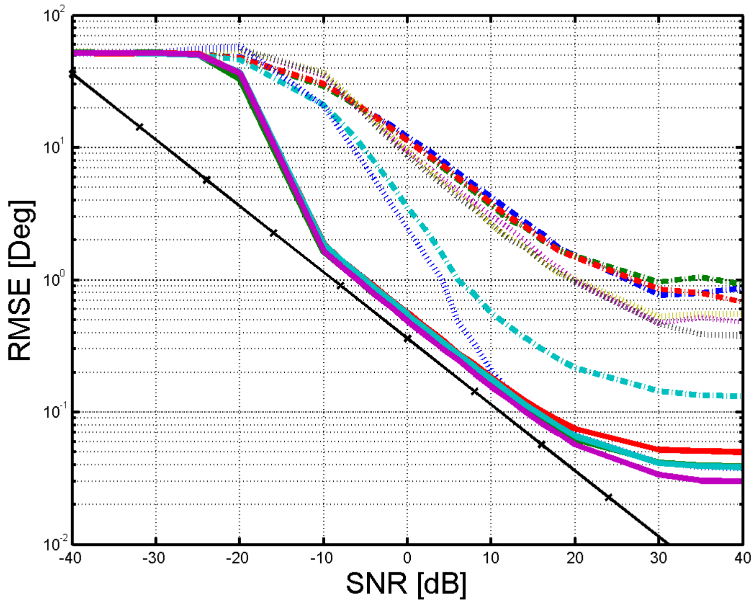

Figure 4.17: Receiver architecture comparison using a UCA of 5 elements, a Gaussian window with $BT = 3$ and the FD-Root-MuSiC algorithm for RB 3.

© University of Pretoria

Table 4.2: Average Processing Time

Receiver	**Processing time**
Basic FFT	2 h 14 min
Basic Channeliser	4 h 3 min
Filtered Channeliser	6 h 49 min
Filtered ACM-integration Channeliser	19 h 19 min

integration receiver with RB ACM integration) and 12 snapshots (only RB ACM integration for all results) seem negligibly small for the strongest signal. This demonstrates that excessive integration of the ACM does not yield significant benefits for the processing it requires.

The channeliser does not have a significant advantage over the Basic-FFT method for strong signals (RB 3 and Figure 4.17); however, the channeliser has a significant improvement for signals with greater interference (RB 1 and Figure 4.15). Additional filtering in the channeliser greatly improves performance as interference and out-of-band noise is significantly reduced (RB 1 and Figure 4.15). These results show that using good signal separation receivers, like the channeliser, performance is increased in multi-signal environments, as the interference is reduced. In the case of OFDM it is a good isolation technique, and it can be applied to various signalling systems.

An interesting observation is that in Figure 4.16 the results for the RB post-integration are not monotone descending, as they have a local maximum of the RMSE near 5 dB SNR (the maximum is slightly different for each case). This local maximum, which causes the RMSE to increase, may either be due to the fact that the DF algorithms lock onto the neighbouring signal of RB 3, or due to a deficiency in the integration algorithm, or both.

The average calculation time of simulations for each receiver type is shown in Table 4.2. The ACM integration method over all channelised data is the most processing intensive, but it provided the best results for all signals (Figures 4.15 to 4.17). By comparison, the Basic-FFT method used approximately an eighth of the processing time (Table 4.2), with very similar results for strong signals. This shows that by selecting the correct receiver architecture a

© University of Pretoria

reduction in the processing can be achieved without a great loss in performance, hence the cost of the receiver can be significantly reduced.

It seems that the single greatest means of improvement of performance is to integrate the ACM of the 12 carriers of each RB (Figures 4.15 to 4.17). The best performance versus processing time trade-off would be the channelised receiver with a BPF per channel and a final DFT using RB ACM integration. This indicates that by selecting a combination of all the integration techniques, relatively good results can be achieved at reduced system processing cost.

The RB 2, which is received at a lower power level and is directly adjacent to RB 3, has significantly worse results (Figures 4.16 compared to 4.17). This shows that some frequency separation between signals is required to reduce the interference. Even with filtering and using appropriate windows for the FFT, the interference cannot be reduced sufficiently for reliable results (Figure 4.16). In frequency dispersive channels (i.e. if Doppler spread is observed), the separation of the signals is even more difficult to achieve [38].

The results show that the receiver selection has a significant impact on the performance of the DF estimation as well as the processing requirements. It therefore emphasises that the receiver architecture has the most influential and crucial effect on the design of a system.

It should also be considered to perform simulations on an optimal computational platform. The simulations are done on a mainly serial-processing platform, therefore parallel processing methods are not optimal and that other processing platforms (e.g. FPGA or dedicated hardware) can result in better processing efficiency for the channeliser based receivers.

4.3.3 Windowing

This section considers the influence of windowing-methods on the DF performance. The legend for this section is shown in Figure 4.18.

Figures 4.19 to 4.24 compare the effects of the different windows used in the receiver architecture. The results are from a simulation for a UCA of 5 elements and utilises the FD-Root-MuSiC algorithm.

© University of Pretoria

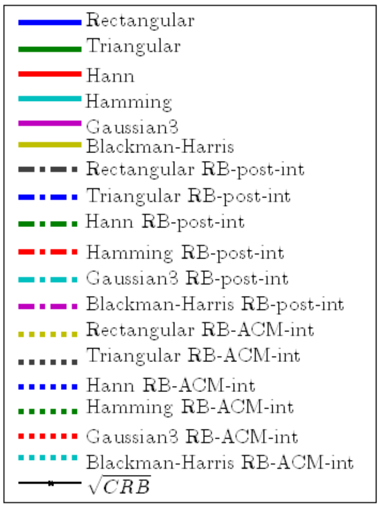

Figure 4.18: Legend for window comparison.

Similar to the previous section, a UCA is selected as it allows 360° coverage, has no array ambiguities and has relatively few elements. The FD-Root-MuSiC algorithm is selected for its processing, robustness, and it is not limited by search operations.

Figures 4.19 to 4.21 consider a Basic-DFT architecture. A Basic-DFT receiver has double the number of frequency-taps than the OFDM signal in the given bandwidth, hence the side-lobe reduction is increased due to oversampling.

Figures 4.19 and 4.22 show the performance for RB 1, Figures 4.20 and 4.23 for RB 2, and Figures 4.21 and 4.24 for RB 3.

From the results for the Basic-FFT receiver (Figures 4.19 to 4.21), it shows that the best performing window is the rectangular window. The largest difference in the windows are observed in the saturation region for RB-ACM integration. The Hamming, Hann and triangular windows have similar performance (Figures 4.19 and 4.20).

The window with the poorest performance for RB-ACM integration for all three RBs is the Blackman-Harris window (Figures 4.19 and 4.20), and the Gaussian window performing the second poorest. This is counter-intuitive, as these windows have the lowest SLL, hence maximum signal isolation. On the other hand, these two windows have the broadest main lobe, hence signals with little frequency separation experiences great interference.

© University of Pretoria

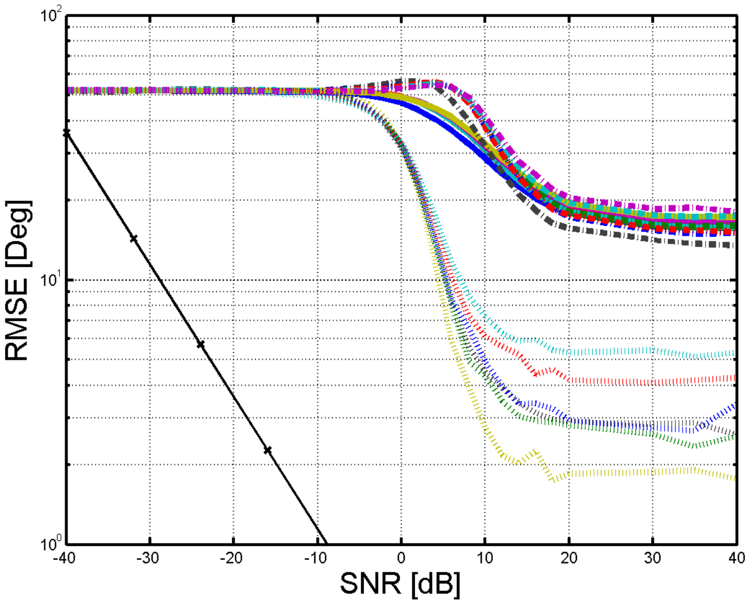

Figure 4.19: Window comparison using a UCA of 5 elements, the FD-Root-MuSiC algorithm and a Basic-FFT receiver architecture for RB 1.

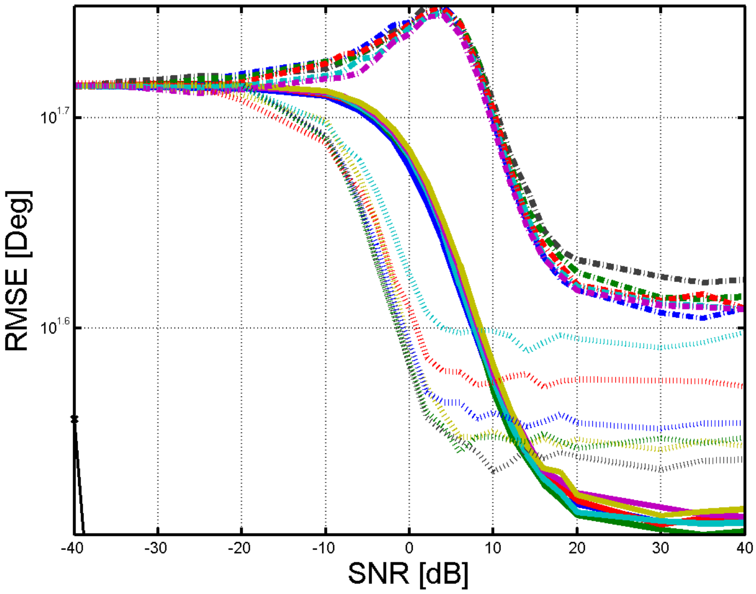

Figure 4.20: Window comparison using a UCA of 5 elements, the FD-Root-MuSiC algorithm and a Basic-FFT receiver architecture for RB 2.

© University of Pretoria

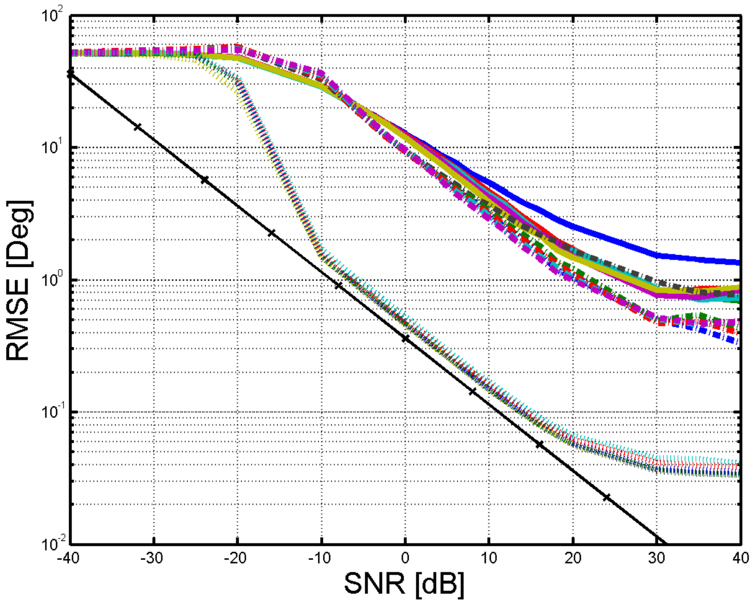

Figure 4.21: Window comparison using a UCA of 5 elements, the FD-Root-MuSiC algorithm and a Basic-FFT receiver architecture for RB 3.

Since the performance difference between the windows is insignificant for RB 3, it can be concluded that for strong non-interfering signals, windowing has negligible benefits. On the other-hand, the influence on windowing has a significant effect for interfering signals (Figures 4.19 and 4.20).

Figures 4.22 to 4.24 consider a channeliser architecture with a DFT. A channeliser architecture has two DFT stages, hence a window can be placed at both stages and the effective window of the data for the receiver is the convolved result of the two windows. The SLL reduction and main lobe broadening will therefore be considerably increased in this architecture. Note that the architectures that use ACM integration rather than the DFT do not have a secondary window stage.

The results for the channeliser receiver (Figures 4.22 to 4.24), are similar to the observations for the Basic-FFT receiver: the differences between the windowing methods are greatest for interfering signals (RB 1 and RB 2), the rectangular window performs best, the Blackman-Harris window performs worst, and the performance differences between the windows are most clearly visible in the saturation region for RB-ACM integration methods.

© University of Pretoria

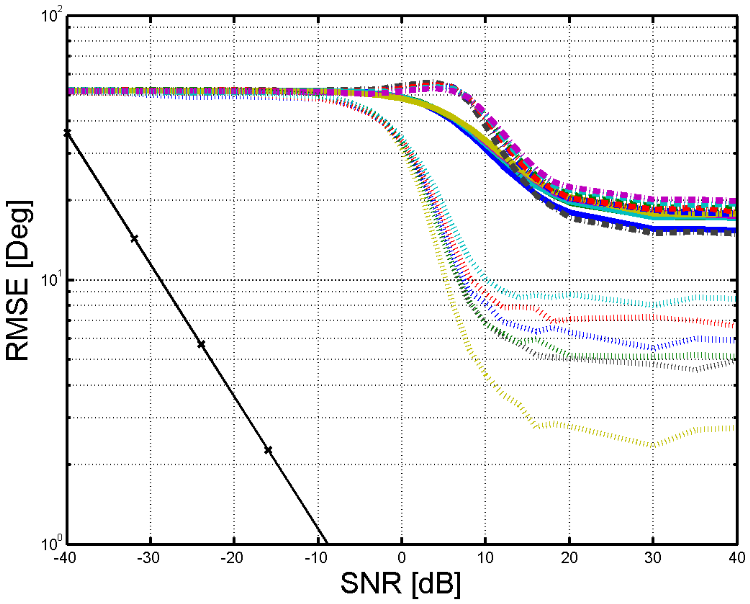

Figure 4.22: Window comparison using a UCA of 5 elements, the FD-Root-MuSiC algorithm and a channeliser with a secondary DFT architecture for RB 1.

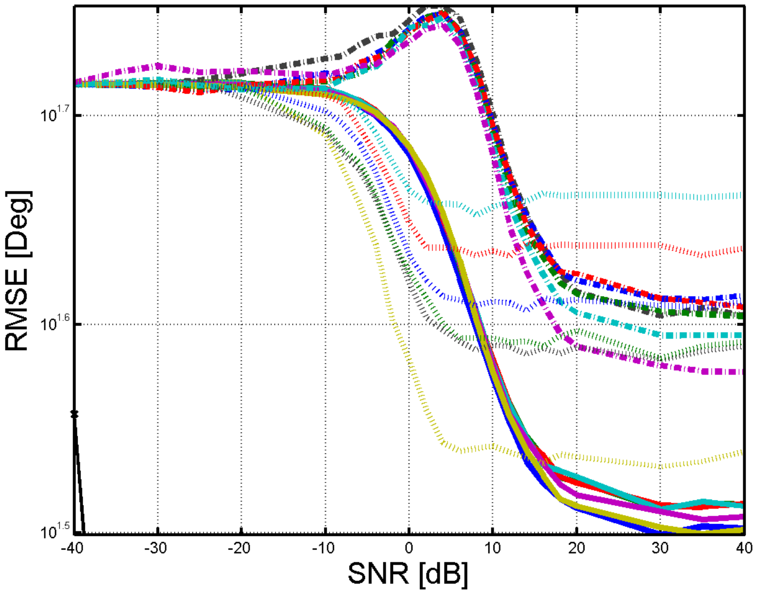

Figure 4.23: Window comparison using a UCA of 5 elements, the FD-Root-MuSiC algorithm and a channeliser with a secondary DFT architecture for RB 2.

© University of Pretoria

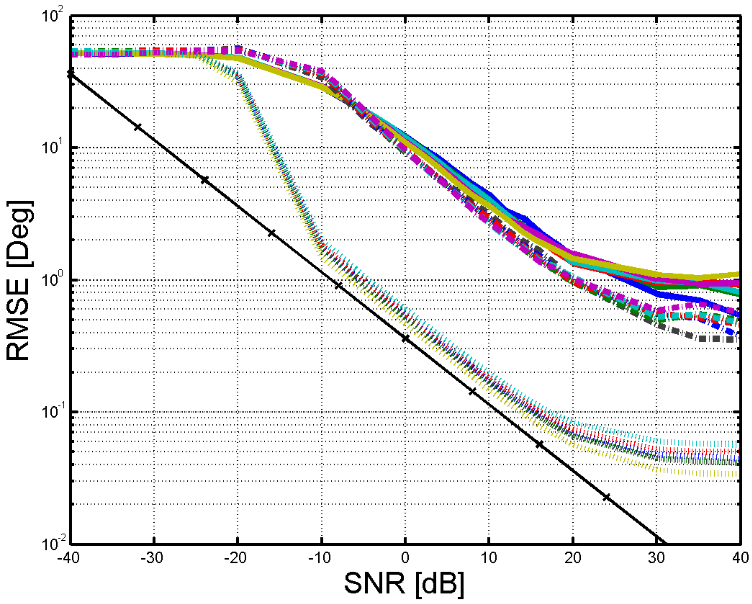

Figure 4.24: Window comparison using a UCA of 5 elements, the FD-Root-MuSiC algorithm and a channeliser with a secondary DFT architecture for RB 3.

The results have shown that windowing has an effect on interfering signals, however in the case of the simulation it has shown that using no windowing gives the best results. This is counter-intuitive, however it shows that side-lobe broadening is more detrimental to the signal processing than the benefits of SLL reduction.

Another argument can be made that windowing removes the orthogonality from the signal, hence it causes interference instead of removing it. In frequency-flat stationary channels this would be true, however fading effects can cause the loss of orthogonality as well. Therefore there is the possibility that windowing is beneficial in fading channels.

Figures 4.25 to 4.27 consider a Basic-DFT architecture in a EVA 70 Hz channel. Figures 4.25 to 4.27 show that a rectangular window is no longer the optimal window to use. For RB 1 the best performing windows in order of merit are the Hamming, triangular and then the Hann windows (Figure 4.25). The rectangular window still offers better performance than the Gaussian and Blackman-Harris windows. Similar results are observed for RB 2 (Figure 4.26). The results for RB 3 show that the influence of the windows are negligible (Figure 4.27).

© University of Pretoria

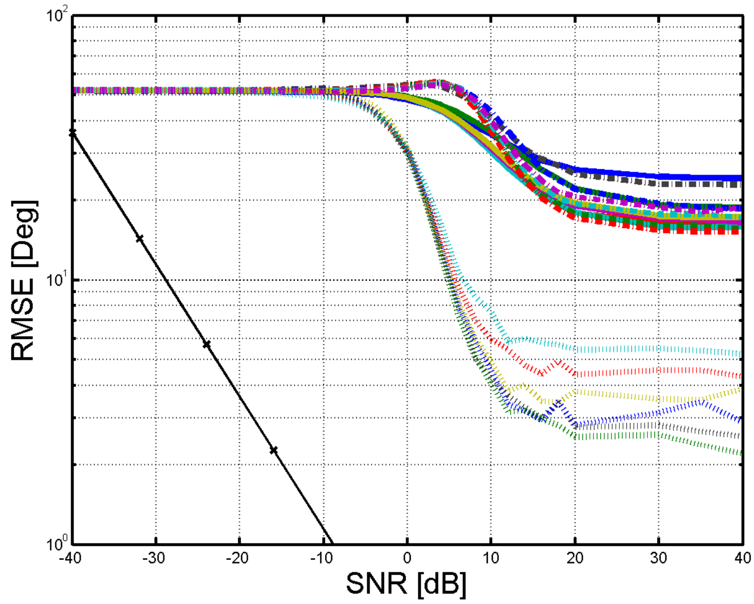

Figure 4.25: Window comparison using a UCA of 5 elements, the FD-Root-MuSiC algorithm and a Basic-FFT receiver architecture for RB 1.

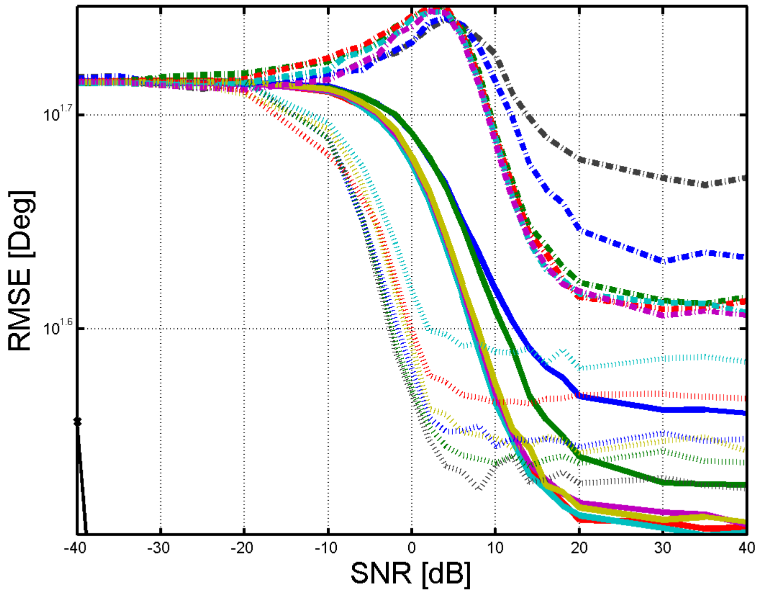

Figure 4.26: Window comparison using a UCA of 5 elements, the FD-Root-MuSiC algorithm and a Basic-FFT receiver architecture for RB 2.

© University of Pretoria

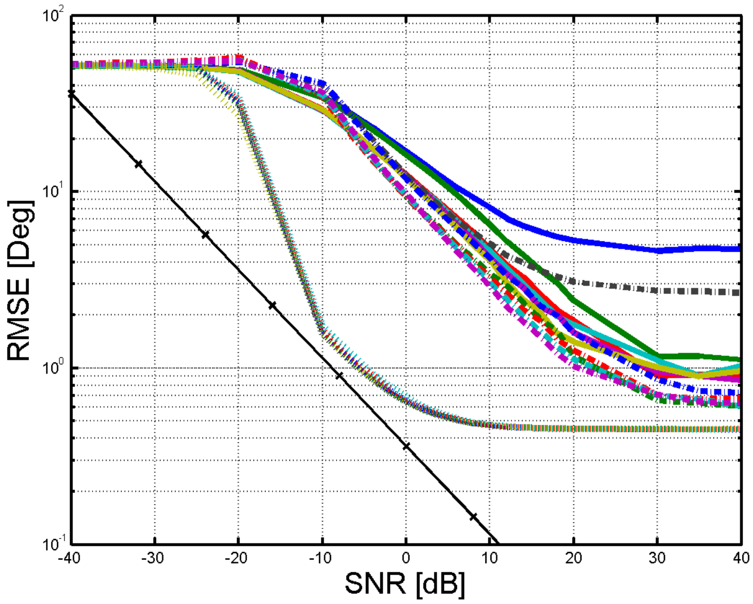

Figure 4.27: Window comparison using a UCA of 5 elements, the FD-Root-MuSiC algorithm and a Basic-FFT receiver architecture for RB 3.

In comparison to the frequency-flat static channel results (Figures 4.19 to 4.21), the results for the fading channel are poorer (Figures 4.25 to 4.27). This is shown clearly for RB 3 where the saturation region occurs earlier in the fading channel (Figure 4.27).

Figures 4.28 to 4.30 consider a channeliser architecture with a DFT in a EVA 70 Hz channel. These results shows that a rectangular window is optimal, as in the frequency-flat static channel case (Figures 4.28 to 4.30 vs. Figures 4.22 to 4.24). As with the Basic-FFT case, the results are slightly poorer due to the fading, and it is best visible for RB 3 (Figure 4.30).

The final results show that windowing is only beneficial in fading channels for Basic-FFT receivers. For other cases better results are achieved if a rectangular window is used. Windows with broad main-lobes tend to be detrimental to the AOA estimation in the specified case. This is due to the fact that the signals do not exhibit enough frequency separation. In the case where greater frequency separation is achieved between two signals, windowing may have some benefits.

© University of Pretoria

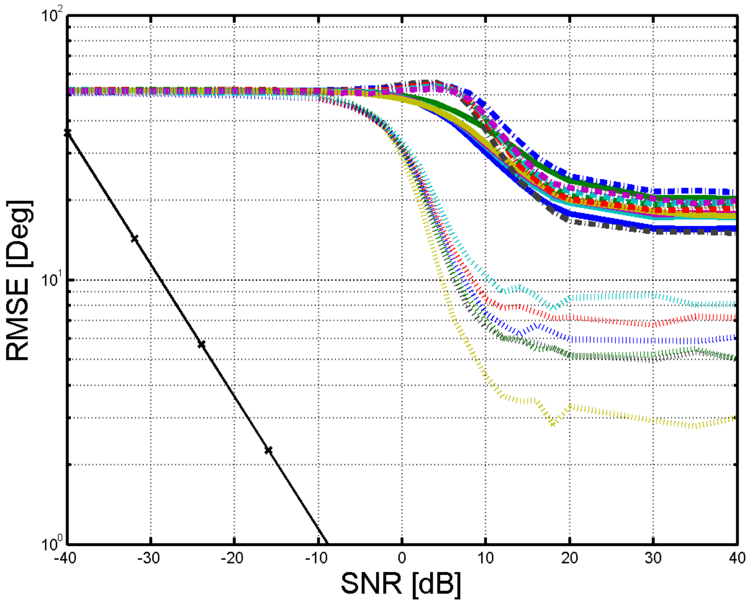

Figure 4.28: Window comparison using a UCA of 5 elements, the FD-Root-MuSiC algorithm and a channeliser with a secondary DFT architecture for RB 1.

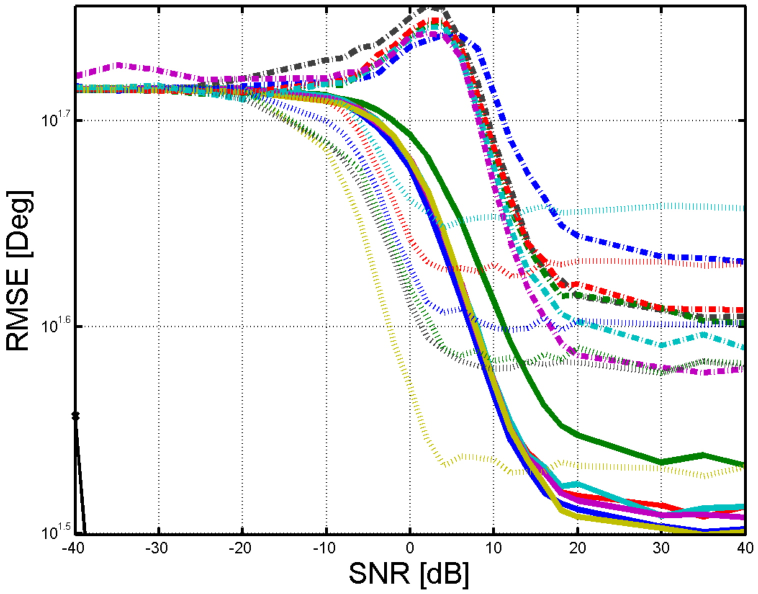

Figure 4.29: Window comparison using a UCA of 5 elements, the FD-Root-MuSiC algorithm and a channeliser with a secondary DFT architecture for RB 2.

© University of Pretoria

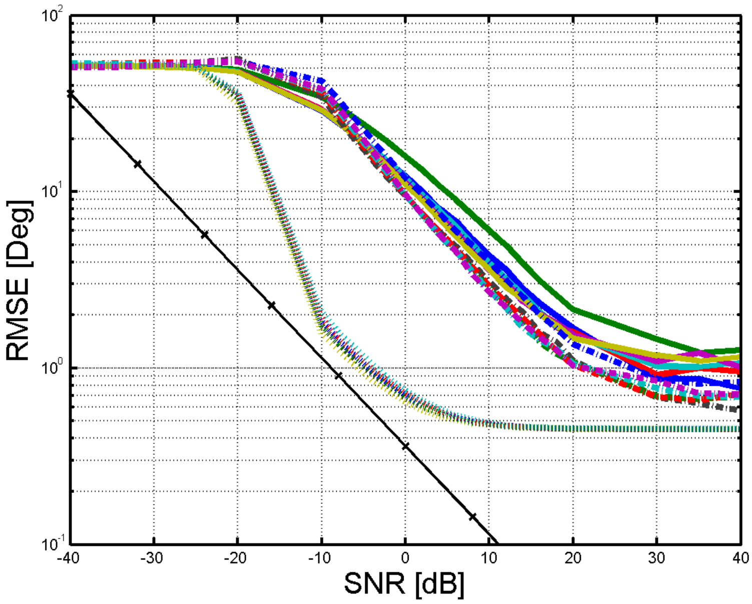

Figure 4.30: Window comparison using a UCA of 5 elements, the FD-Root-MuSiC algorithm and a channeliser with a secondary DFT architecture for RB 3.

4.3.4 Sensor Array comparison

This section considers the influence of the array geometry on the DF performance. The legend for this section is shown in Figure 4.31.

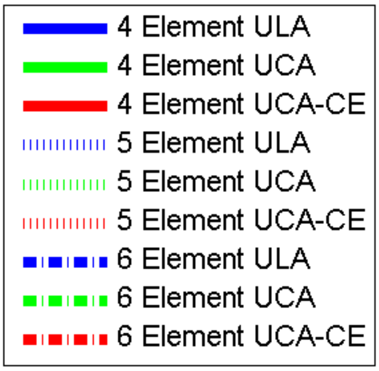

Figure 4.31: Legend for array comparison.

Figures 4.32 to 4.34 show the results for no post-integration.

The results are from a simulation using the FD-Root-MuSiC algorithm, as it is applicable

© University of Pretoria

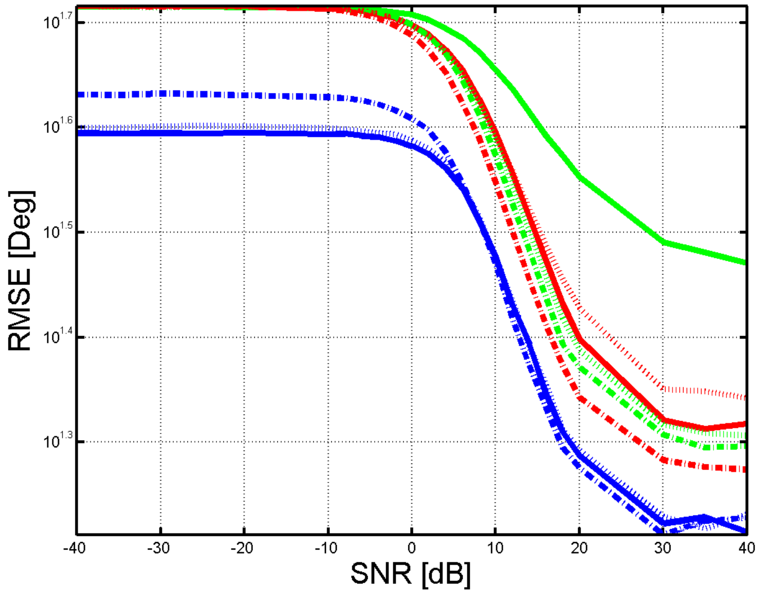

Figure 4.32: Array comparison with a FD-Root-MuSiC algorithm using a Gaussian window channeliser with a secondary DFT architecture and with no post-integration of RB 1.

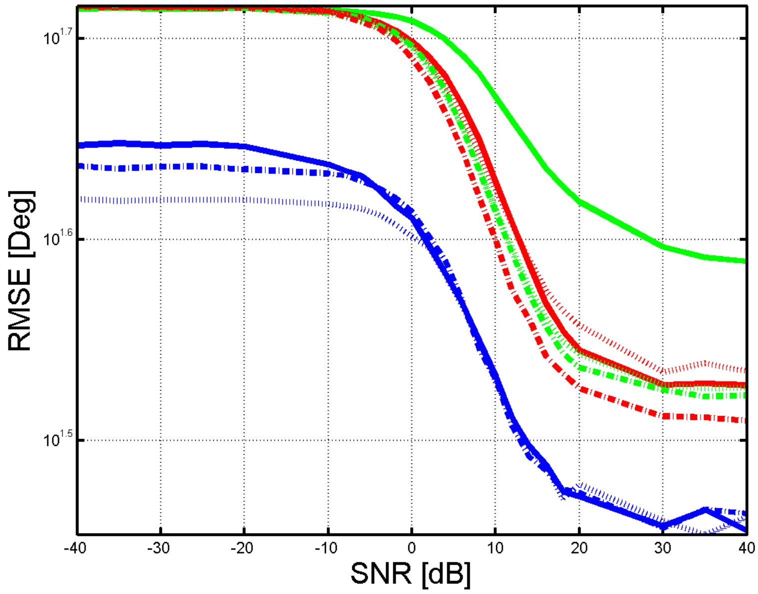

Figure 4.33: Array comparison with a FD-Root-MuSiC algorithm using a Gaussian window channeliser with a secondary DFT architecture and with no post-integration of RB 2.

© University of Pretoria

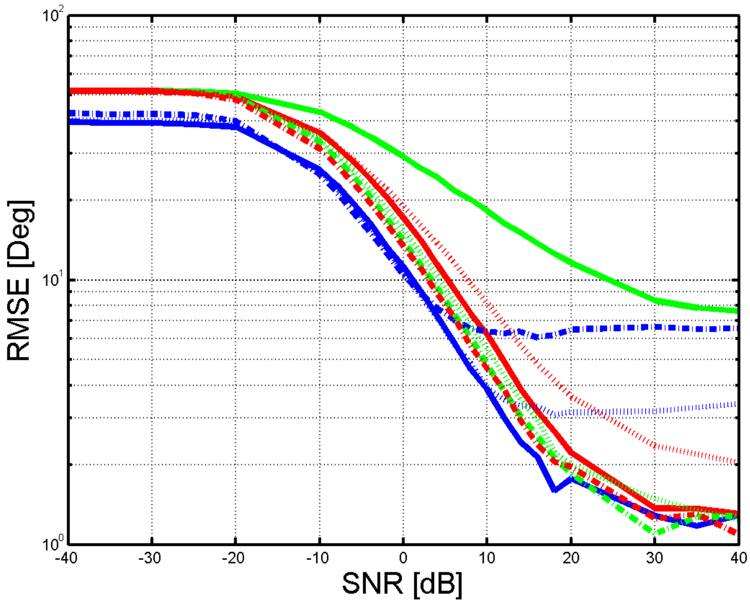

Figure 4.34: Array comparison with a FD-Root-MuSiC algorithm using a Gaussian window channeliser with a secondary DFT architecture and with no post-integration of RB 3.

to all array configurations without the need of mathematical transformations. The UCA based arrays are simulated over a 360° azimuth, and the ULA based arrays are simulated over a 120° azimuth coverage to compensate for array ambiguities. The ULA based arrays are assumed for a sectored system that has three sectors, each with a bandwidth of 120°. A channeliser with a secondary DFT architecture is selected as it has relative good results and requires little processing time (see section 4.3.2).

In all figures the RMSE in the noise dominant region is considerably lower for a ULA than for a UCA (Figures 4.32 to 4.37). This can be explained by the fact that the AOA estimation for a ULA is bounded to compensate for the 180° ambiguity of the array. The ULA arrays only observe signals over an azimuth range of 120°, whereas the UCA based arrays observe signals over the full 360° range. Therefore the expected maximum error for a ULA is lower.

The results for both RB 1 and RB 2 (Figures 4.32 and 4.33) show that the ULA have lower RMSE values than the UCA based arrays. The same is not true with RB 3, as the saturation region has higher RMSE values for ULA in comparison to the UCA based arrays (Figure 4.34). This shows that ULA have an improved performance for interfering signals and in low SNR conditions. All results for RB 1 and RB 2 (Figures 4.32 and 4.33) are poor as none of the

© University of Pretoria

arrays yield sub 10° accuracy. RB 3 does achieve an accuracy smaller than 10° at high SNR for all arrays.

RB 3 has the best RMSE values (Figure 4.38), followed by RB 1(Figure 4.32), and RB 2 has the poorest values (Figure 4.35). This is consistent with all previous results.

Figures 4.35 to 4.37 show the results for RB post-integration. The results for RB integration shows that improved RMSE values are achieved, this is consistent with previous results and as expected. The ULA arrays for RB 1 achieve RMSE values near 10° for high SNR. This shows great improvement above the UCA. However it should still be noted that the FOV for the ULA is smaller, hence improved results is to be expected.

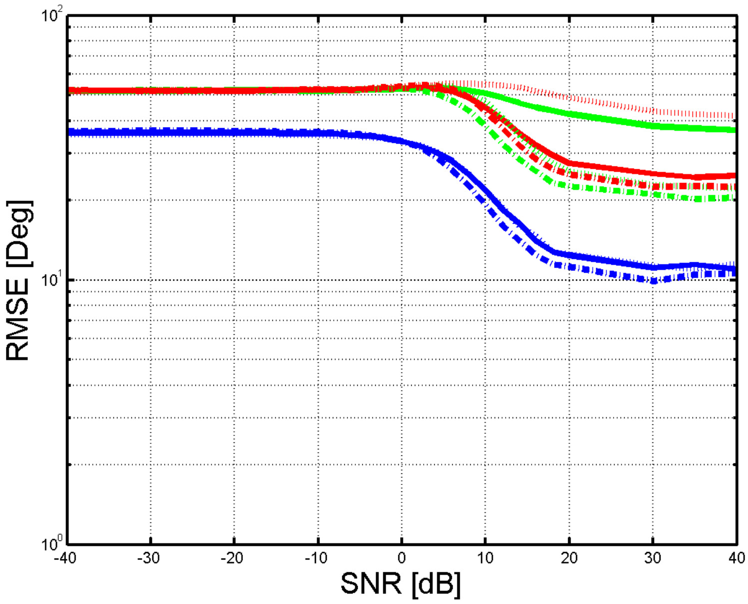

Figure 4.35: Array comparison with a FD-Root-MuSiC algorithm using a Gaussian window channeliser with a secondary DFT architecture and with post-integration of RB 1.

The results for both RB 1 and RB 2 (Figures 4.35 and 4.36) show that the ULA have lower RMSE values than the UCA based arrays. The same is not true with RB 3, as the saturation region has higher RMSE values for ULA in comparison to the UCA based arrays (Figure 4.37). This shows that ULA have an improved performance for interfering signals and in low SNR conditions.

© University of Pretoria

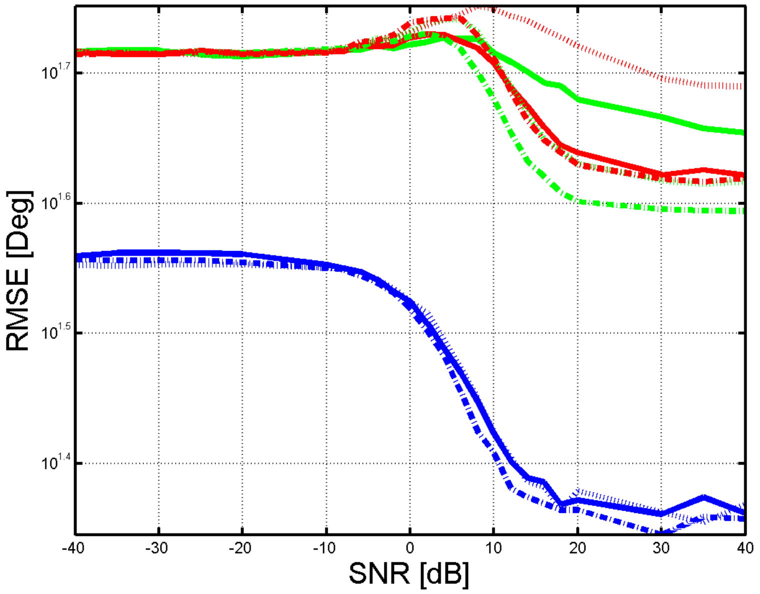

Figure 4.36: Array comparison with a FD-Root-MuSiC algorithm using a Gaussian window channeliser with a secondary DFT architecture and with post-integration of RB 2.

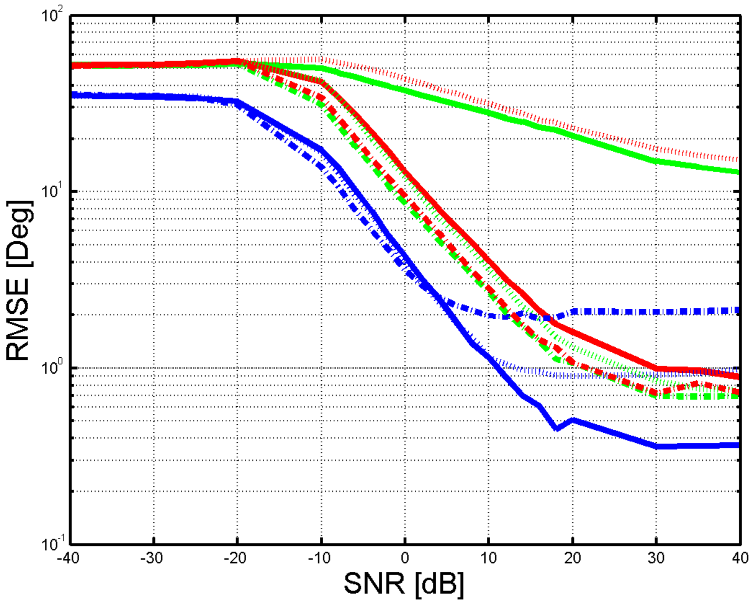

Figure 4.37: Array comparison with a FD-Root-MuSiC algorithm using a Gaussian window channeliser with a secondary DFT architecture and with post-integration of RB 3.

© University of Pretoria

The 4-element UCA and the 5-element UCA-CE yielded poor results in comparison to the other arrays, and this is especially evident for non interfering signals (Figure 4.37). This is caused by an 180° array ambiguity which occurs every 90° when a far-field signal approaches the array in line with an element position towards the centre of the array. Typically the RMSE performance of an array configuration improves as the number of elements increases. However structural ambiguities cause great errors and results in exceptions.

Figures 4.38 to 4.40 shows the results for ACM-RB integration.

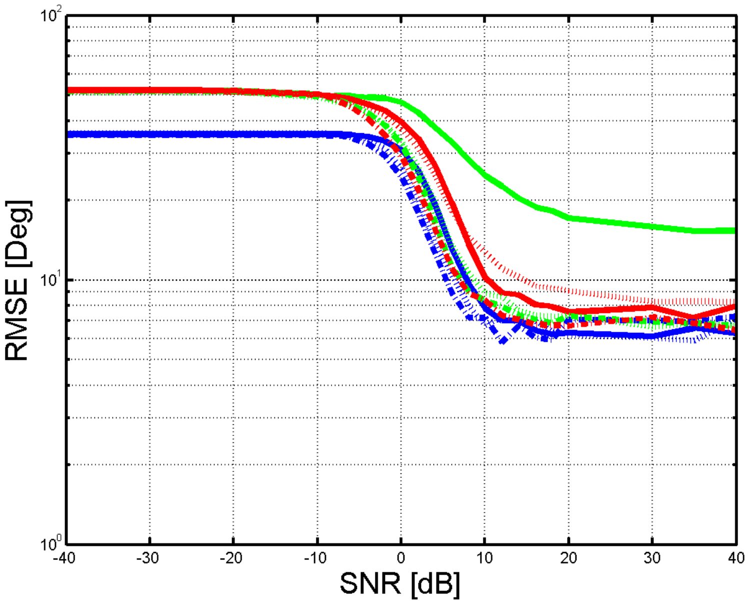

Figure 4.38: Array comparison with a FD-Root-MuSiC algorithm using a Gaussian window channeliser with a secondary DFT architecture and with ACM post-integration of RB 1.

The saturation region of the ACM-RB method block for RB 3 (Figure 4.40) for ULAs has poor results. These are also the only results that have non-monotone RMSE with a minima. This local minima (e.g. at −10 dB SNR for a 6-element ULA) are caused by the FD-Root-MuSiC algorithm. To validate this statement a subsection of the results of the Root-MuSiC algorithm is shown for RB 3 in Figures 4.41 to 4.43. The results of the Root-MuSiC algorithms show that the graphs are indeed monotone-decreasing over all SNR values. The UCA-CE still uses the FD-Root-MuSiC algorithm, as the mathematical transformation for the Root-MuSiC algorithm for this array has not been developed.

© University of Pretoria

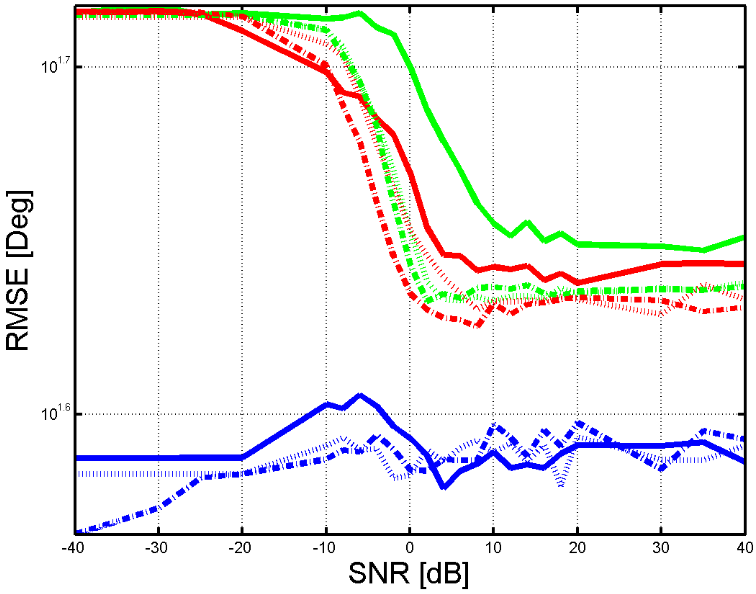

Figure 4.39: Array comparison with a FD-Root-MuSiC algorithm using a Gaussian window channeliser with a secondary DFT architecture and with ACM post-integration of RB 2.

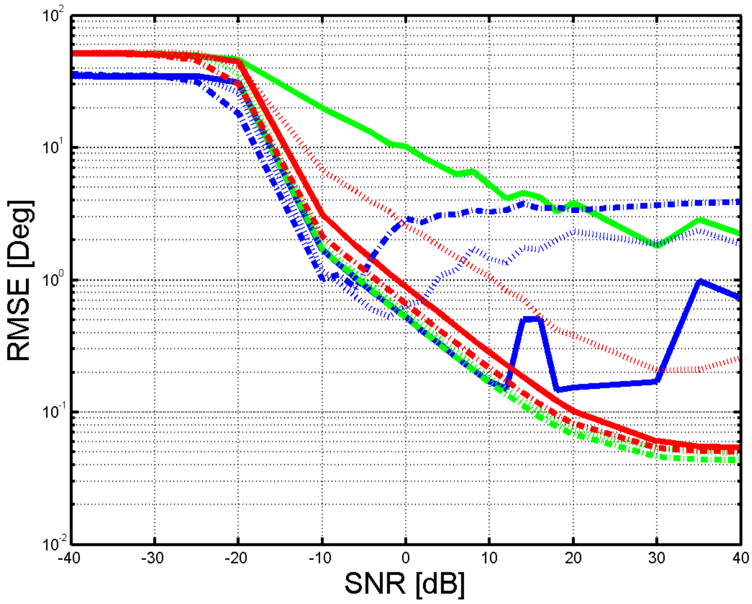

Figure 4.40: Array comparison with a FD-Root-MuSiC algorithm using a Gaussian window channeliser with a secondary DFT architecture and with ACM post-integration of RB 3.

© University of Pretoria

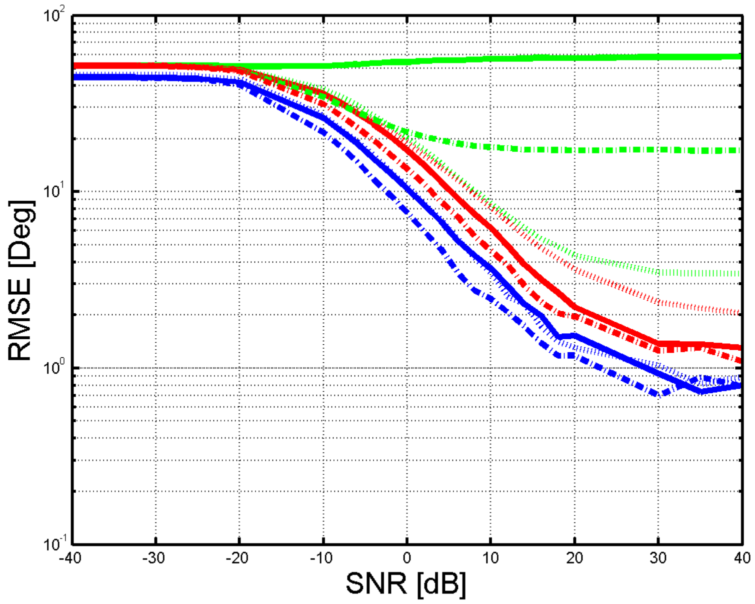

Figure 4.41: Array comparison with a Root-MuSiC algorithm using a Gaussian window channeliser with a secondary DFT architecture and with no post-integration of RB 3.

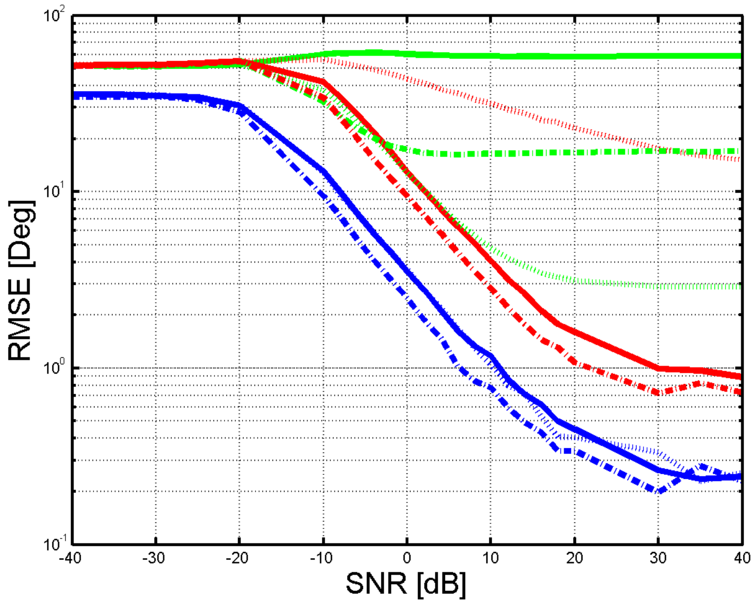

Figure 4.42: Array comparison with a Root-MuSiC algorithm using a Gaussian window channeliser with a secondary DFT architecture and with post-integration of RB 3.

© University of Pretoria

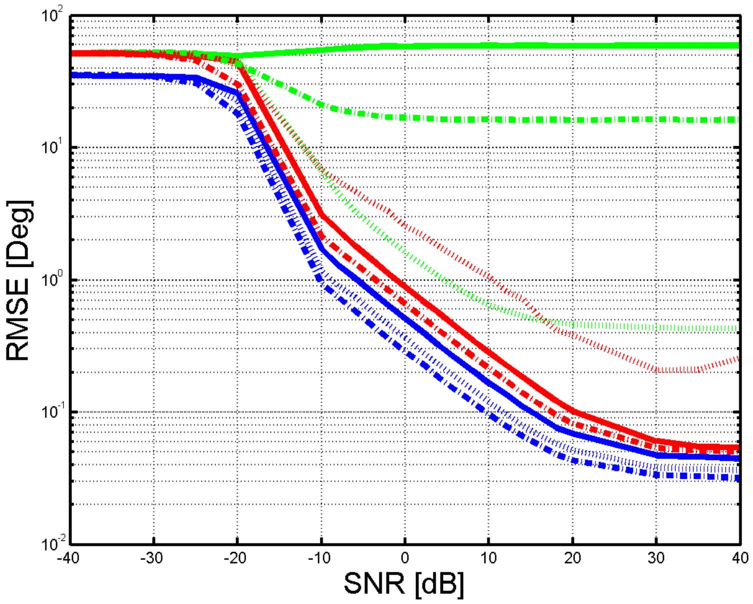

Figure 4.43: Array comparison with a Root-MuSiC algorithm using a Gaussian window channeliser with a secondary DFT architecture and with ACM post-integration of RB 3.

Figure 4.41 shows the results for no post-integration, Figure 4.42 shows the results for RB post-integration, and Figure 4.43 shows the results for RB-ACM post-integration. The results show that the Root-MuSiC algorithm does not have an early saturation region (Figures 4.41 to 4.43) as shown for the FD-Root-MuSiC algorithm (Figures 4.34, 4.37, and 4.40).

4.3.5 System optimisation

This section uses the simulation results to determine the Pareto efficiency of the variables for minimum simulation time (processing requirements) and the minimum RMSE at certain SNR values.

For the analysis the SNR values of -10 dB, 0 dB, 10 dB and -10 dB are considered as they present the following cases:

1. Noise dominant: The noise is stronger than the signal present,
2. Weak signal: noise has a significant influence as it has equal power to the signal,
3. Moderate signal: sufficiently high SNR for the signal to be dominant,

© University of Pretoria

4. Strong signal: high SNR where the influence of the noise is negligible.

A Pareto efficient point is a data point which cannot be improved for a certain parameter without the reduction of another parameter. This results in a selection of optimal receivers for multiple parameters. The Pareto efficient points forms a Pareto front which allows selection of the optimal design parameters.

All the previous results can be incorporated for the analysis. A small subset of additional simulations can be performed using the simulation profiles that are on the Pareto front and by changing some of the parameters for these profiles using the conclusions of the previous results. This results in an efficient method of finding optimal points without the need of large scale simulations to cover all parameters. The presented results include the additional subset of simulations.

The legend for this section is shown in Figure 4.44. Note that the post-integration methods are observed separately. This is done as the post-integration methods are not separated in the simulations, and hence their contribution to the processing cannot be quantified.

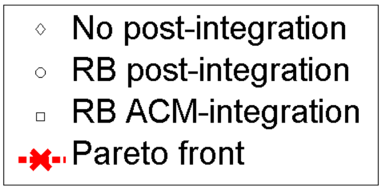

Figure 4.44: Legend for optimisation.

Figure 4.45 shows the analysis for RB 1 and UCA based arrays. Figure 4.46 shows the analysis for RB 2 and UCA based arrays. Figure 4.47 shows the analysis for RB 3 and UCA based arrays. The analysis is done separately for UCA and ULA based arrays, as ULA based arrays have a smaller FOV. A smaller FOV requires more simultaneous systems and should have better RMSE values, as it makes the assumption that signals originate only in the specified FOV. It is therefore an invalid comparison between ULA and UCA based arrays.

There are multiple SNR cases observed as well as three different signals. To further analyse the results, the number of times a simulation profile appears on the Pareto front is calculated. The more often a receiver is on the Pareto the more cases there is where the receiver design

© University of Pretoria

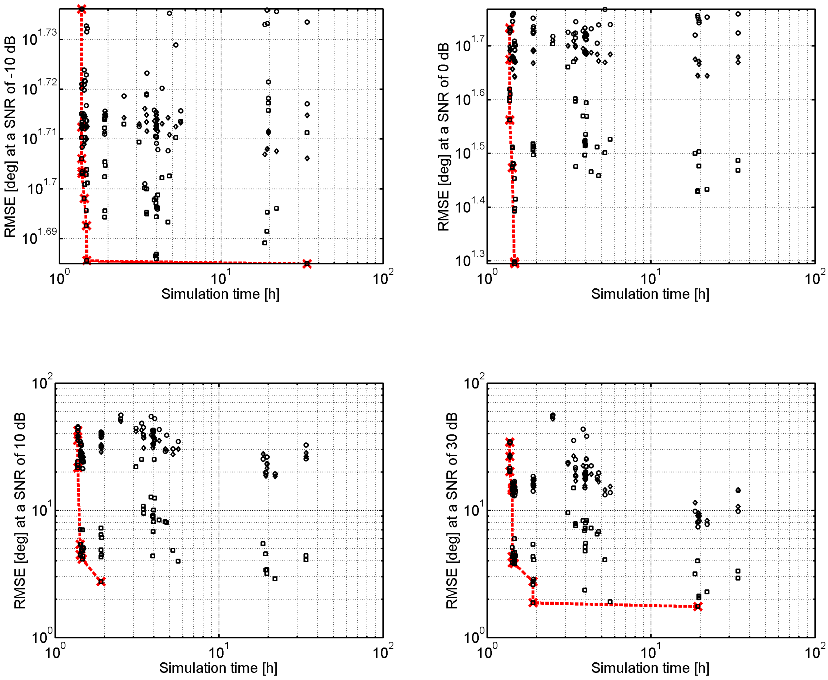

Figure 4.45: Optimisation of RB 1 for UCA based arrays

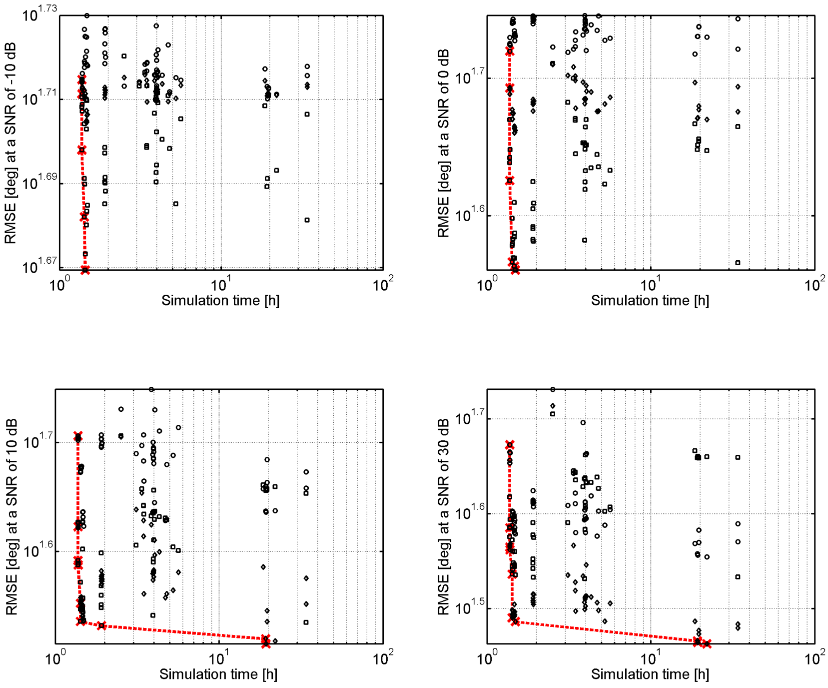

Figure 4.46: Optimisation of RB 2 for UCA based arrays

© University of Pretoria

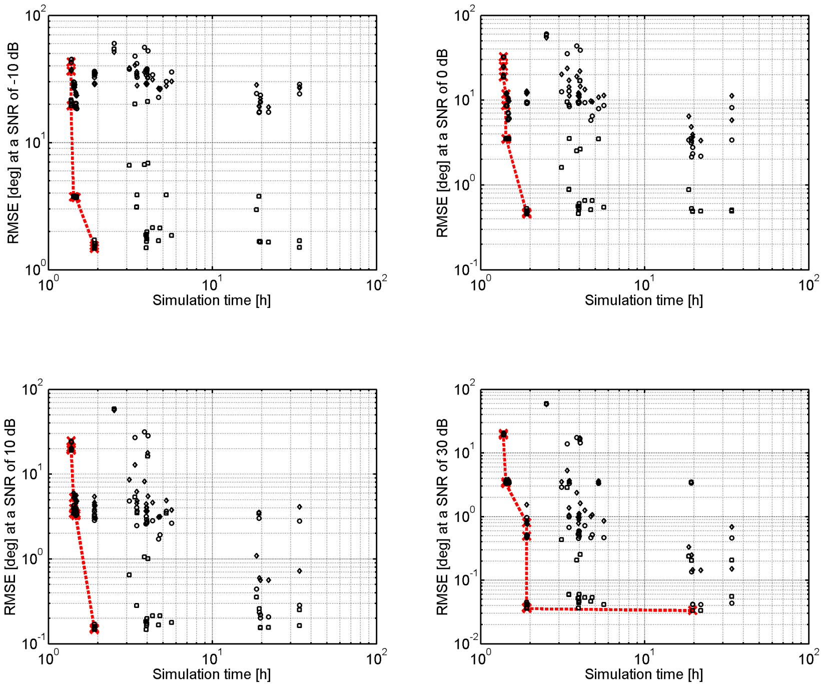

Figure 4.47: Optimisation of RB 3 for UCA based arrays

is a valid optimal point. This method allows a quantifiable analysis to select the best receiver design for a NNC-DF receiver.

Table 4.3 shows the parameters of the simulation profiles which are most frequently on the Pareto front. These simulation profiles are the short list for DF-receiver design with UCA-based arrays.

Based on the results, it shows that the UCA-CE do not feature at all, hence it is an inefficient array configuration, despite the stability it causes on a system.

The most frequent receiver architectures is the Basic-FFT, and it can be contributed to the fact that it is processing efficient and inexpensive. The use of the FD-Linesearch algorithm also reduces processing time. However, the results are poor with a minimum RMSE in the analysis being at 12.1°.

The use of the FD-Root-MuSiC algorithm has significantly better results with only a slight increase in processing time.

© University of Pretoria

Table 4.3: Simulation profiles which are Pareto efficient over multiple scenarios for UCA-based arrays.

Parameter	**Simulation parameters**					
No. of times on Pareto front	11	6	5	4	3	1
Array Type	UCA	UCA	UCA	UCA	UCA	UCA
Number of elements	5	5	5	6	5	5
Receiver type	Basic-FFT	Basic-FFT	Basic-FFT	Basic-FFT	Basic-FFT	Channeliser
NB Filter	-	-	-	-	-	Y
Secondary stage	-	-	-	-	-	ACM-int
Window 1	Triangular	Rectangular	Hann	Rectangular	Triangular	Gaussian
Window 2	-	-	-	-	-	Gaussian
AOA algorithm	FD-LS	FD-Root	FD-Root	FD-LS	FD-Root	FD-Root
Post-integration	ACM-RB	ACM-RB	ACM- RB	ACM-RB	ACM-RB	ACM-RB
Processing time	1 h 25 min	1 h 54 min	1 h 54 min	1 h 28 min	1 h 54 min	19 h 33 min
RMSE [deg] for RB 1						
SNR = -10 dB	2655	2677	2657	2543	2461	2700
SNR = 0 dB	884	1044	1032	395	990	897
SNR = 10 dB	29.1	7.57	23.7	17.1	20	10
SNR = 30 dB	18.7	3.52	7.6	14.6	8	4.2
RMSE [deg] for RB 3						
SNR = -10 dB	14.04	2.2	2.4	13.8	2.2	2.7
SNR = 0 dB	12.27	0.21	0.23	12.4	0.21	0.24
SNR = 10 dB	12.07	0.02	0.023	12.3	0.022	0.024
SNR = 30 dB	12.05	0.0013	0.0014	12.6	0.0013	0.0011
Simulation profile number	42	16	18	41	17	15

Figure 4.48 shows the analysis for RB 1 and ULA based arrays. Figure 4.49 shows the analysis for RB 2 and ULA based arrays. Figure 4.50 shows the analysis for RB 3 and ULA based arrays.

Table 4.4 shows the parameters of the simulation profiles which appears most frequently on the Pareto front for ULA based arrays.

From the analysis the simulation profiles for ULAs it shows that the Basic-FFT receiver architecture is preferred due to its low processing requirements. The Root-MuSiC has a good trade-off between processing and performance.

The simulations for the ULA based arrays require less time. This is due to the fact that a smaller FOV is simulated.

In both the UCA and ULA cases, the use of the Pareto front in conjunction with simulation conclusions lead to improved simulation profile selections. Simulation profiles numbered 40 and above for UCA based arrays, and profiles of 7 and above for ULA based arrays, are

© University of Pretoria

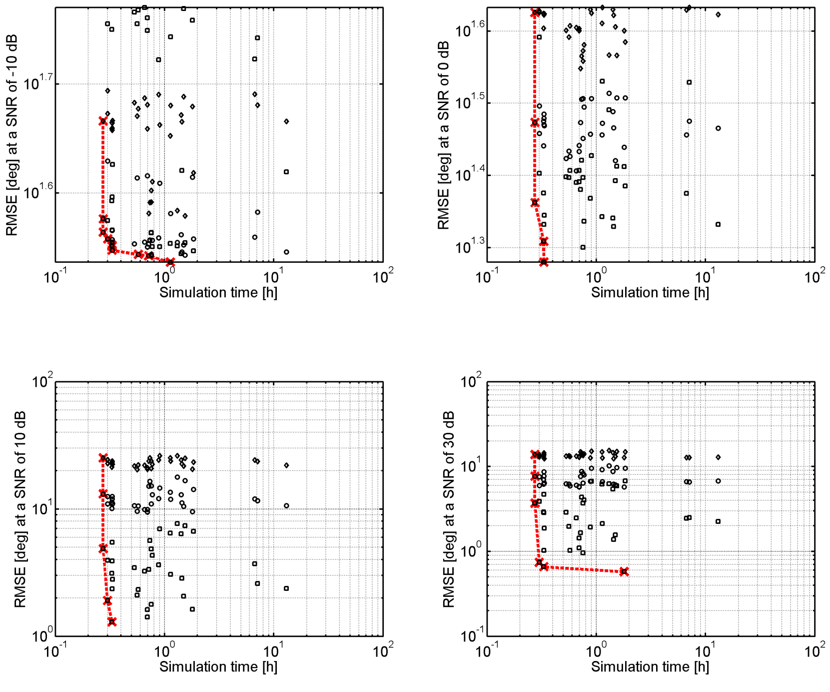

Figure 4.48: Optimisation of RB 1 for ULA based arrays

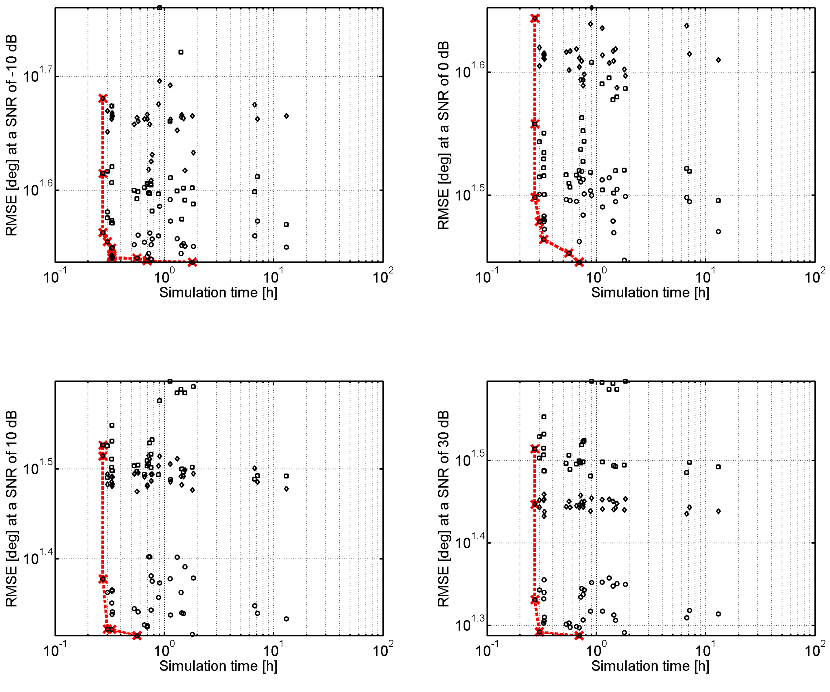

Figure 4.49: Optimisation of RB 2 for ULA based arrays

© University of Pretoria

UNIVERSITEIT VAN PRETORIA
UNIVERSITY OF PRETORIA
YUNIBESITHI YA PRETORIA

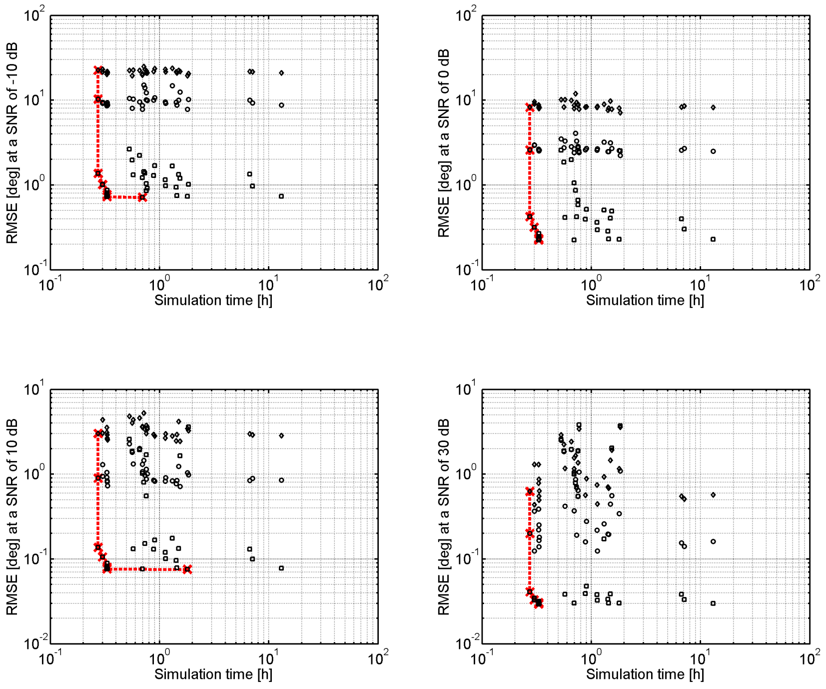

Figure 4.50: Optimisation of RB 3 for ULA based arrays

Table 4.4: Simulation profiles which are Pareto efficient over multiple scenarios for ULA based arrays.

Parameter	**Simulation parameters**					
No. of times on Pareto front	12	6	6	5	2	1
Number of elements	4	5	6	6	6	6
Receiver type	Basic-FFT	Basic-FFT	Basic-FFT	Basic-FFT	Basic-FFT	Basic-FFT
Window 1	Gaussian	Rectangular	Rectangular	Hann	Rectangular	Rectangular
AOA algorithm	Root	Root	Root	Root	MuSiC	Root- Search
Post-integration	ACM-RB	ACM-RB	ACM- RB	ACM-RB	ACM-RB	ACM-RB
Processing time	16 min	18 min	20 min	20 min	1 h 48 min	42 min
RMSE [deg] for RB 1						
SNR = -10 dB	1420	3244	3170	1533	3290	3152
SNR = 0 dB	530	1522	564	414	668	606
SNR = 10 dB	23	3.6	1.68	9.78	2.65	2.0
SNR = 30 dB	13	0.55	0.43	8.46	0.33	1.2
RMSE [deg] for RB 3						
SNR = -10 dB	1.878	1.03	0.53	0.59	0.54	0.51
SNR = 0 dB	0.18	0.1	0.05	0.055	0.053	0.05
SNR = 10 dB	0.019	0.011	0.0058	0.0064	0.0057	0.0058
SNR = 30 dB	0.0017	0.0011	0.00086	0.00092	0.00091	0.00091
Simulation profile number	9	17	19	28	33	32

selected by changing specified parameters on existing simulation profiles that are initially on the Pareto front. From the summary of the results (Table 4.3 and Table 4.4) it shows that

© University of Pretoria

this method is efficient to select a vast parameter space for optimal results.

4.4 CONCLUSION

This chapter presented the simulation results for a NNC-DF receiver system for the case of two frequency-adjacent LTE based signals. Multiple array configuration, algorithms, receiver architectures and windowing methods have been investigated. Optimisation of the simulation parameters have been done through the use of Pareto analysis.

© University of Pretoria

© University of Pretoria

CHAPTER 5

PRACTICAL SYSTEM DEVELOPMENT

5.1 CHAPTER OVERVIEW

This chapter discusses the development of a practical NNC-DF system, based upon the simulation results from Chapter 4.

5.2 SENSOR ARRAY

As shown by the simulation results, the sensor array has a significant influence on the performance of the system.

5.2.1 Number of sensor elements

In theory the sensor array should consist of as many as possible elements, however this causes many practical problems. As the number of elements increase, so does the system cost: as more sensors are used, a receiver is required for each channel, including processing increased for the increase of complexity of the associated DF algorithms. Large arrays also require much space, hence for many applications (especially in the case where mobility is required) the physical structure is too large and impractical. Too few antenna elements on the other hand have reduced DOA accuracy.

The receiver clock stability directly influences the RMSE of the estimation. Therefore clock stability in conjunction with hardware calibration can be used as factors to estimate the lower bound of the RMSE. A sensor array that can estimate more accurately than the hardware-

© University of Pretoria

RMSE bound is therefore considered excessive, hence a limit on the number elements can be determined. Unfortunately the phase stability of the receiver system should first be determined for this approach to be applicable.

Another design approach is to consider commercially available hardware. Software-defined radio (SDR) based architectures offer a relatively cheap and simple commercial option for system design. Most SDRs only have one or two channel architectures, however there are some systems with four channel receivers. Two or four channel receivers have poor DOA estimation for 360° azimuth range, hence the use of a single SDR. Many of these architectures have the option to use external clocking such that multiple devices can be synchronised for DF. However many of these receivers use digital down-converters (DDCs) which also need to be synchronised. It is possible to remove the phase offset caused between two DDCs by calibrating the system on every system start-up, but this is not always a practical approach. In general a SDR sends the measured data to a host-device for processing, hence stacking multiple SDRs together requires a single host that is capable of processing the full received data bandwidth. The host-device is therefore a limiting factor on the total number of SDRs that can be used in parallel.

Using SDR based architectures, the following options can be considered:

1. Three **Ettus B210 SDRs** [62,63] with an **Octoclock** for synchronisation, as it allows a six-channel receiver to be build. A method of calibrating the DDC offset between the three SDRs is required for this configuration. Such a system will allow 360° unambiguous coverage with relative little required processing and hardware. SDRs from Ettus are commonly used for research [64–74], due to the low cost, accessibility and adaptability for multiple applications.
2. A **Per Vices Crimson** SDR [63, 75, 76] as it is a fully synchronised four-channel receiver. No additional clocking considerations is required as all channels are on the same platform. This option limits the array configurations for 360° azimuth coverage as ambiguities may be present. However if a sectored approach is followed (i.e. linear-arrays are used) the system will be more practical.

National Instruments (NI) offers some commercial options with fully synchronised multiple-channel receivers (e.g. the FlexRIO [77–79]), however this option is much more expensive

© University of Pretoria

than most SDRs. Another option is to develop a hardware platform specifically for the application, however this will also be very expensive due to development costs.

5.2.2 Array configuration

The array configuration determines whether ambiguities are present, the array size, which AOA algorithms can be used, and the performance of the algorithms. Many arrays achieve excellent results forNB signals, however they have ambiguities at other frequencies. Uniform arrays tend to have good results for NB operation, but they are not suitable for WB operation.

Linear arrays have excellent results and are directly applicable to most AOA algorithms, however they have a limited range of operation caused by ambiguities. If 360° operation is not required or if a sectored system can be developed, then linear arrays have superior performance and are preferred. The use of non-uniform spacing, such as logarithmic spacing can easily increased the operational bandwidth of a linear array, hence simple WB systems can be developed.

If 360° azimuth operation is required and only a single system may be used (i.e. no sectoring) then circular arrays can be implemented. Circular arrays are less sensitive to system bandwidth for large arrays, however it is still possible to achieve with a small number of array elements. Another option is to use stochastic spacing of elements on a plane, as it is stochastically unambiguous, however it may be difficult to manufacture (custom mounting at arbitrary positions) and the array may have reduced sensitivity at certain bearings.

As the system design of this dissertation considers a NB signal (540 kHz at 1 GHz), uniform arrays (i.e ULA and UCA) can be selected for validation purposes. However for a practical wideband system non-uniform arrays should be considered. Following on section 5.2.1 the following scenarios are to be considered:

1. Three Ettus B210 SDRs with an Octoclock: use a UCA with a radius equal to a half-wavelength of the centre frequency of the operational band.
2. Three Ettus B210 SDRs with an Octoclock: use stochastic element spacing normalised to a half-wavelength of the centre frequency of the operational band.

© University of Pretoria

3. A Per Vices Crimson SDR: for system validation use a ULA.
4. A Per Vices Crimson SDR: for a operational system use a logarithmically-spaced linear array.

5.2.3 Sensor type

The sensor used, determines the size and mountability of an array. Here are some popular choices of sensors that can be used for DF:

1. **Dipole antennas**: these antennas are cheap to manufacture and are omnidirectional. The problem however is that they are mounted at the vertical centre of the antenna, thus they are suitable to be mounted on a mast or on the side of buildings but not on horizontal planar surfaces. For DF such an array should be mounted around a mast, making it often impractical to use.
2. **Monopole antennas**: similar to dipoles, however they are mounted on a plane. These antennas are suitable for planer mounting such as on the roof of a vehicle or bottom of an aeroplane. The vertical coverage is not as optimal as in comparison to a dipole antenna.
3. **Patch antenna**: these antennas are etched on a substrate, hence they can be manufactured through a similar process used for electronic circuitry. These antennas can easily be mounted against surfaces, such as the side of a plane or vehicle. As patch antennas are flat they have aerodynamic benefits to vehicles. Patch antennas are directional hence they have increase antenna gain.
4. **Spiral antennas**: Large bandwidth, small size, directional antennas typically used for radar warning receivers (RWRs).
5. **Parabolic dish antennas**: popular use in radio-astronomy due to high gain, wide bandwidth and large directivity.

For practical land-based systems and for system validation, monopole antennas are selected as they are easy to mount, omnidirectional and relatively cheap. ULAs antenna configurations can use monopole antennas for laboratory testing, as the 180° error can be mitigated and interference from sources outside the FOV are minimal. For practical ULA based systems, patch antennas can be used due to directivity, easy to mount on surfaces and low cost.

© University of Pretoria

5.3 RECEIVER ARCHITECTURE AND DF ALGORITHM SELECTION

The optimisation in section 4.3.5 has shown that the optimal receiver in terms of processing versus DOA accuracy is the Basic-FFT. This is mostly attributed to the low processing requirements. It should however be realised that often sub 10° RMSE values are not achieved (depending on the scenario and DF algorithm), hence this receiver for DOA estimation is strictly not classified as super-resolution.

Channeliser based receivers achieved considerable better results. However, in different scenarios the receiver architectures and windows displayed slightly different performances, resulting in different receivers being optimal in each scenario. Ultimately this slight variance within the results of these receivers caused the receivers not to be on Pareto front regularly. It can therefore be suggested that certain receivers are optimal in certain scenarios.

The FD-Root-MuSiC algorithm proved optimal for UCAs when optimising RMSE performance above processing efficiency. The FD-Linesearch-MuSiC algorithm proved optimal for UCAs when optimising processing above RMSE performance. The FD-Root-MuSiC algorithm typically takes 39% longer to execute than FD-Linesearch-MuSiC algorithm, however it has a RMSE improvement of 1 to 4 orders of magnitude (depending on the selected SNR) (Table 4.3). Given this trade-off, the FD-Root-MuSiC algorithm is selected to be superior for UCA based arrays.

The Root-MuSiC algorithm has been proven optimal for all ULA arrays (Table 4.4).

The WLS based algorithms provided great performance, however the performance increase is negligibly small for the given increase of processing required for the algorithms. These algorithms are therefore not feasible. The MuSiC and Root-Search-MuSiC algorithms are processing inefficient and are therefore also not feasible.

The following five receivers in conjunction with DF algorithms are regularly found on the Pareto line and are therefore considered Pareto efficient and consequently optimal:

- Basic-FFT with a rectangular or Gaussian window and the Root-MuSiC algorithm: processing efficient with fair RMSE values, only applicable for ULAs;

© University of Pretoria

- Basic-FFT with a rectangular window and the FD-Root-MuSiC algorithm: processing efficient with fair RMSE values, only applicable for UCAs;
- Channeliser receiver using a DFT for the secondary stage with both windows being rectangular and using the Root-MuSiC algorithm: increased processing with excellent RMSE values, only applicable for ULAs;
- Channeliser receiver using a DFT for the secondary stage with both windows being rectangular and using the FD-Root-MuSiC algorithm: increased processing with excellent RMSE values, only applicable for ULAs;
- Channeliser receiver using a NB-BPF and ACM integration for the secondary stage with both windows being rectangular and using the FD-Root-MuSiC algorithm: high processing with excellent RMSE values, only applicable for ULAs;

To select the most suitable receiver for a given application, consider the available processing power of the selected platform. Select the receiver architecture to be the best performing receiver on the list above, which is not limited by the platforms processing capabilities.

The OFDM based signal with 12-carrier RB structure achieved the best results for RB-ACM integration. This post-integration method allows a data-rate reduction of factor 12 before DOA estimation, hence less resources are required for DOA estimation. This post-integration method therefore both improves accuracy and performance.

5.4 CONCLUSION

This section discussed the design of a NNC-DF system given the simulation results and taking practical limitations in account.

It was discussed that the biggest practical limitation is the receiver, as it is a trade-off between dynamic range, bandwidth, number of channels, clock - and phase stability, and cost. Therefore this should be the starting point of the design.

Sensors (antennas) and the applicable array used, should be selected according to the application. For validation of algorithms and receivers, uniform based antennas with monopole antennas are sufficient, however this is impractical for an operational system.

© University of Pretoria

The receiver architecture and algorithms are dependent on the platform (receiver), the sensor array, and the available processing. As the architecture and algorithms are generally implemented in the software of firmware, they are observed fairly late in the system design.

© University of Pretoria

© University of Pretoria

CHAPTER 6

CONCLUSION

6.1 CHAPTER OVERVIEW

This chapter discusses the outcomes of the research and draws conclusions based on the results.

6.2 SUMMARY OF THE WORK DONE

In this dissertation the following work was done:

- a mathematical analysis proving that OFDM signals are only orthogonal for a synchronised system (section 3.2),
- a scenario analysis for a NNC system to emphase the issues of timing delay power differences (section 3.3),
- simulations done on AOA estimation that investigate the number of elements, the antenna array configuration, the receiver architecture, the effects of windowing on the data, integration methods in receiver design, the DF algorithms and the effects of different channels for a LTE based signal (chapter 4),
- optimisation of the simulations parameters for better receiver design (section 4.3.5),
- practical system design based upon the simulation results (chapter 5) that incorporate practical limitations (section 3.6).

© University of Pretoria

6.3 SUMMARY OF THE RESULTS

The simulations investigated the number of elements, the antenna array configuration, the receiver architecture, the effects of windowing on the data, integration methods in receiver design, the DF algorithms and the effects of different channels for a LTE based signal. The two received signals for the simulation were assumed to be unsynchronised, from different sources, and to be in adjacent FDMA channels.

From the simulation results the following conclusions were made:

- the increase of antenna elements tend to improve the RMSE, however there are exceptions that displayed inferior performance which are caused by array ambiguities,
- ULAs are less complex with regard to simulation and application of AOA estimation algorithms, as a FFT can be used to relate the antenna positions to the beam-pattern of the array,
- signals from different sources with almost no frequency separation are the most difficult to estimate due to ICI,
- increasing signal isolation provides improved results for signals with interference,
- exploitation of the RB structure of LTE can be used to improve parameter estimation in the frequency domain,
- RB-ACM integration is the most effective integration technique as it reduces the number of AOA estimations required and improves the estimation by accurately obtaining a ACM,
- receiver architectures with great signal isolation and integration techniques tend to have improved results, however the associated processing involved proved inefficient,
- receivers architectures with great signal isolation only show improvement above basic receivers with the presence of interference,
- windowing only showed some benefits in channels that contain frequency dispersion or for signals with large frequency separation.

The following conclusions where made by analysing the simulation results through optimisation techniques, where the processing time and system performance are selected as the optimisation objectives:

© University of Pretoria

- the receiver selection proved to have a larger influence than the DOA algorithm in system design,
- channeliser receivers have great performance but at great processing cost resulting in inefficiency throughout many cases
- the WLS-based algorithms are not optimal despite the good performance,
- the Root-MuSiC is the most efficient algorithm for ULAs,
- the FD-based MuSiC algorithms are the most efficient algorithms for UCAs,
- windowing has very low impact on the system and in most cases the rectangular window (i.e. no windowing) was proven optimal,
- RB-ACM integration is the most effective integration technique in all receivers.

6.4 RESEARCH OUTCOMES

There is limited research on NNC-based DOA estimation techniques which are focused on cellular communication signals, and this dissertation has discussed both the theoretical and practical design of applicable systems. The research has adapted and optimised standard estimation techniques and receiver design to be applicable to NNC-DF systems. NNC based operations are considerably more difficult than network coherent operations, as the sensor environment is not optimally configured for the receiver, and therefore it opens a research field with a different set of challenges.

The research has proven that with correct receiver design and by taking advantage of the signal properties (such as the RB structure), DF can be done for NNC systems, despite interference. An angular resolution of sub-10° is regularly achieved, and in some cases even sub-1° could be achieved in the presence of interference. The AOA accuracy is dependant on the SNR and the degree of interference to the signal, as well as practical limitations, such as measurement precision and dynamic range proved to be further restricting factors for estimation.

Various DF algorithms, receiver architectures, signal isolation techniques, and integration methods have been evaluated, and through optimisation techniques the optimal algorithms and receivers for the application has been identified. For example, it was shown that RB-ACM integration has superior results in terms of post integration techniques, but this technique is

© University of Pretoria

only applicable if the bandwidth of the signal is known (in this case it is limited by the RB as specified in the LTE specification).

Various DF receiver parameters have been simulated, compared and conclusions have been drawn for optimal design as well as identifying the associated advantages and disadvantages for the parameter selection. The parameters include the selection of the sensor array, the receiver and processing of the system. The simulation have shown that despite the loss of orthogonality of OFDM for NNC systems, AOA estimation can still be achieved despite the presence of interference. By exploiting the OFDM based signal properties some estimation improvement was achieved.

6.5 LITERARY CONTRIBUTION

NNC-DF on LTE signals have applications in emergency, security and monitoring services, without the required cooperation or network infrastructure of the cellular network operators. Therefore, for quick reaction tasks, where reaction time is directly proportional to loss, such systems can be proven beneficial.

This research allows a more practical approach to the design of NNC systems. As processing methods are directly compared, many popular DF techniques that are used in isolation in literature have been evaluated to determine whether they are applicable to operational DF systems.

6.6 RECOMMENDATIONS FOR FUTURE WORK

The work was theoretically based and only applied to simulations. However for validation, a practical experiment is required to prove the accuracy of the simulation. It should be noted that due to the range and number of simulation parameters incorporated, a vast number of permutations exist (exactly why optimisation was used to find possible best receivers), therefore experimental evaluation of each permutation is impractical. The optimal receivers, which displayed regularly on the Pareto front, should be selected for experimental evaluation.

Angular multipath was not incorporated in the simulations due to a great increase of channel simulation complexity. For future research, angular multipath should be incorporated to

© University of Pretoria

obtain a more accurate representation of a received signal in a realistic operating environment.

6.7 CONCLUDING STATEMENTS

The design and simulation of a NNC-DF system for LTE which incorporates practical considerations has been addressed in this dissertation. The work done would greatly simplify the development for an operational system.

© University of Pretoria

© University of Pretoria

REFERENCES

[1] Z. D. Boren. (2014, Oct.) There are officially more mobile devices than people in the world. The Independent. [Online]. Available: http://www.independent.co.uk/life-style/gadgets-and-tech/news/there-are-officially-more-mobile-devices-than-people-in-the-world-9780518.html

[2] T. E. Tuncer and B. Friedlander, *Classical and Modern Direction-of-Arrival Estimation.* Burlington: Elsevier, 2009.

[3] E. Auchard. (2015, Mar.) Nokia, NTT DoCoMo prepare for 5G ahead of Tokyo Olympics launch. Reuters. [Online]. Available: http://www.reuters.com/article/2015/03/02/us-telecoms-mwc-ntt-docomo-idUSKBN0LY0FD20150302

[4] S. J. Orfanidis, *Electromagnetic Waves and Antennas.* Rutgers University, 2008.

[5] S. M. Kay, *Modern Spectral Estimation: Theory and Application*, ser. Prentice-Hall Signal processing series. Prentice Hall, 1999.

[6] G. Bartoli, R. Fantacci, D. Marabissi, and M. Pucci, "LTE-A femto-cell interference mitigation with MuSiC DOA estimation and null steering in an actual indoor environment," in *2013 IEEE International Conference on Communications (ICC)*, June 2013, pp. 2707–2711.

[7] D. Kundu, "Modified MUSIC algorithm for estimating DOA of signals," *Signal Processing*, vol. 48, no. 1, pp. 85 – 90, 1996.

[8] H. Abeida and J.-P. Delmas, "Statistical Performance of MUSIC-Like Algorithms in Resolving Noncircular Sources," *IEEE Transactions on Signal Processing*, vol. 56, no. 9,

© University of Pretoria

pp. 4317–4329, Sept. 2008.

[9] O. A. Oumar, M. F. Siyau, and T. P. Sattar, "Comparison between MUSIC and ESPRIT direction of arrival estimation algorithms for wireless communication systems," in *International Conference on Future Generation Communication Technology (FGCT)*, Dec. 2012, pp. 99–103.

[10] M. L. Bencheikh and Y. Wang, "Joint DOD-DOA estimation using combined ESPRIT-MUSIC approach in MIMO radar," *Electronics Letters*, vol. 46, no. 15, pp. 1081–1083, July 2010.

[11] W. A. Gardner, "Simplification of MUSIC and ESPRIT by exploitation of cyclostationarity," *Proceedings of the IEEE*, vol. 76, no. 7, pp. 845–847, July 1988.

[12] Y. L. Sit, M. Agatonovic, and T. Zwick, "Neural network based direction of arrival estimation for a MIMO OFDM radar," in *9th European Radar Conference (EuRAD)*, Oct. 2012, pp. 298–301.

[13] A. Gaber and A. Omar, "Sub-nanosecond accuracy of TDOA estimation using Matrix Pencil algorithms and IEEE 802.11," in *International Symposium on Wireless Communication Systems (ISWCS)*, Aug. 2012, pp. 646–650.

[14] A. Gaber and A. Omar, "A study of TDOA estimation using Matrix Pencil algorithms and IEEE 802.11ac," in *Ubiquitous Positioning, Indoor Navigation, and Location Based Service (UPINLBS)*, Oct. 2012, pp. 1–8.

[15] M. F. Khan and M. Tufail, "Beamspace matrix pencil method for direction of arrival estimation," *Institute of Electronics, Information and Communication Enegineers (IEICE) Electronics Express*, vol. 6, no. 16, pp. 1168–1173, 2009.

[16] T. K. Sarkar and O. Pereira, "Using the matrix pencil method to estimate the parameters of a sum of complex exponentials," *IEEE Antennas and Propagation Magazine*, vol. 37, no. 1, pp. 48–55, Feb. 1995.

[17] J. Capon, "High-resolution frequency-wavenumber spectrum analysis," *Proceedings of the IEEE*, vol. 57, no. 8, pp. 1408–1418, Aug. 1969.

© University of Pretoria

[18] F. T. Ulaby, E. Michielssen, and U. Ravaioli, *Fundamentals of Applied Electromagnetics*. Pearson Education, Limited, 2014.

[19] A. Kaur and A. Singh, “Comparison Between the Radiation pattern of Uniform Circular Array and Uniform Planar Array,” *International Journal of Computer Networks and Wireless Communications (IJCNWC)*, vol. 2, no. 2, pp. 191 – 193, Apr. 2012.

[20] *TS 36.211 Evolved Universal Terrestrial Radio Access (E-UTRA); Physical channels and modulation*, 3rd Generation Partnership Project Std. 36.211, Rev. Release 12.4.0, Jan. 2015.

[21] S. M. Kay, *Fundamentals of Statistical Signal Processing: Estimation Theory*, ser. Prentice-Hall Signal processing series. Prentice Hall, 1993, vol. 1.

[22] W. J. Bangs, “Array processing with generalized beamformers,” Ph.D. dissertation, Yale University, 1971.

[23] G. Bienvenu and L. Kopp, “Adaptivity to background noise spatial coherence for high resolution passive methods,” in *IEEE International Conference on Acoustics, Speech, and Signal Processing (ICASSP)*, vol. 5, Apr. 1980, pp. 307–310.

[24] Z. Liu and G. Liao, “Detection of the number of signal sources utilizing MUSIC spectrum uniformity,” in *Signal Processing, Communications and Computing (ICSPCC), 2011 IEEE International Conference on*, Sept 2011, pp. 1–4.

[25] F. Li, H. Liu, and R. Vaccaro, “Performance analysis for doa estimation algorithms: unification, simplification, and observations,” *Aerospace and Electronic Systems, IEEE Transactions on*, vol. 29, no. 4, pp. 1170–1184, Oct 1993.

[26] R. Schmidt, “Multiple emitter location and signal parameter estimation,” *Antennas and Propagation, IEEE Transactions on*, vol. 34, no. 3, pp. 276–280, Mar 1986.

[27] J. Stone, “Blind source separation using temporal predictability,” *Neural Computation*, vol. 13, no. 7, pp. 1559–1574, July 2001.

[28] K. Lee, Y. Bresler, and M. Junge, “Subspace methods for joint sparse recovery,” *Inform-*

© University of Pretoria

ation Theory, IEEE Transactions on, vol. 58, no. 6, pp. 3613–3641, June 2012.

[29] A. Barabell, "Improving the resolution performance of eigenstructure-based direction-finding algorithms," in *IEEE International Conference on Acoustics, Speech, and Signal Processing (ICASSP)*, vol. 8, Apr. 1983, pp. 336–339.

[30] B. D. Rao and K. V. S. Hari, "Performance analysis of Root-Music," *IEEE Transactions on Acoustics, Speech and Signal Processing*, vol. 37, no. 12, pp. 1939–1949, Dec. 1989.

[31] M. A. Doron and E. Doron, "Wavefield modeling and array processing I. Spatial sampling," *IEEE Transactions on Signal Processing*, vol. 42, no. 10, pp. 2549–2559, Oct. 1994.

[32] M. A. Doron and E. Doron, "Wavefield modeling and array processing II. Algorithms," *IEEE Transactions on Signal Processing*, vol. 42, no. 10, pp. 2560–2570, Oct. 1994.

[33] M. A. Doron and E. Doron, "Wavefield modeling and array processing III. Resolution capacity," *IEEE Transactions on Signal Processing*, vol. 42, no. 10, pp. 2571–2580, Oct. 1994.

[34] C. P. Mathews and M. D. Zoltowski, "Eigenstructure techniques for 2-D angle estimation with uniform circular arrays," *IEEE Transactions on Signal Processing*, vol. 42, no. 9, pp. 2395–2407, Sept. 1994.

[35] R. Goossens, H. Rogier, and S. Werbrouck, "UCA Root-MUSIC With Sparse Uniform Circular Arrays," *IEEE Transactions on Signal Processing*, vol. 56, no. 8, pp. 4095–4099, Aug. 2008.

[36] M. Rubsamen and A. B. Gershman, "Direction-of-Arrival Estimation for Nonuniform Sensor Arrays: From Manifold Separation to Fourier Domain MUSIC Methods," *IEEE Transactions on Signal Processing*, vol. 57, no. 2, pp. 588–599, Feb. 2009.

[37] S. M. Kay, *Fundamentals of Statistical Signal Processing: Detection Theory*, ser. Prentice-Hall Signal processing series. Prentice Hall, 1998, vol. 2.

[38] T. S. Rappaport, *Wireless Communications: Principles and Practice*, ser. Electrical

© University of Pretoria

engineering. Prentice Hall, 1996.

[39] J. Vlok and J. Olivier, "Non-cooperative detection of weak spread-spectrum signals in additive white gaussian noise," *Communications, IET*, vol. 6, no. 16, pp. 2513–2524, November 2012.

[40] J. Vlok and J. Olivier, "Blind sequence-length estimation of low-snr cyclostationary sequences," *Communications, IET*, vol. 8, no. 9, pp. 1578–1588, June 2014.

[41] E. C. Ifeachor and B. W. Jervis, *Digital Signal Processing: A Practical Approach*, ser. Electronic systems engineering series. Prentice Hall, 2002.

[42] M. Arulampalam, S. Maskell, N. Gordon, and T. Clapp, "A tutorial on particle filters for online nonlinear/non-gaussian bayesian tracking," *Signal Processing, IEEE Transactions on*, vol. 50, no. 2, pp. 174–188, Feb 2002.

[43] R. Mahler, "Multitarget bayes filtering via first-order multitarget moments," *Aerospace and Electronic Systems, IEEE Transactions on*, vol. 39, no. 4, pp. 1152–1178, Oct 2003.

[44] *TS 36.101 Evolved Universal Terrestrial Radio Access (E-UTRA); User Equipment (UE) radio transmission and reception*, 3rd Generation Partnership Project Std. 36.101, Rev. Release 12.6.0, Jan. 2015.

[45] *TS 25.913 V9.0.0 Technical Specification Group Radio Access Networdk; Requirements for Evolved UTRA (E-UTRA) and Evolved Utran (E-Utran)*, 3rd Generation Partnership Project Std. 25.913, Rev. Release 9, Jan. 2009.

[46] T. Nakamura and S. Abeta, "Super 3G Technology Trends - Part 1: Super 3G Overview and Standardazation Activities," *NTT DoCoMo Technical Journal*, vol. 8, no. 2, pp. 52 – 56, Sept. 2006.

[47] S. Johnson and T. Virki. (2009, Dec.) UPDATE 1-TeliaSonera launches world's first LTE services. Reuters. [Online]. Available: http://fr.reuters.com/article/idUKLDE5BD1NK20091214

[48] T. Motsoeneng. (14, July) S.Africa's MTN launches trial of faster LTE network.

© University of Pretoria

Reuters. Johannesburg. [Online]. Available: http://www.reuters.com/article/2011/07/14/idUSL6E7IE1LV20110714

[49] *TS 36.201 Evolved Universal Terrestrial Radio Access (E-UTRA); LTE physical layer; General description*, 3rd Generation Partnership Project Std. 36.201, Rev. Release 12.1.0, Jan. 2015.

[50] *TS 36.212 Evolved Universal Terrestrial Radio Access (E-UTRA); Multiplexing and channel coding*, 3rd Generation Partnership Project Std. 36.212, Rev. Release 12.3.0, Jan. 2015.

[51] *TS 36.104 Evolved Universal Terrestrial Radio Access (E-UTRA); Base Station (BS) radio transmission and reception*, 3rd Generation Partnership Project Std. 36.104, Rev. Release 12.6.0, Dec. 2014.

[52] R. Pec and Y. S. Cho, "A parameter estimation technique for an LTE-based mobile relay station with antenna array," in *International Conference on Information and Communications Technology Convergence (ICTC)*, Oct. 2013, pp. 134–135.

[53] *Recommendation ITU-R M. 1225 Guidelines for evaluation of radio transmission technologies for IMT-2000*, International Telecommunications Union Std. M. 1225, 1997.

[54] *TS 136.101 V11.6.0 LTE; Evolved Universal Terrestrial Radio Access (E-UTRA); User Equipment (UE) radio transmission and reception*, 3rd Generation Partnership Project Std. TS 136.101, 2013.

[55] *TS 137.976 V11.0.0 Universal Mobile Telecommunications (UMTS); LTE; Measurement of radiated performance for Multiple Input Multiple Output (MIMO) and multi-antenna reception for High Speed Packet Access (HSPA) and LTE terminals*, 3rd Generation Partnership Project Std. TS 137.976, 2012.

[56] *TS 36.116 Evolved Universal Terrestrial Radio Access (E-UTRA); Relay radio transmission and reception*, 3rd Generation Partnership Project Std. 36.116, Rev. Release 12.0.0, Jan. 2015.

[57] *TS 125.996 V7.0.0 Universal Mobile Telecommunications System (UMTS); Spacial chan-*

© University of Pretoria

nel model for Multiple Input Multiple Output (MIMO) simulations, 3rd Generation Partnership Project Std. TS 125.996, 2007.

[58] *TS 36.873 Technical Specification Group Radio Access Network; Study on 3D channel model for LTE*, 3rd Generation Partnership Project Std. 36.873, Rev. Release 12.0.0, Sept. 2014.

[59] X. Gandibleux, *Metaheuristics for Multiobjective Optimisation.* Springer, 2004.

[60] D. Jones and M. Tamiz, *Practical Goal Programming.* Springer, 2010.

[61] B. P. Lathi and Z. Ding, *Modern Digital and Analog Communication Systems*, ser. Oxford series in electrical and computer engineering. Oxford University Press, 2010.

[62] T. Killian. (2013, Aug.) SDR Showdown: HackRF vs. bladeRF vs. USRP. http://www.taylorkillian.com. [Online]. Available: http://www.taylorkillian.com/2013/08/sdr-showdown-hackrf-vs-bladerf-vs-usrp.html

[63] C. Laufer. (2014, Aug.) Roundup of Software Defined Radios. rtl-sdr. rtl-sdr.com. [Online]. Available: http://www.rtl-sdr.com/roundup-software-defined-radios/

[64] M. Cheffena and L. E. Braten, "Low-Cost Digital Beacon Receiver Based on Software-Defined Radio," *IEEE Antennas and Propagation Magazine*, vol. 53, no. 1, pp. 50 – 55, Feb. 2011.

[65] J. R. Humphries and D. C. Malocha, "Software defined radio for passive sensor interrogation," in *European Frequency and Time Forum International Frequency Control Symposium (EFTF/IFC), 2013 Joint*, July 2013, pp. 270–273.

[66] Z. Yan, Z. Ma, H. Cao, G. Li, and W. Wang, "Spectrum Sensing, Access and Coexistence Testbed for Cognitive Radio using USRP," in *Circuits and Systems for Communications, 2008. ICCSC 2008. 4th IEEE International Conference on*, May 2008, pp. 270–274.

[67] P. Tamburello and L. Mili, "New Robust Estimators of Correlation and Weighted Basis Pursuit," *IEEE Transactions on Signal Processing*, vol. 63, no. 4, pp. 882–894, Feb. 2015.

[68] G. Berardinelli, J. L. Buthler, F. M. Tavares, O. Tonelli, D. A. Wassie, F. Hakhamaneshi,

© University of Pretoria

T. B. Sorensen, and P. Mogensen, “Distributed Synchronization of a testbed network with USRP N200 radio boards,” in *Signals, Systems and Computers, 2014 48th Asilomar Conference on*, Nov. 2014, pp. 563–567.

[69] G. Berardinelli, P. Zetterberg, O. Tonelli, A. Cattoni, T. B. Sorensen, and P. Mogensen, “An SDR architecture for OFDM transmission over USRP2 boards,” in *Signals, Systems and Computers (ASILOMAR), 2011 Conference Record of the Forty Fifth Asilomar Conference on*, Nov. 2011, pp. 965–969.

[70] S. Chantaraskul and K. Moessner, “Implementation of a genetic algorithm-based decision making framework for opportunistic radio,” *IET Communications*, vol. 4, no. 5, pp. 495–506, Mar. 2010.

[71] H. Shahid and Y.-D. Yao, “Algorithm and experimentation of frequency hopping, band hopping, and transmission band selection using a cognitive radio test bed,” in *Wireless and Optical Communication Conference (WOCC), 2014 23rd*, May. 2014, pp. 1–5.

[72] A. A. Tabassam, M. U. Suleman, S. Khan, and S. H. R. Tirmazi, “Spectrum estimation and spectrum hole opportunities prediction for cognitive radios using higher-order statistics,” in *Wireless Advanced (WiAd), 2011*, June 2011, pp. 213–217.

[73] V. Barral, J. Rodas, J. Garcia-Naya, and C. J. Escudero, “A novel, scalable and distributed software architecture for software-defined radio with remote interaction,” in *Systems, Signals and Image Processing (IWSSIP), 2012 19th International Conference on*, Apr. 2012, pp. 80–83.

[74] R. Linhart and P. Fiala, “Measuring RF circuits response using software defined radio system,” in *Applied Electronics (AE), 2014 International Conference on*, Sept. 2014, pp. 185–188.

[75] Wireless Design & Development (WDD). (2014, Sept.) Per Vices’ Crimson Full Duplex Transceiver. Wireless Design & Development. http://www.wirelessdesignmag.com/. [Online]. Available: http://www.wirelessdesignmag.com/product-releases/2014/09/vices-crimson-full-duplex-transceiver

[76] B. Malatest. (2014, Oct.) Per Vices’ Crimson: SDR With

© University of Pretoria

20Gbps Backhaul. Nasdaq. http://globenewswire.com/. [Online]. Available: http://globenewswire.com/news-release/2014/10/15/673506/10102813/en/Per-Vices-Crimson-SDR-With-20Gbps-Backhaul.html

[77] National Instruments. (2015) NI FlexRIO. National Isntruments. [Online]. Available: http://www.ni.com/flexrio/

[78] E. Martinez. (2011, May) Ni expands fpga-enabled ni flexrio family for pxi with six new i/o modules. National Instruments. thomasnet.com. [Online]. Available: http://news.thomasnet.com/companystory/ni-expands-fpga-enabled-ni-flexrio-family-for-pxi-with-six-new-i-o-modules-847424

[79] E. Johnson and A. Brown. (2013, Mar.) Software-designed instrumentation redefines test. Evaluation Engineering. http://www.evaluationengineering.com/. [Online]. Available: http://www.evaluationengineering.com/articles/201303/software-designed-instrumentation-redefines-test.php

© University of Pretoria

© University of Pretoria

APPENDIX A

PARETO OPTIMISATION EXAMPLE

A.1 INTRODUCTION

This section provides an extended tutorial with Pareto optimisation.

A.2 BASE PROBLEM AND SYSTEM RULES

Pareto optimisation considers a system with multiple outcomes which needs to be optimised. Firstly it requires the system to be defined (section A.2.2), followed by the evaluation of the outcomes of the system. Lastly the system inputs that results in optimal outcomes of the system should be identified and used.

A.2.1 The problem

Two people Alex and Ben (denoted by A and B respectively) are hungry and are presented with a bowl of fruit containing apples (α), bananas (β), grapefruit (γ), and dates (δ). Each individual has a preference to certain fruit and therefore enjoy some fruit more than others. The aim of the optimisation is to divide to fruit such that both A and B receive maximum satisfaction from the fruit.

A.2.2 The system description

The bowl of fruit consists of a finite number of each fruit:

- Three apples, i.e. $N(\alpha) = 3$

© University of Pretoria

- Two bananas, i.e. $N(\beta) = 2$
- One grapefruit, i.e. $N(\gamma) = 1$
- Two dates, i.e. $N(\delta) = 2$

Therefore a total of eight fruit are in the bowl. Each person must receive a minimum of one fruit (i.e $\min\left[N(A\{\cdots\})\right] = \min\left[N(B\{\cdots\})\right] = 1$), and a maximum of three fruit (i.e $\max\left[N(A\{\cdots\})\right] = \max\left[N(B\{\cdots\})\right] = 3$). Therefore 27 different fruit allocations exist for each user. As an example, the possible allocations for A are listed:

$$\begin{array}{cccccc}
A\{\alpha\} & A\{\beta\} & A\{\gamma\} & A\{\delta\} & A\{\alpha,\alpha\} & A\{\alpha,\beta\} \\
A\{\alpha,\gamma\} & A\{\alpha,\delta\} & A\{\beta,\beta\} & A\{\beta,\gamma\} & A\{\beta,\delta\} & A\{\gamma,\delta\} \\
A\{\delta,\delta\} & A\{\alpha,\alpha,\alpha\} & A\{\alpha,\alpha,\beta\} & A\{\alpha,\alpha,\gamma\} & A\{\alpha,\alpha,\delta\} & A\{\alpha,\beta,\beta\} \\
A\{\alpha,\beta,\gamma\} & A\{\alpha,\beta,\delta\} & A\{\alpha,\gamma,\delta\} & A\{\alpha,\delta,\delta\} & A\{\beta,\beta,\gamma\} & A\{\beta,\beta,\delta\} \\
A\{\beta,\gamma,\delta\} & A\{\beta,\delta,\delta\} & A\{\gamma,\delta,\delta\} & & &
\end{array}$$

As the quantity of fruit (resources) are finite, a total of 438 valid fruit allocations exists for the two individuals.

The two outcomes of the system can be described as the satisfaction of Alex (i.e. $O(A\{\cdots\})$) and the satisfaction of Ben (i.e. $O(B\{\cdots\})$). The general rule is that the satisfaction of multiple fruit are the sum of each individual fruit, for example:

$$O(A\{\alpha,\beta\}) = O(A\{\alpha\}) + O(A\{\beta\}) \tag{A.1}$$

Alex (A) has the following preferences and associated satisfaction:

1. Alex receives great satisfaction from apples, $O(A\{\alpha\}) = 5$.
2. Alex cannot consume more than one apple without feeling nauseous, $O(A\{\alpha,\alpha,\cdot\}) = -2$.
3. Alex is allergic to bananas, $O(A\{\beta\}) = -1$.
4. Alex is indifferent to grapefruit and dates, $O(A\{\gamma\}) = O(A\{\delta\}) = 1$.

© University of Pretoria

Ben(B) has the following preferences and associated satisfaction:

1. Ben prefers apples, $O(B\{\alpha\}) = 2$.
2. Ben is indifferent to all other fruits, $O(B\{\beta\}) = O(B\{\gamma\}) = O(B\{\delta\}) = 1$.
3. Ben has brumotactillophobia (fear of mixing food), therefore his satisfaction reduces by 1 for each different fruit, for example $O(B\{\alpha, \beta\}) = O(B\{\alpha\}) + O(B\{\beta\}) - 1$

A final rule rule of the system is that Alex and Ben are in direct competition, therefore if one of them have more fruit, the other has reduced satisfaction:

$$\text{if } N(A\{\cdots\}) > N(B\{\cdots\}),$$

$$\text{then } O_{ef}(B\{\cdots\}) = O(B\{\cdots\}) - (N(A\{\cdots\}) - N(B\{\cdots\}))$$

A.3 BASIC ANALYSIS CONCEPTS

First of all, the desired output is that the maximum satisfaction should be achieved for each individual. Therefore each resource allocation should be compared, with the emphasis being, to find the maximum achievable satisfaction.

The system has been thoroughly defined, now the question remains, how do we allocate the resources (fruit) to the two individuals (system) to obtain the optimal outcomes (satisfaction)?

A.3.1 Pareto efficiency

To explain Pareto efficiency, a single resource allocation is selected and evaluated. Let us select the following resource allocation:

$$(A\{\alpha, \delta\}, B\{\alpha, \gamma\}), \tag{A.2}$$

where the outcomes form a point P:

$$P = (O(A\{\alpha, \delta\}), O(B\{\alpha, \gamma\})) = (6, 2) \tag{A.3}$$

The Pareto efficiency of the allocation should now be determined. A solution set (resource allocation) is Pareto efficient if any outcome can be improved without worsening any other.

© University of Pretoria

Therefore a single improvement of the outcome should be found such that the allocation can be classified as Pareto inefficient. An exhaustive search of all the possible allocations should therefore be made.

An option to improve the outcome $O(B\{\cdots\})$ is to add another apple (α), to form a new output of $O_n(B\{\alpha, \alpha, \gamma\}) = 4$. This shows that the output has improved for B, however $O_n\left(A\{\alpha, \delta\}\right)$ has decreased to 5. Therefore as a whole the new point $N = (5, 4)$ has not improved all outcomes. Based on this improvement it seems as if the point P is Pareto efficient, however all possible improvements should be evaluated to confirm whether point P is Pareto efficient or not.

Follow the same steps by improving the outcome $O(B\{\cdots\})$ by adding another apple (α), but additionally improve the outcome $O(A\{\cdots\})$ by adding another date (δ). The new outcomes forms a point M:

$$M = \left(O_m\left(A\{\alpha, \delta, \delta\}\right), O_m\left(B\{\alpha, \alpha, \gamma\}\right)\right) = (7, 4) \tag{A.4}$$

Point M improves all outcomes of point P, therefore **P is Pareto inefficient**. Further, point M improves outcome $O(A\{\cdots\})$ whilst outcome $O(B\{\cdots\})$ remains the same when compared to point N, therefore **point N is also Pareto inefficient**.

Lastly, the Pareto efficiency of point M should be determined. Outcome A, is already at the maximum possible value it can achieve of $5 + 1 + 1 = 7$. Outcome B can be improved if and only if the grapefruit (γ) is substituted with an apple (the diversity penalty is then removed and Ben prefers apples) to obtain a satisfaction level of 6, but the third apple is already allocated to A. As $O(A\{\cdots\})$ is at the maximum possible and $O(B\{\cdots\})$ cannot be improved without reallocating all resources (i.e. worsening output A), it is concluded that **point M is Pareto efficient**.

The three points P, N and M are shown in Figure A.1. The analysis steps from point P to M are also presented.

A graphical analysis method of Pareto efficiency is to observe the location of each point relative to all other points. In the case where both system outcomes should be maximised, a point is Pareto efficient if no points exists that is larger in any aspect. Consider a point P as its own axis, if there are other points located in its first quadrant, then point P is Pareto

© University of Pretoria

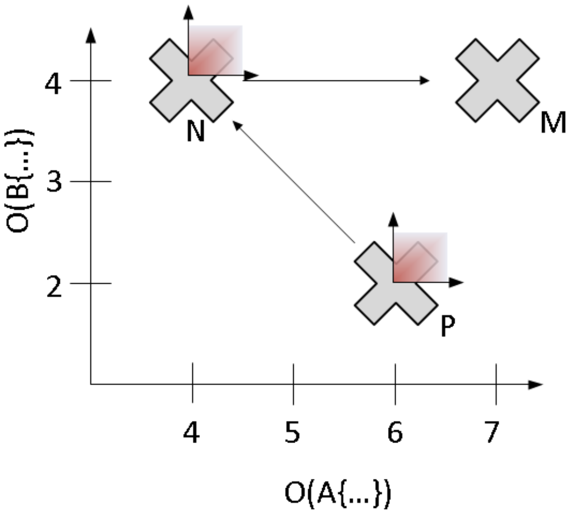

Figure A.1: Graphical representation of system outcomes.

inefficient. If there are no other points in the relative first quadrant, then point P is Pareto efficient. In Figure A.1 points N and P have other points in their relative first quadrants, this is why a small axis with a red first quadrant is drawn.

The graphical technique is relatively simple to implement. If both outcomes should be minimized, then the relative third quadrant of each point should be selected. The quadrant of selection is therefore dependant on whether an output should be maximised or minimized.

All Pareto inefficient points are sub-optimal, as one of their outcomes can be improved. Once all Pareto efficient points are found on the graph, then they can be used to draw the Pareto front.

A.4 FULL PARETO ANALYSIS

In this example all resource allocation permutations will be considered. This is not always possible as a large number of permutations is processing intense to solve. In practice a subset of the resource allocations is often considered, and then the values on the Pareto front are used to recursively select an improved resource subset.

All the outcomes are shown in Figure A.2. The size of each circle indicates the number of times the specified outcomes have been achieved. The dotted red line combines all the Pareto

© University of Pretoria

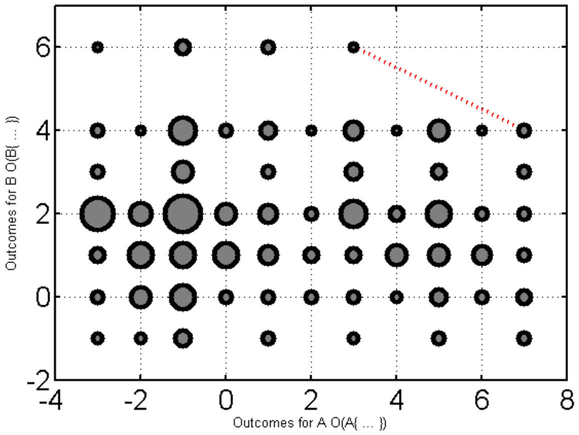

Figure A.2: Graphical representation of system outcomes.

efficient points to form the Pareto front. In this case there are only two points on the Pareto front. The associated resource allocations for all Pareto efficient points is shown in Table FinResults.

Table A.1: Resource allocation for Pareto efficient outcomes.

$A\{\cdots\}$	$B\{\cdots\}$	$O(A\{\cdots\})$	$O(B\{\cdots\})$
γ, δ, δ	α, α, α	3	6
α, γ, δ	α, α, β	7	4
α, γ, δ	α, α, γ	7	4
α, γ, δ	α, α, δ	7	4
α, δ, δ	α, α, β	7	4
α, δ, δ	α, α, γ	7	4

After the Pareto analysis six different resource allocations have resulted in two optimal outputs of the system. The optimisation does not result in a single value, therefore some degree of freedom exist in selection of the final resource allocation.

Now further factors for resource allocation can be added to select the final output. If I have a deep respect for Ben's phobia, I'll select $A\{\gamma, \gamma, \delta\}$ and $B\{\alpha, \alpha, \alpha\}$, such that I am as accommodating as possible. On the other hand, if the combined satisfaction should be a maximum I'd select one of the other six results.

© University of Pretoria

The same process can be used if more than two outcomes are required to be optimised. However higher dimension graphing is then required to solve the problem graphically.

© University of Pretoria

© University of Pretoria

APPENDIX B

DERIVATION OF THE POWER SPECTRAL DENSITY OF NNC-OFDM SIGNALS

B.1 INTRODUCTION

This section shows the mathematical derivation of the PSD for unsynchronised reception of a OFDM-based communication signal.

B.2 PHASE DISCONTINUITY

A complex-sinusoid is bounded over a period of T_{sym}, and undergoes a random phase change of ϕ_0 at time t_0:

$$x(t) = A \times \Pi\left(\frac{t - \frac{t_0}{2}}{t_0}\right) \times \mathrm{e}^{2\pi \mathrm{j} f_c t} + A \times \Pi\left(\frac{t - \frac{T_{sym}+t_0}{2}}{T_{sym} - t_0}\right) \times \mathrm{e}^{2\pi \mathrm{j} f_c t + j\phi_0}, \tag{B.1}$$

through simplification we obtain:

$$x(t) = A \times \mathrm{e}^{2\pi \mathrm{j} f_c t}\left(\Pi\left(\frac{t - \frac{t_0}{2}}{t_0}\right) + \Pi\left(\frac{t - \frac{T_{sym}+t_0}{2}}{T_{sym} - t_0}\right) \times \mathrm{e}^{\mathrm{j}\phi_0}\right). \tag{B.2}$$

The frequency domain is derived:

$$X(f) = A\delta(f - f_c) * \left[t_0 \mathsf{sinc}\left(ft\right) \mathrm{e}^{\pi \mathrm{j} f t_0} + (T_{sym} - t_0)\mathsf{sinc}\left(f(T_{sym} - t_0)\right) \mathrm{e}^{\pi \mathrm{j} f (T_{sym}+t_0) + \mathrm{j}\phi_0}\right], \tag{B.3}$$

and simplified:

$$X(f) = A\mathrm{e}^{\pi \mathrm{j}(f - f_c)t_0}\left[t_0 \mathsf{sinc}\left((f - f_c)t\right) + (T_{sym} - t_0)\mathsf{sinc}\left((f - f_c)(T_{sym} - t_0)\right) \mathrm{e}^{\pi \mathrm{j}(f - f_c)T_{sym} + \mathrm{j}\phi_0}\right]. \tag{B.4}$$

© University of Pretoria

The function is redefined to be a function of both the frequency and the time-delay of the phase change:

$$X_{eq}(t,f) = X(f)|_{t=t_0}\,. \tag{B.5}$$

Define the time-delay as a random variable with a uniform distribution :

$$p_{t_0}(t) = \begin{cases} \frac{1}{T_{sym}} & 0 \le t \le T_{sym} \\ 0 & otherwise \end{cases}. \tag{B.6}$$

The average spectral power $\overline{X}_t(f)$ over the time-delay is defined:

$$\overline{X}_t(f) = \mathsf{E}\left[|X_{eq}(t,f)|^2\right] = \frac{1}{T_{sym}}\int\limits_0^{T_{sym}} X_{eq}(t,f) \times X^*_{eq}(t,f)dt. \tag{B.7}$$

To solve this equation, the power of the signal is defined:

$$P_x(t,f) = X_{eq}(t,f) \times X^*_{eq}(t,f), \tag{B.8}$$

and solved:

$$\begin{aligned} P_x(t,f) = A^2 \times \Big\{ & t^2 \mathsf{sinc}^2\left(\left(f-f_c\right)t\right) + \left(T-t\right)^2 \mathsf{sinc}^2\left(\left(f-f_c\right)\left(T-t\right)\right) \\ & + 2t\left(T-t\right)\mathsf{sinc}\left(\left(f-f_c\right)t\right) \times \\ & \mathsf{sinc}\left(\left(f-f_c\right)\left(T-t\right)\right)\cos\left(\pi T_{sym}\left(f-f_c\right)+\phi_0\right)\Big\}. \end{aligned} \tag{B.9}$$

To solve the PSD, use the power of the signal $P_x(t,f)$ and *devide et impera*:

$$\overline{X}_{t1}(f)(v) = \int\limits_0^{T_{sym}} t^2 \mathsf{sinc}^2\left(vt\right)dt = \frac{T_{sym}}{2\pi^2 v^2}\left[1 - \mathsf{sinc}\left(2vT_{sym}\right)\right] \tag{B.10}$$

$$\overline{X}_{t2}(v) = \int\limits_0^{T_{sym}} \left(T-t\right)^2 \mathsf{sinc}^2\left(v\left(T-t\right)\right)dt = \frac{T_{sym}}{2\pi^2 v^2}\left[1 - \mathsf{sinc}\left(2vT_{sym}\right)\right] \tag{B.11}$$

$$\therefore \overline{X}_{t2}(v) = \overline{X}_{t1}(v) \tag{B.12}$$

$$\overline{X}_{t3}(v) = \int\limits_0^{T_{sym}} t\left(T-t\right)\mathsf{sinc}\left(vt\right)\mathsf{sinc}\left(v\left(T-t\right)\right)\cos\left(\pi T_{sym}\left(f-f_c\right)+\phi_0\right)dt \tag{B.13}$$

© University of Pretoria

$$\overline{X}_{t3}(v) = \frac{T_{sym}\cos\left(\pi v T_{sym} + \phi_0\right)}{2\pi^2 v^2}\left[\mathsf{sinc}\left(2vT_{sym}\right) - \cos\left(\pi v T_{sym}\right)\right] \tag{B.14}$$

The average spectral power can therefore be determined through substitution:

$$\overline{X}_t(f) = \frac{2A^2}{T_{sym}}\left[\overline{X}_{t1}(v) + \overline{X}_{t3}(v)\right]_{v=f-f_c}, \tag{B.15}$$

and solved:

$$\begin{aligned}\overline{X}_t(f) = \frac{A^2}{T_{sym}}\Big[&1 - \mathsf{sinc}\left(2vT_{sym}\right) + \cos\left(\pi v T_{sym} + \phi_0\right)\mathsf{sinc}\left(vT_{sym}\right)\\ &- \cos\left(\pi v T_{sym} + \phi_0\right)\cos\left(\pi v T_{sym}\right)\Big]_{v=f-f_c}.\end{aligned} \tag{B.16}$$

Define the phase-discontinuity as a random variable with a uniform distribution, independent from $p_{t_o}(t)$:

$$p_\phi(\phi) = \begin{cases} \frac{1}{2\pi} & 0 \leq \phi \leq 2\pi \\ 0 & otherwise \end{cases}. \tag{B.17}$$

Hence the average spectral power over both the time-delay and the phase discontinuity can therefore be defined:

$$\begin{aligned}\overline{X}_{(t,\phi)}(f) &= \mathsf{E}\left[\left|X_{eq}(t,f)\right|^2\right]\\ &= \frac{1}{T_{sym}}\int_{-\infty}^{\infty}\int_{-\infty}^{\infty}\left[X_{eq}(t,f)\times X_{eq}^*(t,f)\right]\times p_{t_0}(t)\times p_\phi(\phi)dtd\phi\\ &= \frac{1}{2\pi}\int_0^{2\pi}\overline{X}_t(f)\Big|_{\phi_0=\phi}d\phi.\end{aligned} \tag{B.18}$$

The average spectral power over both the time-delay and the phase discontinuity is obtained:

$$\overline{X}_{(t,\phi)}(f) = \frac{A^2}{\pi^2 v^2}\left[1 - \mathsf{sinc}\left(2vT_{sym}\right)\right]_{v=f-f_c}. \tag{B.19}$$

The PSD for the observer over both the time-delay and the phase discontinuity is therefore determined:

$$S_{(t,\phi)}(f) = \frac{A^2}{\pi^2 v^2 T_{sym}}\left[1 - \mathsf{sinc}\left(2vT_{sym}\right)\right]_{v=f-f_c}. \tag{B.20}$$

© University of Pretoria

B.3 AMPLITUDE AND PHASE DISCONTINUITY

A signal with a phase and amplitude discontinuity is defined:

$$x_a(t) = A_1 \times \Pi\left(\frac{t-\frac{t_0}{2}}{t_0}\right) \times \mathrm{e}^{2\pi \mathrm{j} f_c t} + A_2 \times \Pi\left(\frac{t-\frac{T_{sym}+t_0}{2}}{T_{sym}-t_0}\right) \times \mathrm{e}^{2\pi \mathrm{j} f_c t}. \tag{B.21}$$

Following the same approach as in the phase discontinuity case, the frequency domain expression can be obtained using the same random variable for the time-delay:

$$X_{eq,a}(t,f) = \mathrm{e}^{\pi \mathrm{j} v t}\left[A_1 t \,\mathsf{sinc}\left(vt\right) + A_2\left(T_{sym}-t\right)\mathsf{sinc}\left(v\left(T_{sym}-t\right)\right)\mathrm{e}^{\pi \mathrm{j} v T_{sym}}\right]\Big|_{v=f-f_c}. \tag{B.22}$$

The average power can be defined:

$$P_{x,a}(t,f) = X_{eq,a}(t,f) \times X^*_{eq,a}(t,f). \tag{B.23}$$

and solved:

$$\begin{aligned} P_{x,a}(t,f) = {} & \left|A_1\right|^2 t^2 \mathsf{sinc}^2\left(\left(f-f_c\right)t\right) + \left|A_2\right|^2\left(T-t\right)^2 \mathsf{sinc}^2\left(\left(f-f_c\right)\left(T-t\right)\right) \\ & + 2\left|A_1\right|\left|A_2\right| t\left(T-t\right)\mathsf{sinc}\left(\left(f-f_c\right)t\right)\mathsf{sinc}\left(\left(f-f_c\right)\left(T-t\right)\right) \times \\ & \cos\left(\pi\left(f-f_c\right)T_{sym} + \angle A_2 - \angle A_1\right). \end{aligned} \tag{B.24}$$

It is assumed that a QAM based modulation scheme is used. The average spectral power can therefore be determined in a similar fashion to the previous case (Section B.2):

$$\overline{X}_{(t,\phi),a}(f) = \frac{A^2_{norm}}{\pi^2 v^2}\left[1-\mathsf{sinc}\left(2vT_{sym}\right)\right]_{v=f-f_c}. \tag{B.25}$$

The PSD for the observer over both the time-delay and the symbol discontinuity is therefore determined:

$$S_{(t,\phi),a}(f) = \frac{A^2_{norm}}{\pi^2 v^2 T_{sym}}\left[1-\mathsf{sinc}\left(2vT_{sym}\right)\right]_{v=f-f_c}. \tag{B.26}$$

B.4 LIMIT OF THE PSD AT THE ORIGIN

The average spectral power is defined as:

$$\overline{X}_{(t,\phi)}(f) = \frac{A^2}{\pi^2 v^2}\left[1-\mathsf{sinc}\left(2vT_{sym}\right)\right]_{v=f-f_c}, \tag{B.27}$$

© University of Pretoria

and the PSD is defined as:

$$S_{(t,\phi)}(f) = \frac{A^2}{\pi^2 v^2 T_{sym}} \left[1 - \mathsf{sinc}\left(2vT_{sym}\right)\right]_{v=f-f_c}. \tag{B.28}$$

The average spectral power of the phase discontinuity is undefined at $f = f_c$. The limit is solved using multiple applications of L'Hopital's rule:

$$\begin{aligned}
\lim_{f\to fc} \overline{X}_{(t,\phi)}(f) &= \lim_{v\to 0} \frac{A^2 - A^2\mathsf{sinc}\left(2vT_{sym}\right)}{\pi^2 v^2} \\
&= \lim_{v\to 0} \frac{-A^2\cos\left(2vT_{sym}\right)}{3\pi^2 v^2} \\
&= \lim_{v\to 0} \frac{A^2 T_{sym}\sin\left(2vT_{sym}\right)}{3\pi v} \\
&= \lim_{v\to 0} \frac{A^2 T_{sym}^2 2\cos\left(2vT_{sym}\right)}{3} \\
&= \frac{2}{3} A^2 T_{sym}^2.
\end{aligned} \tag{B.29}$$

Similarly the PSD can be obtained:

$$\lim_{f\to fc} S_{(t,\phi)}(f) = \frac{2}{3} A^2 T_{sym} \tag{B.30}$$

© University of Pretoria

© University of Pretoria

APPENDIX C

BACKGROUND TO OFDM MATHEMATICS

C.1 INTRODUCTION

This section defines the constellation of QAM and derives the maximum power of a symbol, the average symbol power and the normalised mean power of the constellation.

C.2 QUADRATURE AMPLITUDE MODULATION

This section provides relevant mathematical background to QAM modulation.

For a rectangular M-QAM system, the number of bits B per symbol is a logarithm of base-2, of the constellation size M:

$$B = \log_2 (M) \,. \tag{C.1}$$

In a rectangular QAM system, the symbols are placed in a grid-like fashion within the complex domain with equal spaces between them. As an example the symbols in 16-QAM are a set defined:

$$A_n \in \{\langle \pm 1 \pm i \rangle , \langle \pm 1 \pm 3i \rangle , \langle \pm 3 \pm i \rangle , \langle \pm 3 \pm 3i \rangle\} \,, \tag{C.2}$$

where the imaginary unit i is defined as $i = \sqrt{-1}$. Note that a unit is defined as the smallest distance between the real and/or imaginary axis and the set of points. This is done to ensure

© University of Pretoria

all values in the constellation are integer values in the Cartesian coordinates.

A rectangular QAM scheme has an even number of bits per symbol, and the constellation is symmetric along the x-axis, y-axis, the line $y = x$, the line $y = -x$, and through the point of origin.

The maximum real and imaginary components in the constellation is a function of the the number of bits per symbol:

$$A_{max} = \max_{A} \Re\left\{A_n\right\} = \max_{A} \Im\left\{A_n\right\} = \frac{1}{4}\left(B^2 - 2B + 4\right). \tag{C.3}$$

The maximum power of a symbol in QAM can therefore be calculated as:

$$P_{max} = 2 \times A_{max}^2 = \frac{1}{8}\left(B^2 - 2B + 4\right)^2. \tag{C.4}$$

The average power P_{av} of the constellation is also a function of the number of bits per symbol:

$$P_{av} = \sum_{n=1}^{M} A_n \times A_n^* = \frac{1}{24}\left(B^4 - 4B^3 + 20B^2 - 32B + 48\right). \tag{C.5}$$

The normalised mean power P_{norm} of a constellation is therefore given as:

$$P_{norm} = \frac{P_{av}}{P_{max}} = \frac{1}{3} \times \left(1 + \frac{8}{B^2 - 2B + 4}\right). \tag{C.6}$$

© University of Pretoria

APPENDIX D

DERIVATION OF THE CRAMÉR-RAO BOUND

D.1 INTRODUCTION

This section expands the derivation of the CRB for a ULA, UCA and UCA-CE.

D.2 UNIFORM LINEAR ARRAY CRB

The derivative of the steering vector can be simplified for a ULA:

$$|\dot{\mathbf{a}}(\theta)|^2 = k^2 \cos^2(\theta) \sum_{n=1}^{N_a} d_m^2 = k^2 d_0^2 \cos^2(\theta) \frac{N_a(N_a^2-1)}{12}. \tag{D.1}$$

The expression is a function of the number of snapshots, the SNR, the wave-number k, the antenna spacing d_0 and the number of antennas. The CRB for a ULA can therefore be determined:

$$\text{CRB}_{ULA} \approx \frac{6}{K \times \text{SNR} \times k^2 d_0^2 \cos^2(\theta) N_a(N_a^2-1)}. \tag{D.2}$$

Finally, if it is assumed that half wave-length spacing is used, the CRB can further be simplified to:

$$\text{CRB}_{ULA} \approx \frac{6}{K \times \text{SNR} \times \pi^2 \cos^2(\theta) N_a(N_a^2-1)}. \tag{D.3}$$

© University of Pretoria

D.3 UNIFORM CIRCULAR ARRAY CRB

The derivative of the steering vector can be simplified for a UCA:

$$|\dot{\mathbf{a}}(\theta)|^2 = k^2r^2\sum_{n=1}^{N_a}\cos^2\left(\frac{2\pi n}{N_a}-\theta\right) = \frac{k^2r^2N_a}{2}. \tag{D.4}$$

It can be derived that for a UCA the CRB is a function of the number of snapshots, the SNR, the wave-number, the radius of the circle r and the number of antennas:

$$\mathrm{CRB}_{UCA} \approx \frac{1}{K\times\mathrm{SNR}\times k^2r^2\times N_a}. \tag{D.5}$$

If it is assumed that the radius of the circle is half a wave-length, the CRB can further be simplified to:

$$\mathrm{CRB}_{UCA} \approx \frac{1}{K\times\mathrm{SNR}\times \pi^2\times N_a}. \tag{D.6}$$

D.4 UNIFORM CIRCULAR ARRAY WITH A CENTRE ELEMENT CRB

The derivative of the steering vector can be simplified for a UCA-CE:

$$|\dot{\mathbf{a}}(\theta)|^2 = 0 + k^2r^2\sum_{n=1}^{N_a-1}\cos^2\left(\frac{2\pi n}{N_a-1}-\theta\right) = \frac{k^2r^2(N_a-1)}{2}. \tag{D.7}$$

It can be derived that for a UCA-CE the CRB is a function of the number of snapshots, the SNR, the wave-number, the radius of the circle and the number of antennas (D.8):

$$\mathrm{CRB}_{UCA-CE} \approx \frac{1}{K\times\mathrm{SNR}\times k^2r^2\times (N_a-1)}. \tag{D.8}$$

If it is assumed that the radius of the circle is half a wave-length, the CRB can further be simplified to (3.20):

$$\mathrm{CRB}_{UCA-CE} \approx \frac{1}{K\times\mathrm{SNR}\times \pi^2\times (N_a-1)}. \tag{D.9}$$

© University of Pretoria